DYNAMIC TERRAMECHANIC MODEL FOR LIGHTWEIGHT WHEELED MOBILE ROBOTS

by

Rishad Irani

Submitted in partial fulfillment of the requirements
for the degree of Doctor of Philosophy

at

Dalhousie University
Halifax, Nova Scotia
August 2011

DALHOUSIE UNIVERSITY

DEPARTMENT OF MECHANICAL ENGINEERING

The undersigned hereby certify that they have read and recommend to the Faculty of Graduate Studies for acceptance a thesis entitled "DYNAMIC TERRAMECHANIC MODEL FOR LIGHTWEIGHT WHEELED MOBILE ROBOTS" by Rishad Irani in partial fulfilment of the requirements for the degree of Doctor of Philosophy.

Dated: August 8, 2011

External Examiner: _____

Research Supervisor: _____

Examining Committee: _____

_____

_____

Departmental Representative: _____

DALHOUSIE UNIVERSITY

DATE: August 8th, 2011

AUTHOR: Rishad Irani

TITLE: DYNAMIC TERRAMECHANIC MODEL FOR LIGHTWEIGHT WHEELED MOBILE ROBOTS

DEPARTMENT OR SCHOOL: Department of Mechanical Engineering

DEGREE: PhD CONVOCATION: October YEAR: 2011

Signature of Author

To my family...all of them

TABLE OF CONTENTS

List of Tables

List of Figures

ABSTRACT

This doctoral thesis extends analytical terramechanic modelling for small lightweight mobile robots operating on sandy soil. Previous terramechanic models were designed to capture and predict the mean values of the forces and sinkage that a wheel may experience. However, these models do not capture the fluctuations in the forces and sinkage that were observed in experimental data.

The model developed through the course of this research enhances existing terramechanic models by proposing and validating a new pressure-sinkage relationship. The resulting two-dimensional model was validated with a unique high fidelity single-wheel testbed (SWTB) which was installed on a Blohm Planomat 408 computer-numerically controlled creepfeed grinding machine. The new SWTB translates the terrain in the horizontal direction while the drivetrain and wheel support systems are constrained in the horizontal direction but allowed to freely move in the vertical direction. The design of the SWTB allowed for a counterbalance to be installed and, as a result, low normal loads could be examined. The design also took advantage of the grinding machine's high load capacity and precise velocity control.

Experiments were carried out with the new SWTB and predictable repeating ridges were found in the track of a smooth rigid wheel operating in sandy soil. To ensure that these ridges were not an artifact of the new SWTB a mobile robot was used to validate the SWTB findings, which it did. The new SWTB is a viable method for investigating fundamental terramechanic issues.

A series of experiments at different slip ratios and normal loads were carried out on the SWTB to validate the new pressure-sinkage relationship which explicitly captures and predicts the oscillations about the mean values for the forces and sinkage values for both a smooth wheel and a wheel with grousers. The new pressure-sinkage relationship adds two new dimensionless empirical factors to the well known pressure-sinkage relationship for a rigid wheel. The first new factor accounts for changes in the local density of the terrain around the wheel and the second factor accounts for the effects grousers have on the forces and sinkage.

List of Abbreviations and Symbols Used

Roman symbol	Description	Units
$A_{\odot}$	Area	m^2
A	Amplitude of oscillations	Pa
A_{γ}	Amplitude factor related to density changes	Pa
A_{σ}	Amplitude factor related to Passive Stresses	Pa
a_1	Empirical pressure value for Bevameter test	Pa
a_2	Empirical pressure value for Bevameter test	Pa
b	Wheel width or plate size	m
b_0	Empirical coefficient for maximum normal stress	$--$
b_1	Empirical coefficient for maximum normal stress	$--$
c	Cohesion	Pa
D_h	Hydraulic diameter	m
DP	Drawbar pull	N
e	Void ratio	$--$
F	Force	N
G	Filter transfer functions	$--$
g	Gravity	m/s^2
H	Thrust	N
h_b	Grouser length	m
i	Slip ratio	$--$
j	Soil deformation	m
k	Empirical coefficient	$--$
K	Shear deformation modulus	m
$\hat{k}$	Fitting constant	$--$
k_{ϕ}	Friction modulus	N/m^{n+2}
k'_{ϕ}	Dimensionless friction modulus	$--$
k'_a	Pressure-sinkage modulus	$--$

Roman symbol	Description	Units
k_c	Cohesion modulus	N/m^{n+1}
k'_c	Dimensionless cohesion modulus	$--$
k'_g	Pressure-sinkage modulus	$--$
k_p	Organic stiffness of peat	N/m^3
l	Length	m
l_c	Contact length	m
l_{qp}	Surcharge length	m
m	Mass	kg
$\hat{m}$	Fitting constant	$--$
M_m	Strength of surface mat	N/m^3
n	Sinkage exponent	$--$
$\hat{n}$	Fitting constant	$--$
N_ϕ	Flow value	$--$
n_g	Number of grousers	$--$
p	Pressure	Pa
q	Surcharge	Pa
r	Radius	m
R	Resistance	N
RMS	Root-Mean-Square	$--$
T	Torque	Nm
t	Time	s
V	Velocity	m/s
V_s	Volume of substance	m^3
V_v	Total volume	m^3
w	Width	m
W	Weight	N
z	Sinkage	m

Greek symbol	Description	Units
α_s	Empirical relationship to the sinkage exponent	deg
γ	Weight density	N/m^3
η	Rear of wheel sinkage relationship	$--$
θ	Angle	rad
σ	Normal stress	Pa
$\bar{\sigma_p}$	Mean of the maximum passive stresses	Pa
τ	Shear stress	Pa
Φ	Phase shift	rad
ϕ	Internal angle of friction	deg
ω	Angular frequency or velocity	rad/s

Acknowledgements

The author would like to thank his supervisor Dr. Robert Bauer for his support, expertise and guidance through the various iterations of this doctorial project. The author is also thankful for the support of Drs. Ted Hubbard, Craig Lake and Ya-Jun Pan at Dalhousie University for their support on my supervisory committee. They have always shown a keen interest in this doctorial research.

Financial support for this work originated from Natural Sciences and Engineering Research Council of Canada (NSERC) and the Canadian Foundation for Innovation (CFI). The author would also like to thank Shaw Brick for donating the test sand.

A heart felt "THANK YOU!" goes out to all of my friends and family who have always encouraged me to pursue my dreams.

CHAPTER 1

INTRODUCTION

In 1997 NASA's Mars Pathfinder mission featured *Sojourner*, which was the first planetary rover to traverse Mars. The mission is hailed as a success because it provided scientists with valuable information about the Red Planet; also, the mission lasted for over twelve weeks when the original program was scheduled to last less than four weeks. The next successful rover mission was in 2004 with NASA's Mars Exploration Rovers. These two rovers, named *Spirit* and *Opportunity*, have had their fair share of hardships with the martian terrain. *Spirit* suffered from an inoperative front wheel while *Opportunity* was entrenched in what is now referred to as the "Purgatory Dune". However, the Mars Exploration Rovers have also been wildly successful as they have led to a plethora of scientific discoveries. They have even won the prestigious *Science* magazine's "Breakthrough Of The Year" in 2004 because *Opportunity* discovered salty, rippled sediments of an ancient shallow sea, and *Spirit* discovered a rock that once was so drenched it had actually rotted [Ker04]. With the overall success of these missions many national and international agencies have begun their own rover programs to explore both Moon and Mars, such as the collaborative ExoMars program led by the European Space Agency (ESA). Also, Google has partnered with the X PRIZE foundation for the "Google Lunar X Prize" which is a competition for privately funded teams to land a robot on Moon and have it travel 500 metres over the surface and send images and data back to Earth. To improve the design, simulation, and optimization of the planetary rovers used in these missions, high-fidelity wheel-soil interaction models are needed. Wheel-soil interaction models allow for design engineers and mission specialist to evaluate and improve the design of these

lightweight mobile robots and more accurately predict their mobility capabilities on the terrain. Moreover, a combination of multi-body dynamic simulators with advanced wheel-soil models can also be used to assist the mission specialist in developing strategies to free entrenched vehicles.

Wheel-soil models are typically based on the work of M.G. Bekker who developed classical terramechanics in the mid twentieth century [Bek69]. Terramechanics is the study of vehicle-terrain interaction and Bekker's work focussed on large wheeled and tracked vehicles such as tanks, trucks and armoured personal carriers [Bek69]. His semi-emperical analytical models are still widely used to predict the ground pressure, sinkage and traction for these large vehicles. In recent years Bekker's theories and models have been applied to small lightweight mobile robots, specifically planetary rovers [ID04]. However, Azimi et al. [AHG+10] concluded that there is still a need for further validation and improvement of these traditional terramechanic models. One of the features of Bekker's classical terramechanics is that it focuses on the mean values of the ground pressure, sinkage and traction for a vehicle rather than the dynamic or transient effects about these means. For large-scale vehicles these transient dynamic effects could be negligible; however, for small lightweight vehicles these effects can play a significant role in their overall mobility.

To develop and validate advancements in terramechanic models, a single-wheel testbed was constructed at Dalhousie University. Initial testing with a smooth wheel in sandy soil revealed an oscillatory pattern in the track of the wheel and in the measured drawbar pull — dynamic effects not captured by classical terramechanic models. Figure 1.1 shows the track of a 200mm diameter smooth rigid wheel operating at a slip ratio of 0.25 with a 48N normal load. Slip ratio is the difference between the tangential velocity of the wheel and the forward motion of the wheel, normalized with respect to the tangential velocity. Figure 1.2 compares the corresponding experimental data for this case with simulation results from a terramechanic model [IMNY07] for drawbar pull when plotted as a function of time. In Figure 1.2 one will notice that the terramechanic model has some difficulty predicting the mean sinkage. Such discrepancies are well-known in the field and some researchers have added correction factors to better align

analytical solution with the experimental results. For example, AS^2TM [AES03], a commercially available terramechanic model, has several correction factors to better predict the means, and Meirion-Griffith and Spenko [MGS11] have modified Bekker's original theories to better predict the sinkage for the small wheels used for planetary rovers. Since the mean values can be corrected through empirical and semi-empirical factors, the measured data can be represented in mean-adjusted form as shown in Figure 1.3, so that the oscillatory pattern about the mean values can be highlighted and examined more closely. Figure 1.3 clearly shows that there are oscillations in the measurements that are not accounted for in the current analytical terramechanic models for a smooth wheel. It appears that the oscillations in the drawbar pull and the normal force have the same phase and same low frequency period, suggesting that the oscillations are not random noise but rather caused by the same phenomena and is likely linked to the repeatable ridges found in the track of the smooth wheel. Moreover, the phenomena is not isolated to a single normal load or slip ratio and was observed by this researcher for other slip ratio and normal load conditions. Since the ridges in the sand and resulting oscillations in the measured wheel forces are not accounted for in current terramechanic models and the phenomena is not isolated to a single operating condition, further investigation into this phenomena is needed.

Figure 1.1: Track of a smooth wheel operating in loose sandy soil at a slip ratio of 0.25 with a 48N normal load

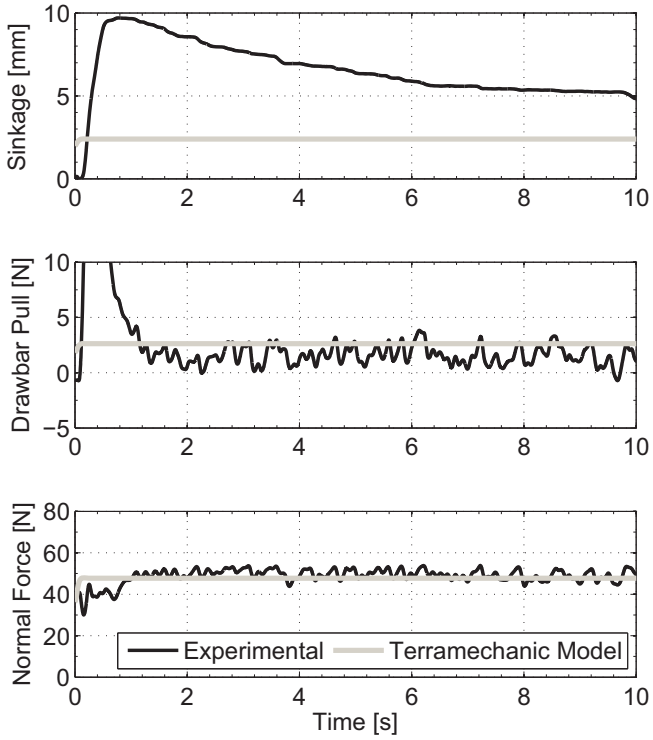

Figure 1.2: Sinkage, drawbar pull, and normal force data from the single-wheel testbed and a terramechanic model [IMNY07] for a smooth wheel with a 48N normal load operating at a slip ratio of 0.25.

Initial testing of a grouser wheel also showed a repeatable oscillation pattern which is caused by the grouser-soil interaction. The track of a 200mm diameter wheel can be seen in Figure 1.4 which clearly shows the repeatable ridges in the terrain after the wheel has passed. The wheel was operating at a slip ratio of 0.25 with a 64N normal load with 16, 10mm long grousers. Figure 1.5 compares the resulting experimental data from a single wheel with simulation results from a terramechanic model [IMNY07] for sinkage, drawbar pull and normal load when plotted as a function of time. It is apparent that the terramechanic model is again unable to model the variations about the mean. The oscillations and ridges in the sand are also not accounted for in the terramechanic model and the present author has observed that this phenomena is not isolated to a single operating condition; therefore, further investigation into the phenomena is required.

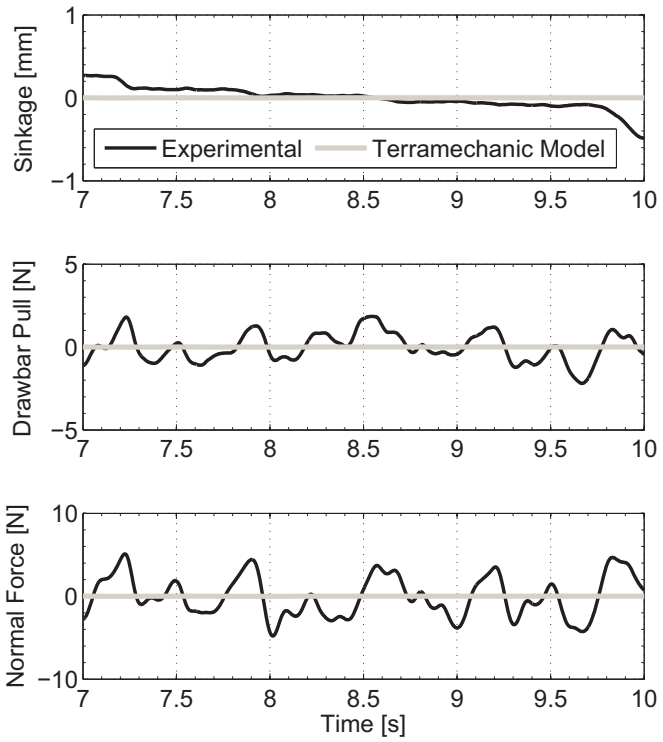

Figure 1.3: Mean-adjusted sinkage, drawbar pull, and normal force data from the single-wheel testbed and a terramechanic model [IMNY07] for a smooth wheel with a 48N normal load operating at a slip ratio of 0.25.

Given these observations, the objective of this research is to: *develop a wheel-soil interaction model for rigid wheels operating in sandy soil that can better predict the oscillations observed in the measured data from the single-wheel testbed*. The resulting model could be used to assist future designers and motion planners of lightweight mobile robots, specifically planetary rovers.

This thesis is divided into 7 chapters. Chapter 2 reviews various experimental setups used to develop and validate wheel-soil interaction models. Chapter 3 reviews terramechanic models and how an analytical model is implemented in this research. The chapter also highlights the effect of various parameters found in traditional analytical terramechanic models. Chapter 4 develops a new dynamic terramechanic model for smooth wheels operating in sandy soil. Chapter 5 further develops this new dynamic terramechanic model for a wheel with grousers

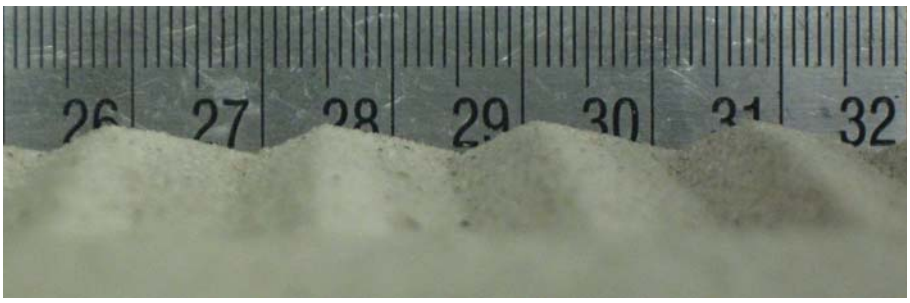

Figure 1.4: Track of a grouser wheel operating in loose sandy soil at a slip ratio of 0.25

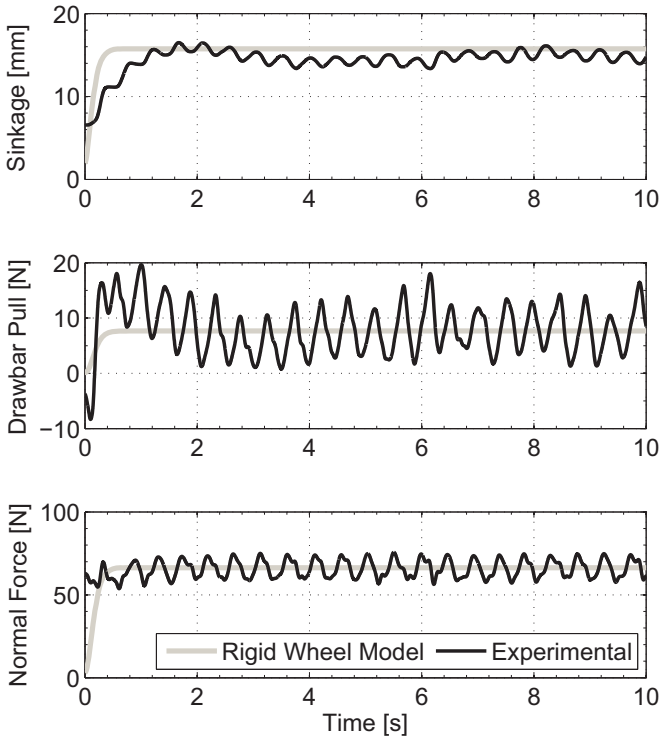

Figure 1.5: Sinkage, drawbar pull, and normal force data from the single-wheel testbed and a terramechanic model [IMNY07] for a wheel with 16 grouser, 10mm long and a 66N normal load at a slip ratio of 0.25.

operating in sandy soil. Chapter 6 examines a selection of experimental cases studies and applications for the new model, while Chapter 7 summarizes the results and contributions.

CHAPTER 2

EXPERIMENTAL EQUIPMENT AND DEVELOPMENT

This chapter reviews various designs of single-wheel testbeds (SWTB) and presents alternative implementations based on the work of others. For the purpose of this doctorial research, a Blohm 408 Plamomat creepfeed machine was converted into a SWTB. The chapter discusses the new SWTB that was designed and built by the author and a selection of preliminary results for various testing configurations. The chapter ends with some quantification of the new SWTB and confirmation that observed ridges in the track of a smooth wheel presented in Chapter 1 are not an artifact of the SWTB.

2.1 Review of Single-Wheel Testbeds

Most SWTB designs share the following characteristics: the terrain is prepared, confined and stationary while the wheel is rotated and translated through the terrain [IMNY07, INY09, AWHT03, SID05, IKSD04, ISD02, LHC+10, MRTG06, BLB05, MFM+07, KTMS06, Ree65]. Figure 2.1 shows a schematic of a conventional SWTB. The conveyance system incorporates an accurate control system to ensure the speed of the wheel and associated support structure is maintained. The relatively large translating structure, including wheel, drivetrain, and sensors can make it challenging to simulate the relatively low normal loads which a rover may experience on Mars or Moon. While a moving counterbalance is possible, it may add dynamic effects and require larger actuators in the system.

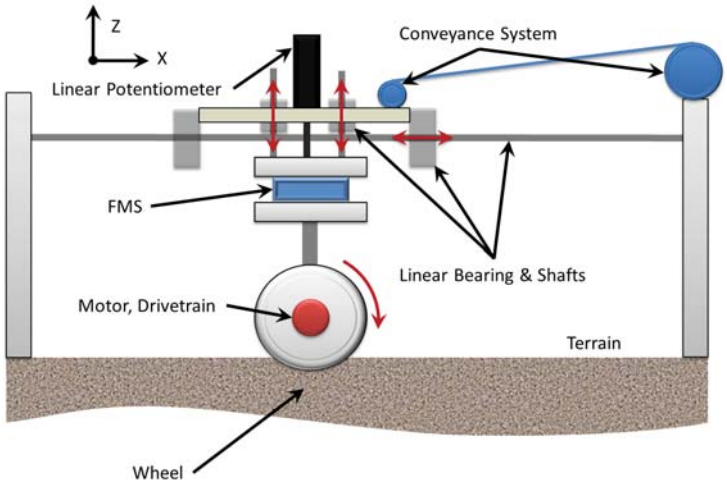

Figure 2.1: Typical SWTB design

A possible design of a SWTB with a counterbalance is shown in Figure 2.2. This four-bar linkage design is based on images of DLR's SWTB [MRTG06]. In this testbed, the entire structure translates in the x-direction along the conveyance slides. These slides may be ball screws, linear motors or actuators. The motor and wheel assembly is fastened to the conveyance system by a set of ball joints and links. On one of these joints a rotary encoder can be installed to determine the sinkage that the wheel experiences. A counterbalance can be added at the end of the link to adjust the normal load experienced by the wheel. If the rigid link is not installed and joints $A_{1,2}$ and $B_{1,2}$ are purely rotational then the sinkage of the wheel and the path of the counterbalance mass follow an arc in the zy-plane, rather than moving only in the z-direction as desired. For small wheel sinkage, this arc-effect is minimal and can be neglected; however, if the sinkage is significant then this arc may need to be accounted for during the analysis. The arcing sinkage can be circumvented if a revolute and prismatic joint is installed at points $A_{1,2}$ and $B_{1,2}$ and a rigid link connects the back of the FMS housing to the conveyance mount. This rigid link would need to have a fixed joint on the back side of the FMS but have a prismatic joint on the conveyance mount at point C_1 which allows the mechanism to translate freely in the z-direction. The addition of the revolute and prismatic joint with a rigid link would confine the

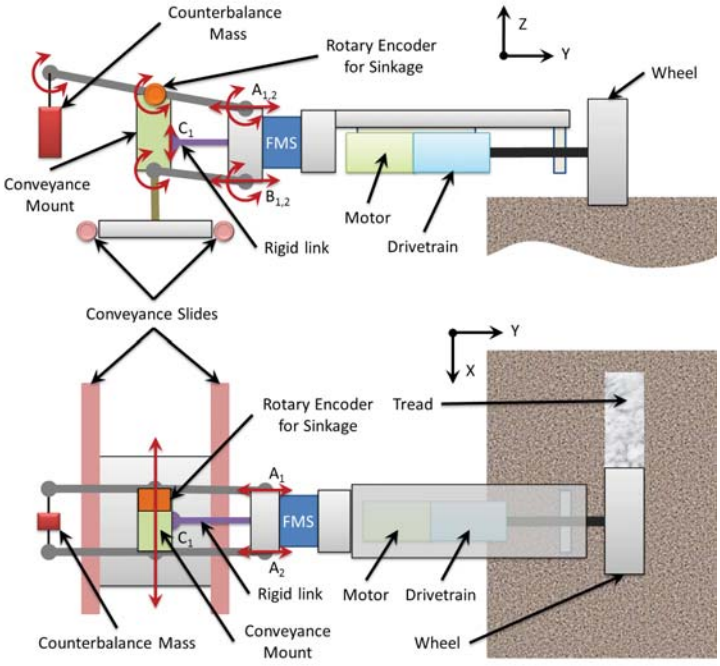

Figure 2.2: Counterbalanced SWTB

sinkage to only occur in the zx-plane. A similar arrangement could be done for the counter balance so that its motion is also confined to the zx-plane. With the complex joints at points $A_{1,2}$ and $B_{1,2}$ one does have to be careful of added friction forces that could be imparted on the FMS and cause one to misinterpret the force readings.

Another SWTB implementation is a rotary system, shown schematically in Figure 2.3. This type of rotary SWTB was used by Mungas et al.[MFM+07] and Shamah et al. [SARW98]. Instead of using conveyance slides as shown in Figure 2.2, Mungas et al. and Shamah et al. employed a rotary actuator with the terrain contained in an annulus around the rotary actuator. In this design the wheel is always skidding slightly and thus it is always experiencing small lateral forces. If one were to use this SWTB for fundamental terramechanic research, interpreting forces and torques from this setup may pose a challenge. The contact of the wheel and soil is not a solitary point but rather a patch ahead and behind the drive axle. In this configuration, as the wheel rotates, the leading half of the contact patch

(ahead of the centreline) has its tangential velocity $v_{t\ lead}$ angled towards the centre of the SWTB. However, the trailing half of the contact patch (behind the centreline) has its tangential velocity $v_{t\ trail}$ angled away from the centre of the SWTB. Figure 3 shows these angles greatly exaggerated for graphical purposes. The net effect of these two tangential velocities would cancel and result in a tangential velocity that is perpendicular to that of the centreline. However, the displacement vector of the sand particles under the wheel is far more complicated since they would experience a change in direction from the leading to trailing halves of the wheel. As a result the shear component of a terramechanic model can be difficult to interpret since the shear stress would have a tangential and radial component with respect to the xy-plane of the terrain as shown in Figure 2.3. Furthermore, rotation of any counterbalances would impart dynamic effects across the system that would need to be accounted for. As the system rotates the counterbalance would try to force the system so that the centre of gravity on either side of the rotary actuator is at the same z-coordinate. As a result the sinkage readings could be affected. At very low speeds the dynamic effects mentioned may be minimal and may not be above the resolution of the sensors. These rotary SWTBs are well suited for concept designs, along with component and endurance testing.

Flippo et al. [FHM10, FM11] developed a SWTB shown in Figure 2.4 called the Suspension and Wheel Evaluation and Experimentation Testbed (SWEET). This design employs a wheel which is allowed to spin about its drive axle and translate in the z-direction. A table positioned below the wheel is controlled by three omni-directional motors that are 120° apart. This actuation setup allows for the terrain (being supported by the moving table) to translate and rotate in the xy-plane. The authors mentioned that there is a counter balance system in the z-direction; however, no details are given on how it is implemented.

The researchers involved with SWEET intend to use it for traction, sinkage, turning efficiency, compliancy and rolling efficiency studies for various wheel designs in sand. In order to perform testing with sand, the omni-directional motors must be extremely powerful since the density of sand is between 1200 and 1700 kg/m^3 and the mass of a $1.8 \times 0.5 \times 0.15$m terrain box can reach well over 300kg with a support structure. Flippo et al. [FHM10] mention that SWEET has the

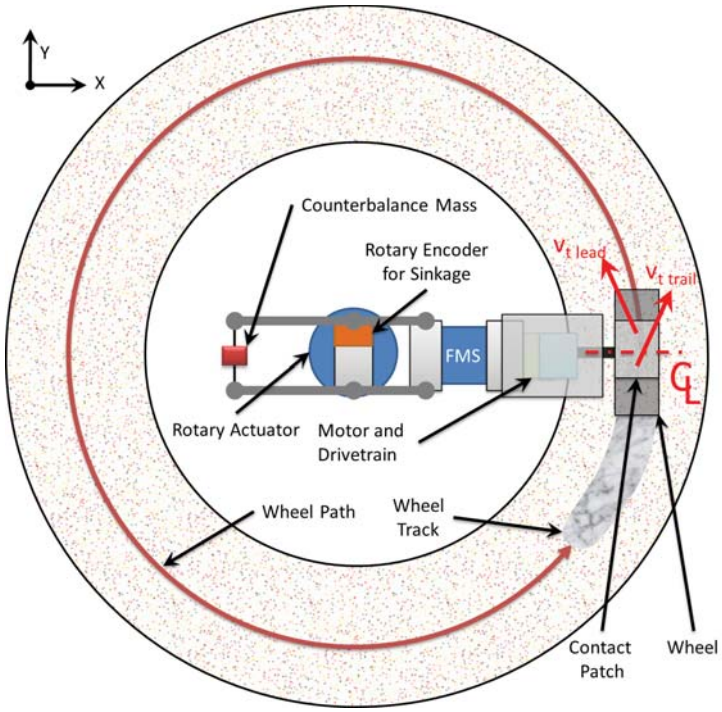

Figure 2.3: Rotary SWTB

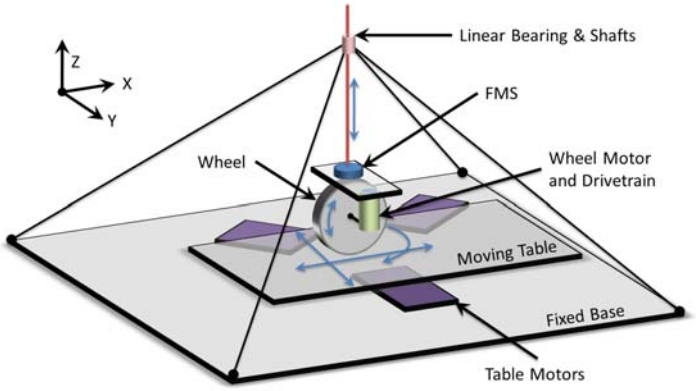

Figure 2.4: SWTB — Suspension and Wheel Evaluation and Experimentation Testbed SWEET

ability to measure forces and torques in a true turn. The researchers also intend to study sloped terrain using this SWTB.

One could conceive of combining the SWEET design with designs based on Figure 2.2 [MRTG06]. This concept can be seen in Figure 2.5. The conveyance system in this case is allowed to move in the x and y-directions and rotate about the z-axis while the terrain remains fixed. This system would have the potential to examine extremely complex mobility issues under controlled conditions. To successfully understand the measurements obtained from such a system would require copious amounts of studies to understand the complex dynamic effects that are imparted on the system which were previously mentioned.

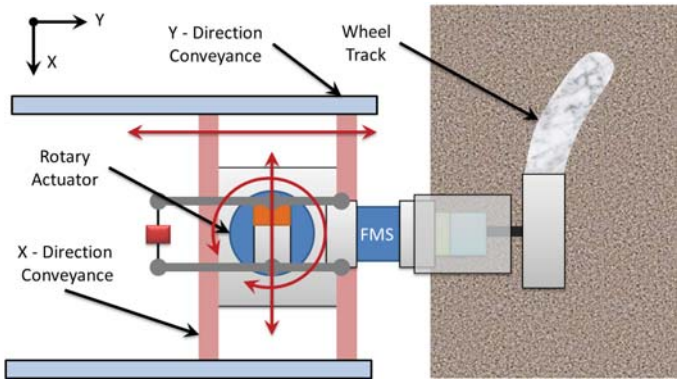

Figure 2.5: Possible design of a SWTB

2.2 New Single-Wheel Testbed

The author has access to a Blohm 408 Planomat creepfeed grinding machine which is extremely rigid and capable of supporting and translating as much as 800kg at rates ranging between 30 and 40,000mm/min. The maximum stroke of the machine is 950mm and the machine's Fanuc controller is easily capable of duplicating experimental velocities and configurations. It was decided that the grinding machine would be retrofitted to accommodate a SWTB such that the machine's table supports and translates the sand while keeping the wheel support stationary similar to the design use by Flippo et al. [FHM10, FM11].

The transformation was accomplished by removing the grinding wheel and associated housing so that the SWTB platform could be installed as shown in Figure 2.6 and 2.7. The wheel is allowed to move freely up and down in the z-direction along eight lubricated linear bearings. A linear potentiometer is used to record the sinkage in the z-direction. To control the wheel rotational speed, a closed-loop tachometer feedback control system was implemented. A JR3 6-degrees-of-freedom transducer measured the wheel-soil interaction forces and associated moments, while a FUTEK torque sensor recorded the wheel motor torque directly on the geartrains output shaft. A National Instruments PCI-MIO-16XE-10 board was used in conjunction with LabView to record all of the sensor data.

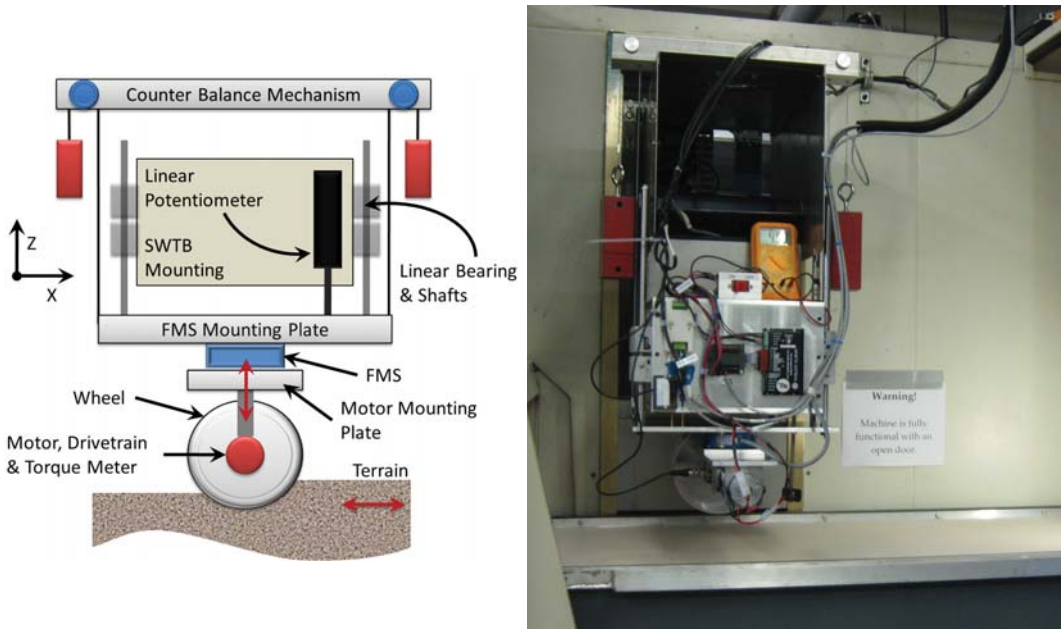

Figure 2.6: The new SWTB with a counterbalance

To alter the slip ratio in the SWTB, the translational speed of the terrain was varied, rather than the wheel rotational speed in order to take advantage of the high-performance characteristics of the grinding machine's control system. While the wheel drive system is extremely reliable, the Fanuc controller offers more flexibility in the testing range without risk of overloading any sensors or drive components. The test wheels were driven by a Dynetic Brushed motor that has a rated torque of 0.155Nm. The motor is directly connected to a 231.59:1 gearhead that

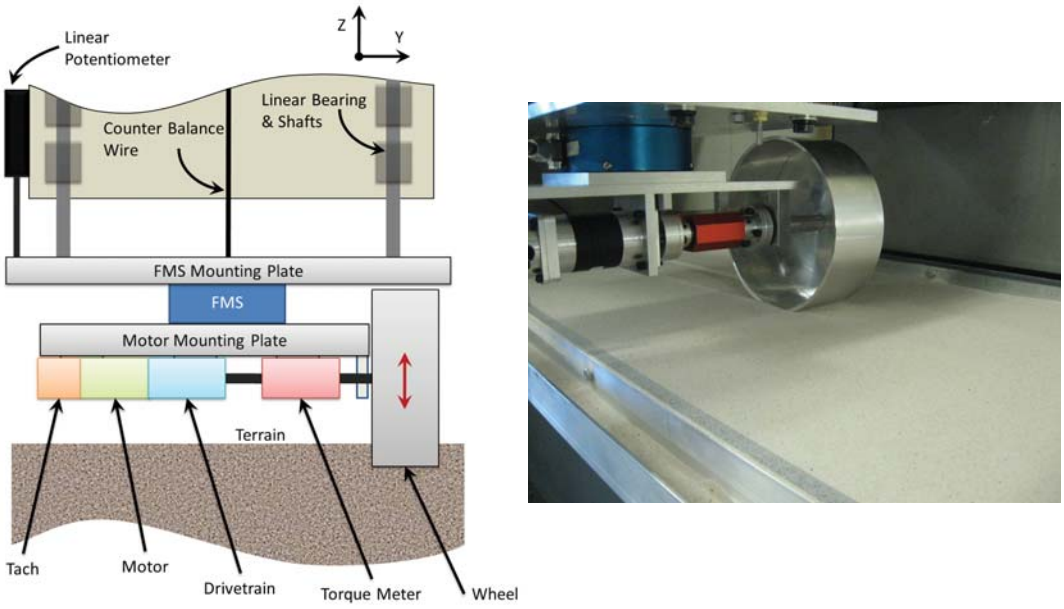

Figure 2.7: Experimental setup of the new SWTB

has a rated torque of 25Nm and a peak torque of 37Nm. The FUTEK torque sensor is rated up to 20Nm. A Dynetic 750 series PWM servo amplifier with tachometer feedback from the back shaft of the motor was used to keep the tangential wheel speed of 0.1m/s (motor speed of ∼3400rpm). This system worked extremely well as there less than a 0.5% deviation from the specified velocity, even when a disturbance caused by the wheel's grousers was added. To avoid damaging any of the drivetrain or sensors the torque output was continuously measured and displayed during the test so that an emergency stop could be tripped if the torque grew beyond the specified safety limit. Figure 2.8 show a schematic of the control and actuation systems of the SWTB.

To study small normal loads, such as those experienced on Mars or Moon, a simple counterbalance was added to the SWTB as seen in Figure 2.6 and 2.7. The velocity and acceleration of wheel sinkage is often taken as quasi-static in planetary rover applications [KTMS06]. It was observed that the wheel sinkage and corresponding counterbalance motion was slow enough to reasonably assume that any dynamics associated with the motion of the counterbalance would not

greatly affect the terramechanic outcomes of the experiments. Moreover, the dynamics of the counterbalance can also be modelled by taking advantage of multibody dynamic tools such as SimMechanics in MATLAB & Simulink.

Previous SWTBs [IMNY07, INY09, SID05, IKSD04, BLB05] used sand depths of 12 to 15cm. For this doctorial research, the grinding machine's high load capacity was taken advantage of and, therefore, a significantly deeper terrain was used. A sandbox 172.5cm long by 52.5cm wide by 29cm deep was installed on the grinding machine's table. The 29cm of sand negated any wall effects, especially at high normal loads, so that the terrain could be considered to be infinitely deep and uniform. To neglect wall effects the normal stress at the bottom of the sand box should be negligible and to calculate the stress through the depth of the sand one can use the following equation [Won01]:

$$\sigma = p_o \left(1 - \frac{1}{\left(1 + \left(\frac{r}{z}\right)^2\right)^2} \right) \tag{2.1}$$

Where p_o is the surface pressure (F/A) from the contact, r is the radius of the contact patch and z is the depth below the surface. Using a 7cm diameter contact patch with an applied force of 19.62N (2kg), the normal stress at the bottom of the new SWTB is 0.15kPa while other SWTBs can have up to 0.77kPa at the bottom of their terrain—a percent difference of 136%.

Another advantage of using the Blohm 408 Planomat is that its conveyance components are already sealed from the abrasive sand by virtue of the machine's intended application. Thus, one did not have to worry about spilling sand inside

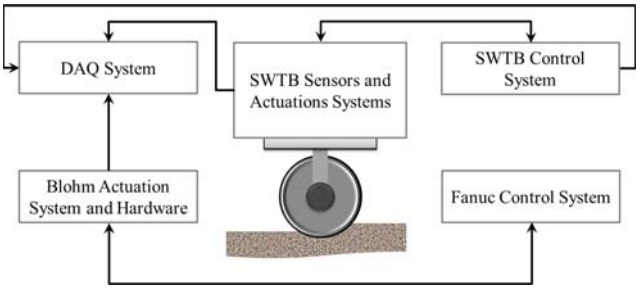

Figure 2.8: Schematic of control and data acquisition systems

of the machine and damaging any components while preparing the terrain for an experiment. Prior to each experiment the terrain was mixed to remove any previous compaction from the prior run and then the terrain was levelled by dragging a metal scraper along the edges of the terrain box. The end result was a uniformly distributed random structure throughout the terrain. There is a trough running along the outer edge of the terrain box to capture any excess spilled sand from the leveling process. A sample image of the prepared terrain can be seen in Figure 2.7. Moreover, the mixing process and terrain preparation would allow for a initial condition of the terrain density to be similar for each test.

2.3 SWTB Capabilities and Results

To compare how the new SWTB design would replicate various loading conditions a few simplified calculations were carried out that approximated the curved wheel as a flat plate. The pressure exerted by a static wheel of a full sized rover (approximately equivalent to NASA's MER rovers) can be found by using:

$$p_{rover} = \frac{F}{A_{\odot}} = \frac{m_{rover} g_{mars} / 6}{w \times l} \tag{2.2}$$

Where, w and l are the width and projected length of the contact patch of the wheel. The pressure exerted by a static wheel on the SWTB can be found by using:

$$p_{SWTB} = \frac{F}{A_{\odot}} = \frac{m_{applied} g_{earth}}{w \times l} \tag{2.3}$$

Here, $m_{applied}$ was varied to replicate various loading conditions and to simulate different planetary conditions. Figure 2.9 illustrates the ground pressure imposed by a full sized rover on Earth, Mars and Moon using Equation (2.2). These pressures can then be compared to the pressures felt by the author's test wheel on the SWTB for various loading conditions by changing $m_{applied}$ in Equation (2.3). As seen in Figure 2.9, the testing range of the SWTB is quite large and it is capable of replicating Moon, Mars and (obviously) Earth scenarios.

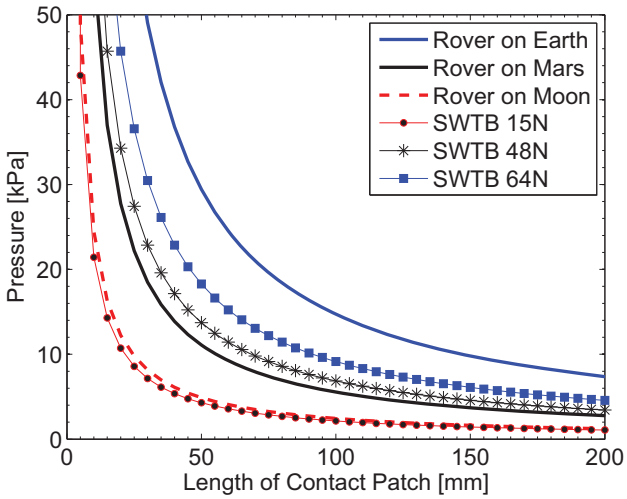

Figure 2.9: Testing range of the SWTB and compared to a full sized rover on Earth, Mars and Moon

2.3.1 *Testing and Procedures*

Various preliminary studies were carried out to develop a standard experimental method and to validate the SWTBs capabilities. Figure 2.10, 2.11 and 2.12 show sample images taken of various rigid wheels mounted on the SWTB traversing through the sandy soil. Figure 2.10 shows a rigid wheel with 32 grousers of height 10mm operating at a slip ratio of 0.90. It can be seen from this viewing angle that there is considerable excavation of terrain occurring around the wheel. This terrain material is being transported behind the wheel by the grousers. The resulting crater that is created has walls approaching the angle of repose of the sand. Figure 2.11 shows the same wheel near the beginning of the 0.90 slip ratio test. From this viewpoint, one can clearly see the massive amount of terrain material being excavated by the grousers. The height of the resulting pile decreases from the extreme level shown in the view as the test proceeds. The initial pileup is an artifact of the testing procedure which starts each experiment with the wheel resting on top of the sand. To start the SWTB, the terrain translation and wheel rotation commence simultaneously. The large pile at the start of the test occurs as the wheel excavates down to its nominal operating condition. These two viewpoints on the

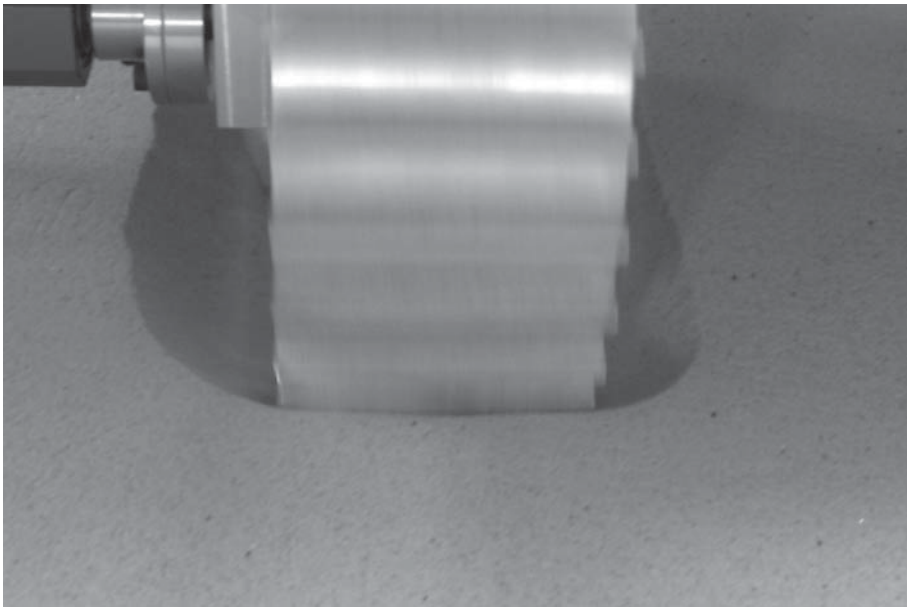

Figure 2.10: Front view of a rigid grouser wheel operating in sandy soil

SWTB can be used to visually quantify the behaviour and transportation of terrain around the wheel that occurs. Figure 2.12 shows a smooth wheel operating at 0.00 slip. This view can be used to visually determine sinkage and quantify any bulldozing effects. It was observed that, for the wheels and the sandy soil used in this research, there was minimal bulldozing and, therefore, bulldozing models of Bekker, [Bek69], Hegedus [HU60] or Wilkinson [WD07] were not considered for the wheel-soil interaction examined in this work.

Figure 2.13 shows the sinkage reading for an entire experiment of a 200mm diameter wheel with 16, 10mm long grousers with a normal load of 48 N operating at a slip ratio of 0.35. In region A of the graph, the wheel is locked in the stored position, not touching the sand. The sand is mixed and levelled while the wheel is in this position. The wheel is then lowered, region B, and allowed to come to rest on the sand surface, region C. The table translation and the wheel's rotation are initiated and the experiment runs in region D. At the end of the run the table's motion is stopped but the wheel rotation continues momentarily resulting in an increase in sinkage at the interface of region D and E. In region E the wheel is returned to the locked, stored position.

Figure 2.11: Rear prospective view of a rigid grouser wheel operating in sandy soil

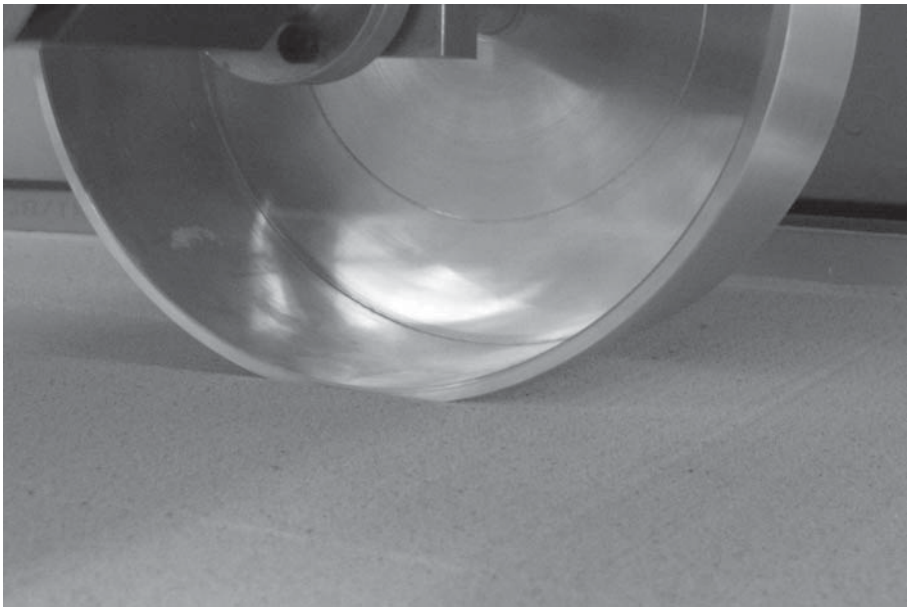

Figure 2.12: Side view of a smooth rigid wheel operating in sandy soil

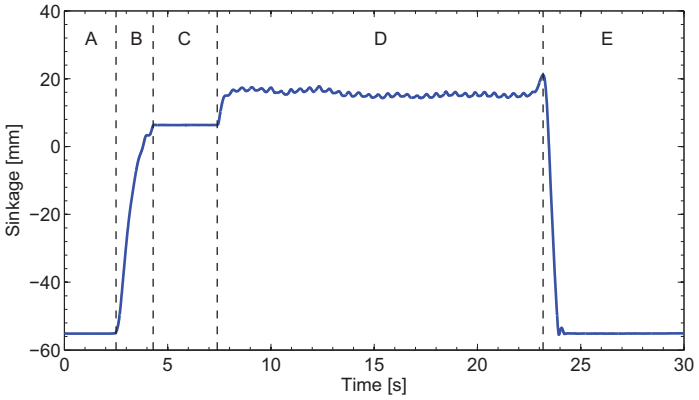

Figure 2.13: Sinkage vs. Time: 200mm diameter wheel with 16 grousers, 9.5mm long with a normal load of 48N operating at a slip ratio of 0.35

Examining region D of Figure 2.13 one can see that the sinkage levels out to an average of 15mm about half way through the experiment and continues at that level for the remainder of the run. It was observed that the SWTBs 950mm travel is sufficient to achieve steady state for a vast majority of test scenarios. Region D also shows how the sinkage oscillates due to the presence of grousers. As the grousers move under the wheel they push the wheel upwards causing the sinkage to vary slightly. The period of these oscillations is a function of the space between the grousers and the slip ratio. This oscillation is a similar result to that of [BLB05, DGD+11] and is not explicitly modeled in the Ishigami et al. [IMNY07] model that is based on traditional Bekker [Bek69] theory.

The presented data from the SWTB was sampled at 1kHz and post-processed with a digital second order lowpass filter. The transfer function of the digital filter in the z-domain is:

$$G(z) = \frac{2.4\,(10)^{-4}\,(z+1)^2}{(z^2 - 1.956z + 0.9565)} \tag{2.4}$$

The filter was created by the `butter` command and implemented with the `filter` in MATLAB. Figure 2.14 demonstrates the filter acting on a hypothetical signal $\sin(4\pi t)$. The figure presents a simple low frequency sine wave and then the same sine wave with uniformly distributed random noise of $\pm$ 0.5 is plotted as a function of time. The time vector t is incremented in .001s steps, which is the same

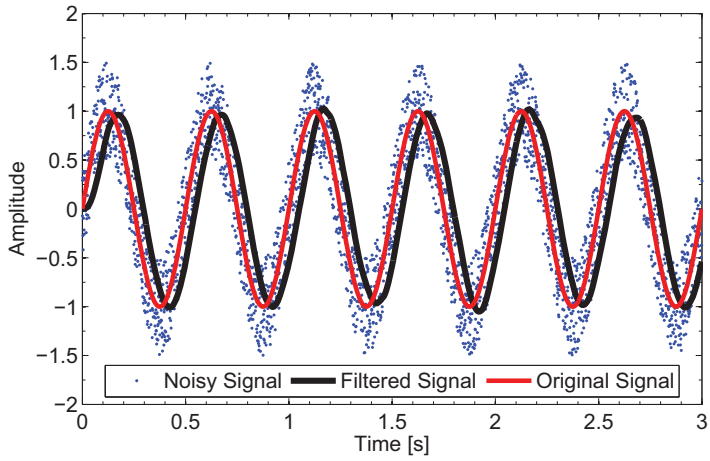

Figure 2.14: Filter analysis

as the SWTB data. The noisy signal (noise + $\sin(4\pi t)$) is passed through the filter (Equation 2.4) and plotted on the same axis. When comparing the filtered to the original signal, it can be seen that there is no appreciable distortion of the signal's magnitude. The root-mean-square (RMS) of the noisy signal is 0.756, the filtered signal has a RMS of 0.700 which is very close to the original signal which has an RMS of 0.707. Since this filter removes the noise and leaves the magnitude of a low frequency oscillation relatively unaffected it can be used to process the data when examining the low frequency oscillations in the phenomena mentioned in Chapter 1. The phase shift that the filter imposes on the data can be adjusted in further post processing when aligning the experimental data with simulation results.

Using Equation 2.4, Figure 2.15 shows typical experimental results for sinkage, horizontal, and vertical forces plotted as a function of time for a smooth rigid wheel and a wheel with grousers. The grouser wheel in the figure has 16, 10mm long grousers and both wheels are operating at a slip ratio of 0.25 with a normal load of 48N. One can visually see that the results from the SWTB are very consistent between runs for both cases. There is some natural variation in the initial conditions (time < 0) but after a few seconds all of the tests converge to a steady state value for all of the measurements regardless of the initial conditions.

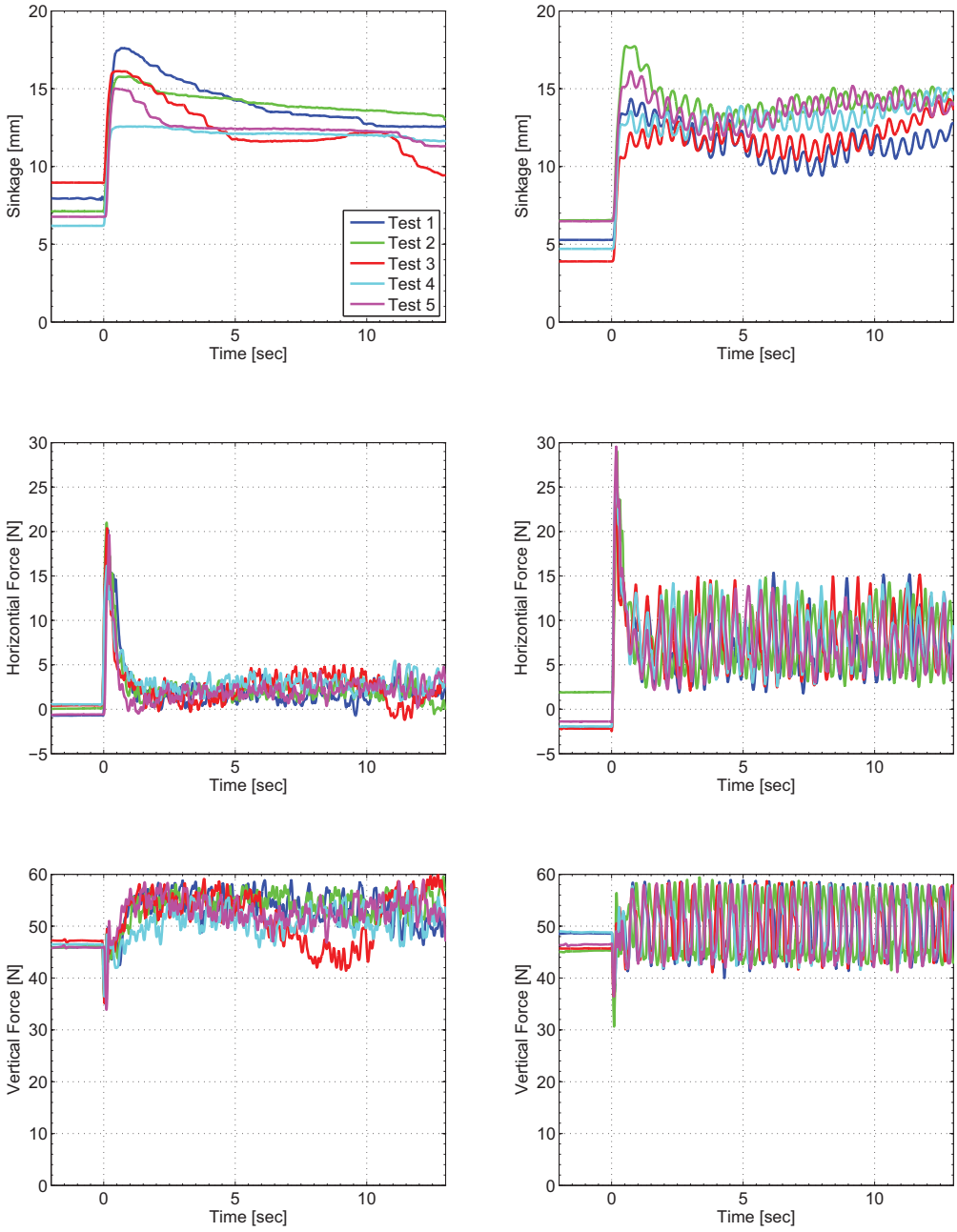

Figure 2.15: Sinkage, horizontal and vertical forces for a Smooth wheel (Left) and a grouser wheel (Right) both cases are for a 48N normal load operating at a slip ratio of 0.25

2.3.2 *Experimental Data*

Figures 2.16 to 2.23 present the average values for the sinkage, horizontal (Drawbar pull) and vertical forces (Normal force) as well as the 95% confidence intervals plotted as a function of time for the various wheel designs and normal load cases examined in this thesis. The relatively small confidence intervals in these figures show that the new SWTB is very consistent for all of the smooth wheel tests and for many of the cases examined with grouser wheels. The means were calculated during steady state operation and averaged over 5 individual test runs. The length of the steady state region varies based on the slip ratio. Since the terrain's linear velocity is altered to control the slip ratio, the amount of time it took for the wheel to traverse the 950mm varied. A 0.00 slip experiment lasts a total of 10 seconds with a steady state region of 2 to 5 seconds, while a 0.95 slip run takes 207 seconds to complete with over 200 seconds of steady state operation and over 200,000 data points or samples (sample rate was 1kHz). One will notice that for a majority of the testing conditions the confidence intervals are very small; however, for a few tests at the high slip ratios, there are large variations in the measured data which is caused by the presence of grousers excavating the loose sandy soil. At these high slip ratios the wheel did not reach a constant sinkage during steady state, instead the wheel sinkage reached a steady state of increasing sinkage. This continual increasing sinkage causes the 95% confidence intervals, which is taken during the steady state region of operation, to be very large. A confidence interval represents the range at which 95% of the data will fall within of a subsequent test, during the period of steady state operation. Therefore, during a period of a steady state increase, the confidence interval will span the range of the increase and, as a result, the confidence interval can represent the degree of the increase during steady state operation. Therefore, the confidence intervals are not necessarily representative of the amplitude of the oscillations which were mentioned in Chapter 1.

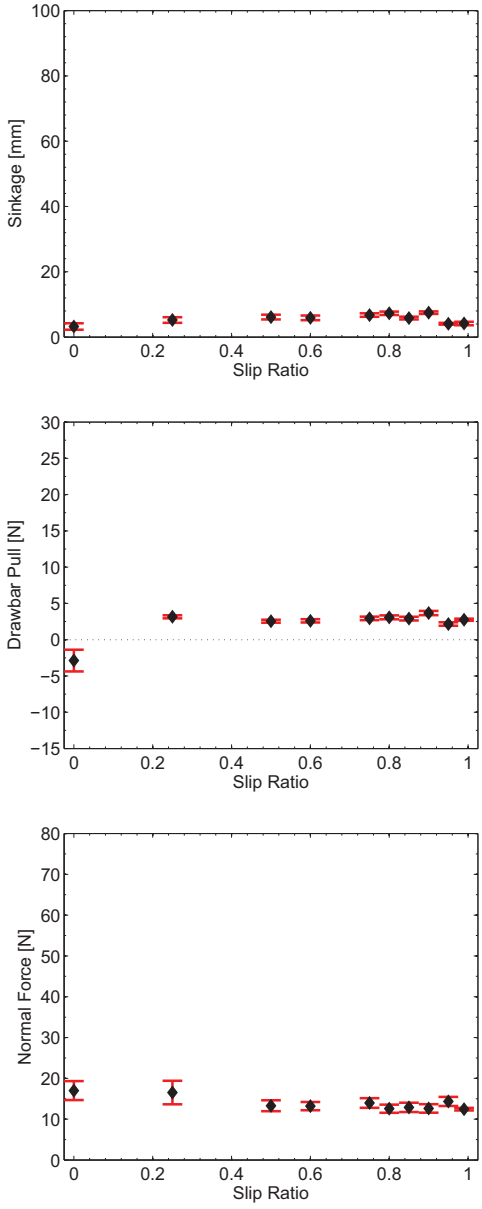

Figure 2.16: Mean data from a smooth wheel with a 15N normal load

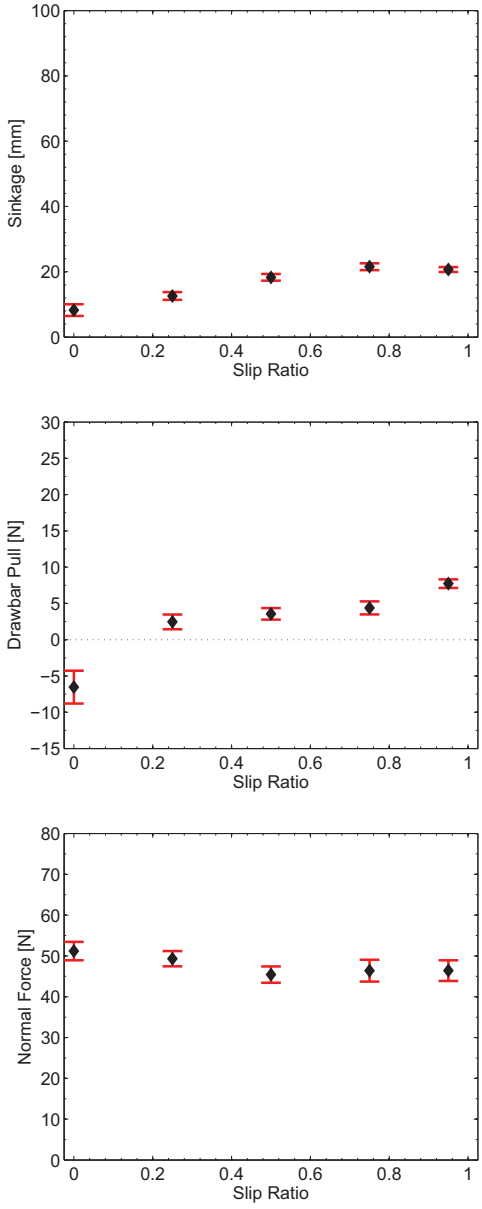

Figure 2.17: Mean data from a smooth wheel with a 48N normal load

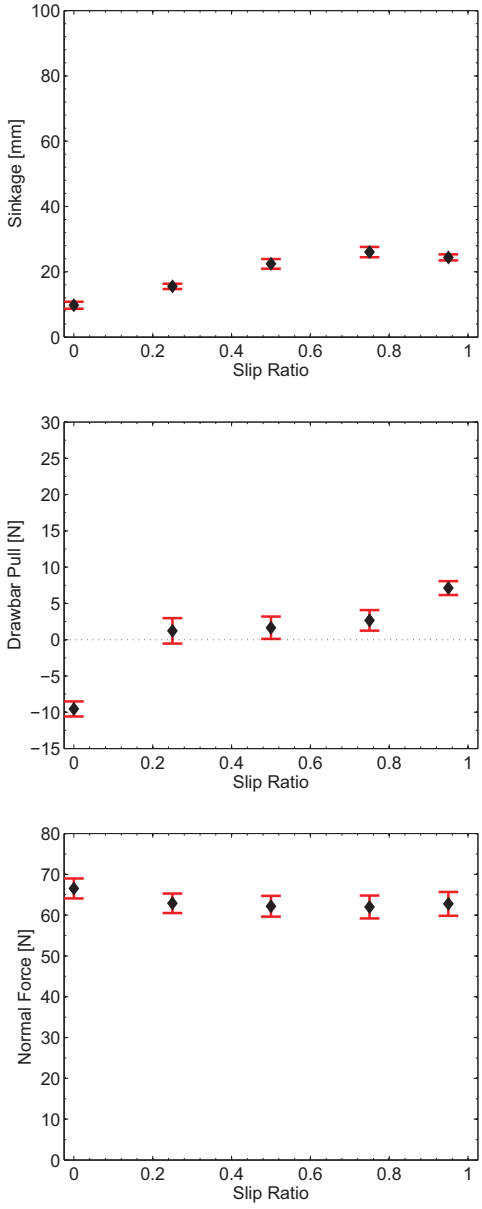

Figure 2.18: Mean data from a smooth wheel with a 64N normal load

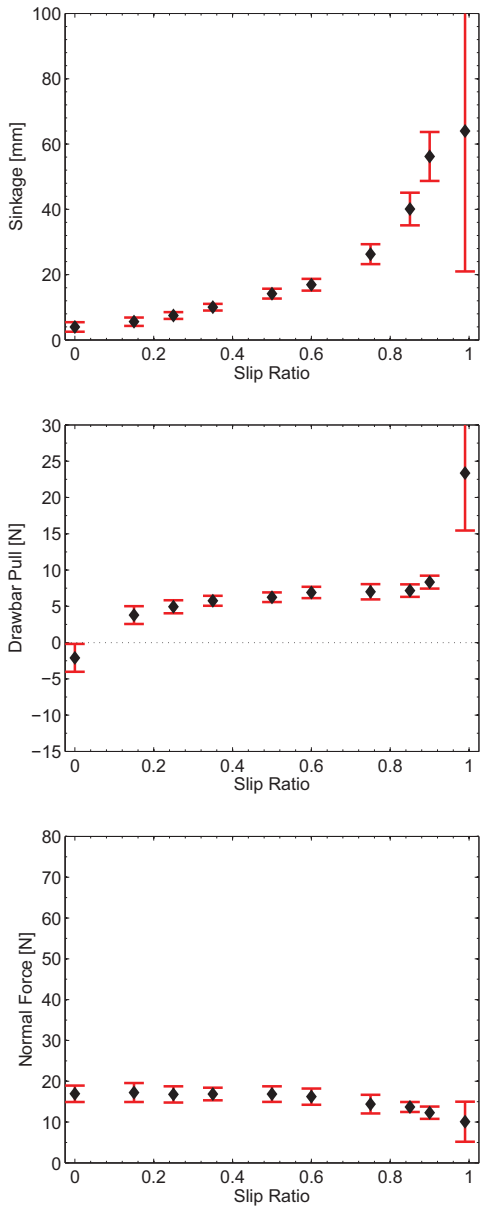

Figure 2.19: Mean data from a smooth wheel with normal load of 15N and 16, 10mm grousers

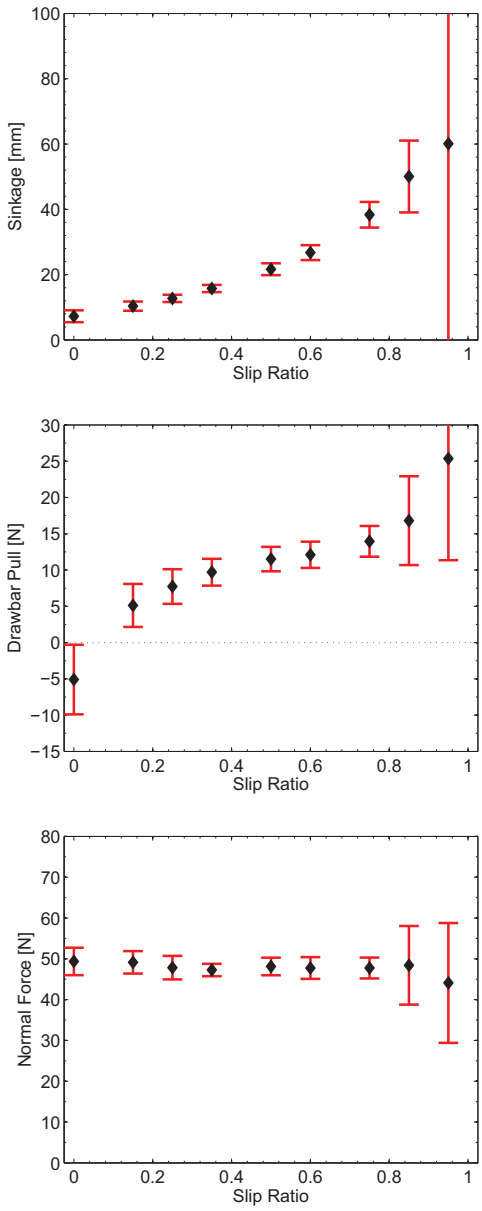

Figure 2.20: Mean data from a smooth wheel with normal load of 48N and 16, 10mm grousers

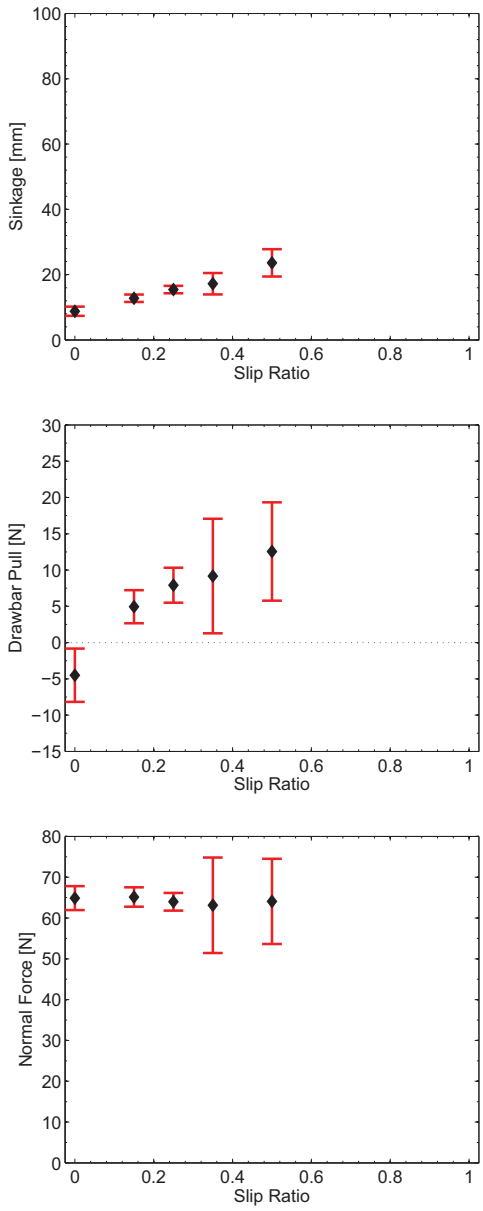

Figure 2.21: Mean data from a smooth wheel with normal load of 64N and 16, 10mm grousers

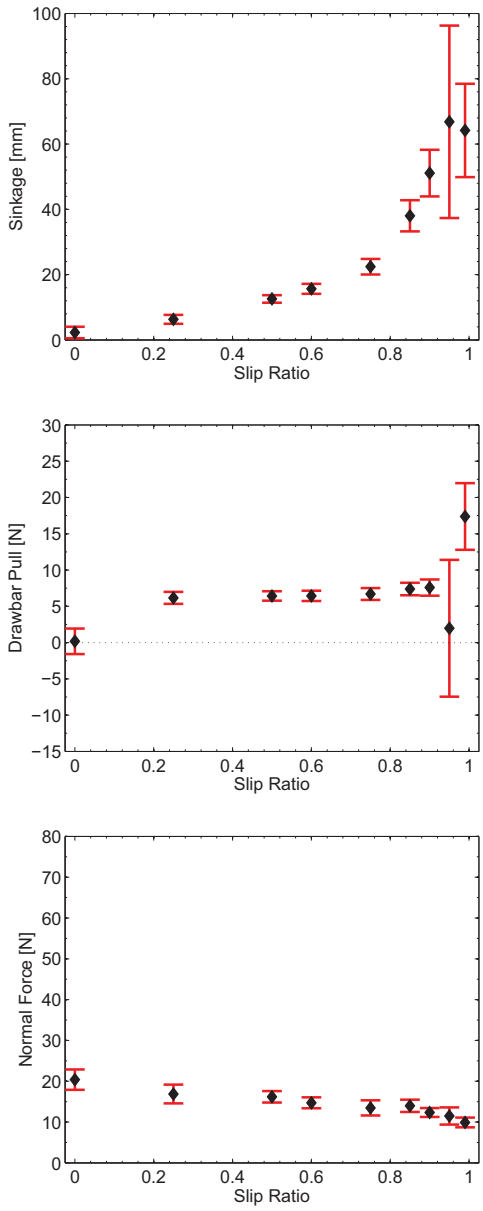

Figure 2.22: Mean data from a smooth wheel with normal load of 15N and 32, 10mm grousers

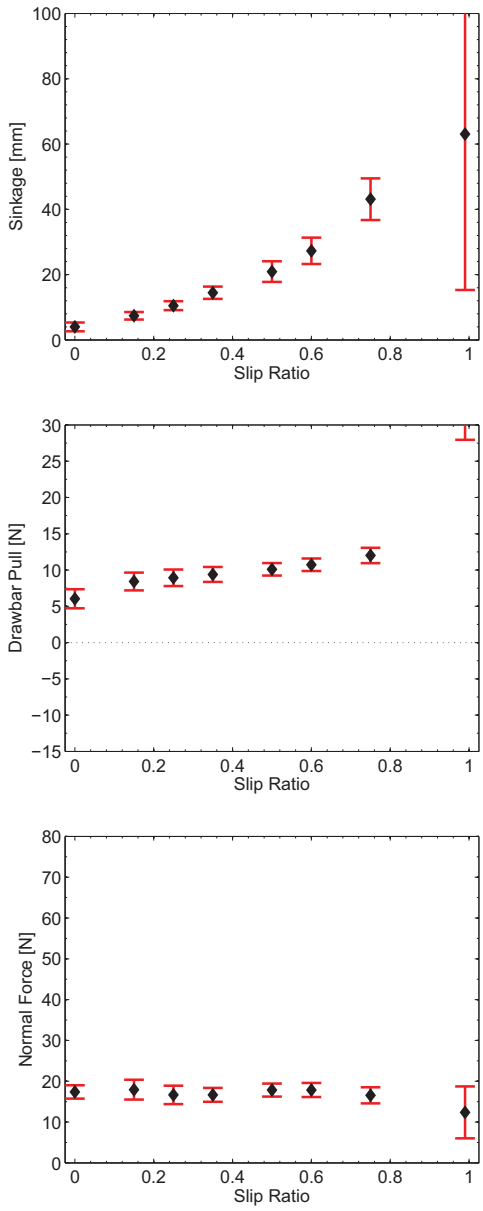

Figure 2.23: Mean data from a smooth wheel with normal load of 15N and 16, 23mm grousers

2.3.3 *Comparison*

A comparison was performed relating the new SWTB to a selection of previously published work to help confirm that the new configuration and equipment is capable of high-fidelity terramechanic studies. Ishigami et al. [IMNY07] used a traditional single-wheel testbed and lunar regolith simulant, equivalent to FJS-1 of Kanamori et al. [KUY+98], and were studying turning maneuvers. The data from the new SWTB in Figures 2.21, is of a 200mm diameter wheel with 16, 10mm grousers operating with a 64N normal load. This operating condition is comparable to Ishigami et al.'s results which used a 180mm diameter wheel operating with a 64.7N normal load and with and unspecified number of 10mm grousers. Figure 2.24 shows experimental drawbar pull (horizontal force) data from the new SWTB and similar tests performed by Ishigami et al.. The data from the new SWTB had a wheel angled at 0° while Ishigami et al's wheel was angled at 5°. Since Ishigami et al. were studying turning maneuvers their data is for a wheel at an angle moving through the terrain. One can see that even though the conditions are not identical the results show reasonable agreement.

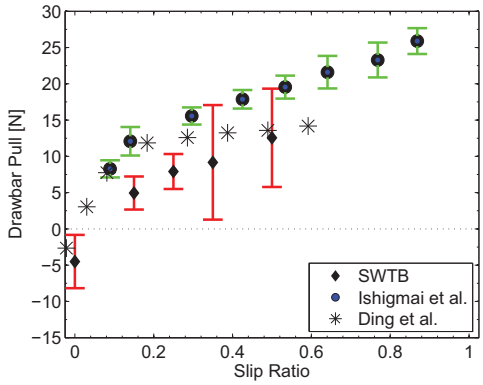

Figure 2.24: Comparison of published drawbar pull data and experimental drawbar pull data from the new SWTB

A comparison to a selection of Ding et al.'s [DGD+11] results to those produced by the new SWTB is also presented in Figure 2.24. The work of Ding et al. concentrated on the determining influence of wheel size, wheel width, grouser height, number of grousers, grouser inclination angles, vertical load, velocity and multipass effects. The data in Figure 2.24, which is from the study [DGD+11], is

of a wheel measuring 314.7mm diameter and 165mm wide with 30, 10mm long grousers. Moreover, Ding et al. reported periodic tracks which grousers produce and the oscillations which grousers cause in the measured data. However, Ding et al. do not explicitly model these fluctuations, rather the data was extensively filtered to remove the oscillations as they were not the focus of the research. Once again it can be seen that even though the conditions are not identical the results show reasonable agreement.

The new SWTB also compares well to the work of Nakashima et al. [NFO+07] who developed a simulation tool to examine the performance of grouser wheels for lunar rovers. For all of their wheel designs, slip ratios and normal loads their experimental *Traction Load* never exceeded 10N and is very comparable to the drawbar pull results from the new SWTB for all of the wheel design, slip ratios and normal loads presented in Figures 2.16 to 2.23.

Experimental values from the new SWTB were also comparable to Bauer et al. [BLB05] who's drawbar pull data has been collected and presented in Table 2.1 and did not exceed 12N. Exact details of the wheel were not published beyond the number of grousers; however, the values are within reason when compared to the data collected by the new SWTB and presented in Figures 2.19 to 2.23.

Table 2.1: Drawbar Pull from Bauer et al. [BLB05]

	Drawbar pull [N]						
9 Grousers	0.74	4.98	8.00	9.94	11.03	10.87	11.61
18 Grousers	0.39	3.92	5.95	7.46	7.30	8.56	9.00
slip ratio	-0.04	0.12	0.25	0.37	0.48	0.57	0.66

There is no standardized test that can be performed to ensure that a new SWTB is producing repeatable and "correct" results. However, one can see that the published values from four different researchers, [BLB05, NFO+07, DGD+11, IMNY07] are close to the experimental readings from the new SWTB lending credibility to the new design of the single wheel testbed and the associated data processing.

2.3.4 Smooth Wheel Phenomena

As mentioned in Chapter 1 repeatable ridges were noticed in the track of a smooth rigid wheel when preliminary testing was performed with the new SWTB. Since all of the test equipment was new, confirmation was required to ensure that the observed phenomena was not an artifact of the equipment. First the wheel was measured with a coordinate measuring machine (CMM) to see if the drive axle and the circumferential centre matched. It was found that the two centres were within $42\mu m$ of each other, and such a small miss-alignment would not cause such obvious ripples in the sand. Thus, a small micro rover was constructed to determine if the phenomena was due to the unique arrangement of the new SWTB.

The 1.6kg micro rover, seen in Figure 2.25, has four wheels. The rear wheels are powered through a 505.9:1 geartrain allowing the wheels to rotate at 9.5rpm which was recorded and monitored through an onboard tachometer. The front wheels are unpowered and rotate freely. The diameter of the front and rear wheels is 100mm. A rotary potentiometer is connected to a spool and is unwound as the rover travels. The signal from the rotary potentiometer is recorded and used to determine the linear displacement of the rover. The data from the tachometer and potentiometer were recorded via LabView and then later post-processed by several custom MATLAB scripts to determine the slip ratio. The post-processing turns the discontinuous saw-tooth signal from the rotary potentiometer into a continuous increasing function so that the displacement and resulting velocities can be found and the slip ratio can then be calculated. Due to non-linearities of the rotary potentiometer some error may be incurred at the transition from 360° to 0°; however, no obvious non-linearities were noticed.

A consistent and repeatable slipping condition was produced by changing the incline of the sand box to 3.5° which produced repeatable ridges in the sand and a slip ratio of 0.8. An example of these ridges can be seen in the top right image of Figure 2.25. The fact that these ridges occur during the operation of a powered rover operating in loose sandy soil confirms that the phenomena is not an artifact of the SWTB but rather an undocumented phenomena which is independent of the testing setup. These ridges warrant further investigation into the cause of the

phenomena and a possible mathematical model to account for them. The data collected from the new SWTB will be used for the investigation due to its high precision and repeatability.

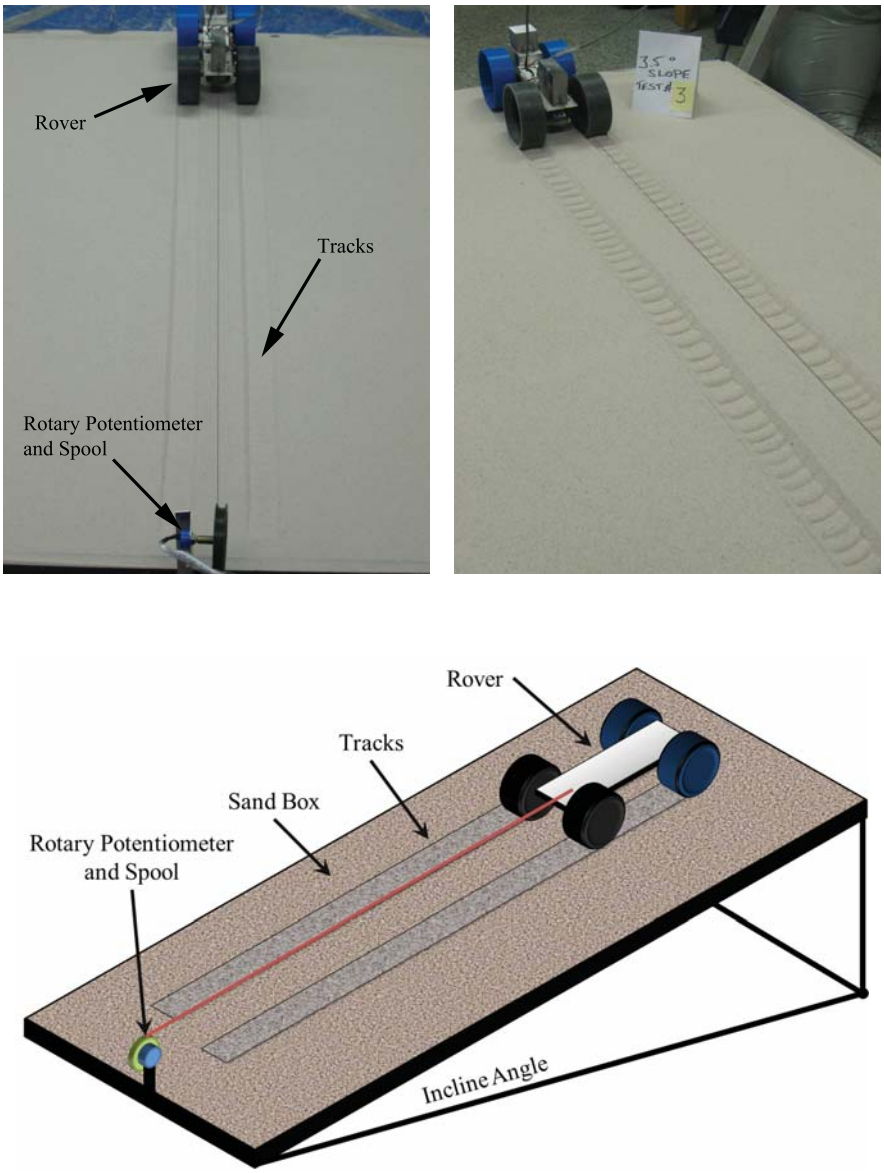

Figure 2.25: Schematic and photographs of the experimental setup of the micro rover. Top Left) 0° incline; Top Right) 3.5° incline sustained operation at a slip ratio of 0.80; Bottom) Schematic of the experimental setup.

2.4 Summary

The work presented in this chapter is summarized below:

1. A simple counter balance can add versatility to many SWTBs.
2. Translating the terrain in a SWTB, rather than the wheel support, is a viable method of conducting terramechanics studies.
3. Over 300 individual experiments were performed on the SWTB, processed and presented showing good repeatability.
4. The new SWTB results compare well to previously published data.
5. The ripple phenomena observed in the track of a smooth wheel is not a function of the SWTB as it was confirmed with a micro rover.

The next chapter will review the literature regarding wheel-soil interaction and the associated modelling techniques which could be used to explain the observed phenomena.

CHAPTER 3

A REVIEW OF TERRAMECHANICS

Terramechanics is used to examine the wheel-soil interaction for the purpose of determining the forces and moments acting on the wheels of an off-road vehicle. These models have also been used to evaluate planetary rovers during their development phase, such as, the European Space Agency's rover chassis evaluation tool (RCET) [MRTG06, PEA+06] and other high fidelity dynamic simulators [JGL+03, SGKR10, BLB05]. Terramechanic models are also used to estimate soil parameters once the vehicle is operational [IKSD04, ID04, HZSA06]. Moreover, they can be used to assist in mobility control of planetary rovers and other lightweight mobile robots [IGD99, IMNY07, INY09].

This chapter presents a literature review of relevant information related to wheel-soil interaction and the associated modelling techniques which are pertinent to examining the phenomena presented in Chapter 1. This chapter is divided into four key sections. The first section presents some of the work done with finite element methods to describe the wheel-soil interaction. The second section discusses analytical terramechanic modelling. The next section of this chapter presents an implementation of an analytical terramechanic model and the fourth section presents a sensitivity analysis of an analytical terramechanic model for the various model parameters.

3.1 Finite Element Modelling

Finite element analysis (FEA) is a powerful tool as it allows researchers to examine endless permutations of a configuration. However, Chiroux et al. [CFJ+05]

identified the fact that FEA has been under-utilized in many engineering situations, including terramechanics. Due to the increase in advanced soil models and contact models in FEA algorithms [Hal07, Lew04], more researcher are turning to FEA in the field of terramechanics. In FEA it is possible to capture the dynamic effects of the grousers since the full wheel and its contours can be modelled in addition to the track left in the terrain by the wheel.

3.1.1 Review of Finite Element Work

The FEA work of Chiroux et al. [CFJ+05] focuses on the dynamic interaction between a wheel and the soil for large rigid wheels, 1.372m in diameter and normal loads of 5.8 and 11.6kN. Their method provides a discrete time history for the simulation and models the dynamic behaviour of the wheel-soil interaction. However, the work concentrated on the stresses and the rebound effects for their terrain. Their model predicted a 25% rebound of the total sinkage deflection; however, for their terrain this rebound effect was not observed. Chiroux et al. [CFJ+05] implemented a Drucker-Prager soil model [DP52] and based their soil parameters data on "Norfolk Sandy Loam" as defined by Block [Blo91]. Chiroux et al.'s work is promising and could be used to examine the oscillatory phenomena which exists for the smooth rigid wheel.

Oscillations in the measured data were observed when grousers were present. Grousers are "paddles" on wheels to provide extra traction and these grousers can pose potential problems for FEA methods. Many FEA algorithms fail at singular points which are often referred to as singularities. Dundurs and Comninou [DC79] say that sudden or abrupt changes in the boundary conditions can lead to singularities. An example of a singular point in a wheel-soil model could be the tip of a grouser on the wheel or at the base of the grouser when the blade joins the wheel as shown in Figure 3.1. At these points the boundary conditions can abruptly change—especially during the blade's entrance and exit of the terrain. But this issue is not insurmountable as Sinclair et al. [SBHS09] described a method for identifying stress singularities by means of numerical divergence checks with at least three meshes of increasing refinement. However, this mesh refinement can be a large arduous task for the complex and dynamic wheel-soil interaction.

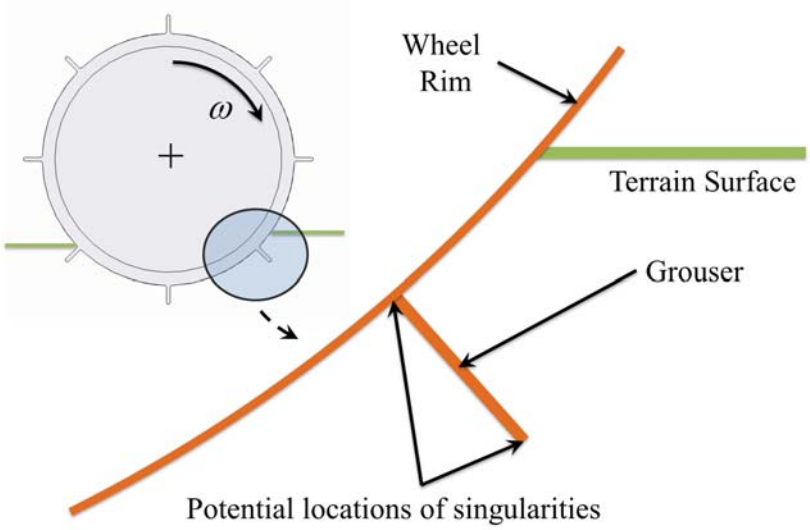

Figure 3.1: Possible locations of singularities in finite element models of a grouser wheel-soil interaction.

A way to avoid singular points with the wheel-soil interaction is the use of Discrete Element Method (DEM) which has the ability to determine microscopic flows or deformation. DEM is a meshless finite element technique and differs from from typical FEA, which relies on an structured grid or mesh. The soil in a DEM analysis is represented as lumped masses; each mass is attached to its neighbour by a spring and damper and shown schematically in Figure 3.2. A DEM algorithm solves the series of equations that are constructed from the interaction of each of the lumped masses and, as a result, the computation time can be very long. Horner et al. [HPC01] have shown that their high resolution 3D DEM model of ten million elements can take up to 16000 CPU hours on a state-of-the-art 256 processor Cray T3E supercomputer. To avoid these high computing times many researches do not use such high resolution models and opt for lower resolution 2D models consisting of 944 to 20,000 elements [NFO$^+$07, KSJN07].

Nakashima and Oida developed an algorithm that marries FEA and DEM to model the wheel-soil interaction [NFO$^+$07, NO04]. The DEM analysis simulates the wheel-soil interaction while an FEA simulation models the deeper layers of the soil where the terrain deformation was not as significant. Nakashima et al.'s model was used for the purpose of simulating different wheel designs for a micro

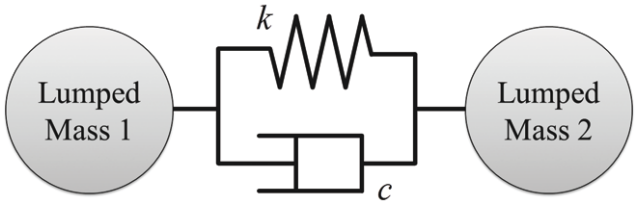

Figure 3.2: Schematic of two lumped masses joined in DEM

lunar rover [NFO+07]. The researchers used conventional Coulomb friction for the tangential forces in the simulation. They claim that no significant difference in the performance was seen as the friction coefficient was varied. It was stated that the DEM model was 'sufficient' in predicting the nominal operating conditions of a planetary rover.

Li et al. [LHC+10] constructed a sophisticated DEM model to examine grouser wheels on lunar soil and gravity. Their model was able to simulate and model the repeatable ridges which were left in the track of the wheel which were noticed in their experimental work. Li et al. did not plot their simulated or experimental forces as a function of time so a clear assessment of the model's ability to simulate the fluctuations about the mean measurements remains uncertain. However, the work shows that DEM has the potential to model the tracks of a grouser wheel.

Recently Schäfer et al. [SGKR10] developed a complex hybrid model which is named Digital Elevation Model or DEM, not to be confused with the DEM (Discrete Element Method) methods described above. Schäfer et al. use a mesh geometry for an arbitrary wheel geometry and computes the stresses for the geometric wheel-soil interaction. The model is based on an animation technique developed by Sumner et al. [SOH99]. Schäfer et al. do not report how computationally expensive their technique is; however, their reference, Sumner et al. [SOH99], reports that a 30 second animation of six wheels can take approximately 125 seconds on Silicon Graphics Power Challenge system with 16 195MHz MIPS R10000 processors and 4GB of memory running in parallel (or approximately 300 seconds when running in series). Schäfer et. al [SGKR10] showed that their preliminary results were able to simulate the dynamic effects caused by the grousers in their torque measurements.

The following summarizes the key points from this review of state-of-the-art

terramechanic finite element research:

1. Chiroux et al. [CFJ+05] have shown that FEA methods can be used to examine a smooth rigid wheel

2. Singularities can occur with wheels with grousers and Sinclair et al. [SBHS09] have proposed methods to avoid these singularities.

3. DEM can be used to model the wheel-soil interaction for a grouser wheel and is capable of modelling the ripples in the track of the wheel [LHC+10].

4. The hybrid method of Schäfer et al. [SGKR10] is able to model oscillations in the torque measurements.

5. The computation time for a high resolution DEM model can reach 16000 CPU hours on a state-of-the-art Cray supercomputer [HPC01].

6. The estimated computation time for the hybrid method of Schäfer et al. [SGKR10] can take over 30 minutes to simulate 30 seconds of animation when operating on 16 CPUs running in parallel on a Silicon Graphics Power Challenge system.

It appears that DEM or the hybrid method could be used to investigate the oscillations observed in the preliminary results of the single-wheel testbed. However, the computation time required to carry out an investigation into the oscillations is prohibitive at this time. Moreover, Wong [Won10] reports that the use of DEM for the "study of vehicle-terrain interaction is still in its developmental stage" as there are many developmental and technical issues that need to be addressed prior for DEM to become the defacto wheel-soil interaction analysis tool. In DEM analysis there is considerable difficulty representing a soil's cohesion and adhesion as DEM does not easily model these tensile forces. Zhang and Li [ZL06] and Asaf et al. [ARS06] have presented methods for modelling these forces but it is not a trivial undertaking. Since finite element algorithms require powerful computers to model the wheel-soil interaction, they are not ideal for end users of motion planning, terrain estimation or multi-bodydynamic simulators. Thus, analytical terramechanic models based on Bekker [Bek69], Wong [Won01] and

Reece [Ree65] are still widely used for motion planning, terrain estimation and multi-body dynamic simulations [DDG+11]. The next section will investigate these analytical terramechanic models.

3.2 Analytical Terramechanic Modelling

Figure 3.3 presents the forces and stresses that an analytical terramechanic model calculates. The smooth rigid wheel model described by Bekker [Bek69] assumes that the pressure p under a wheel is an exponential function of the form:

$$p(z) = kz^n \tag{3.1}$$

where z is the sinkage, n is the sinkage exponent, and k is an empirical coefficient. Bekker proposed that the coefficient k has the form:

$$k = \frac{k_c}{b} + k_\phi \tag{3.2}$$

where k_c and k_ϕ are known as the cohesion modulus and friction modulus, respectfully. Both terms need to be determined experimentally by a Bevameter [Bek69].

3.2.1 Bevameter Testing

Two tests, a penetration and a shear test, combine to form bevameter testing. Figure 3.4 (left) shows a schematic of the in-field ring shear test which is used to determine the shear deformation modulus K and the cohesion c of the terrain. The test involves pressing a ring with grousers into the terrain and rotating the ring. The stress-displacement curve can then be determined and the cohesion and shear deformation modulus can be approximated by this empirical *in-situ* testing method. The cohesion c is the y-axis intercept and the shear deformation modulus K is the first order time constant of the ring-terrain interaction [Bek69]. Figure 3.4 (right) shows a schematic of the penetration system for a bevameter test [Bek69]. The penetration testing allows one to calculate empirical soil constants k_c, k_ϕ and n. The test involves two plates of known dimensions pressed into the soil, and the pressures and the depth of penetration are recorded. The

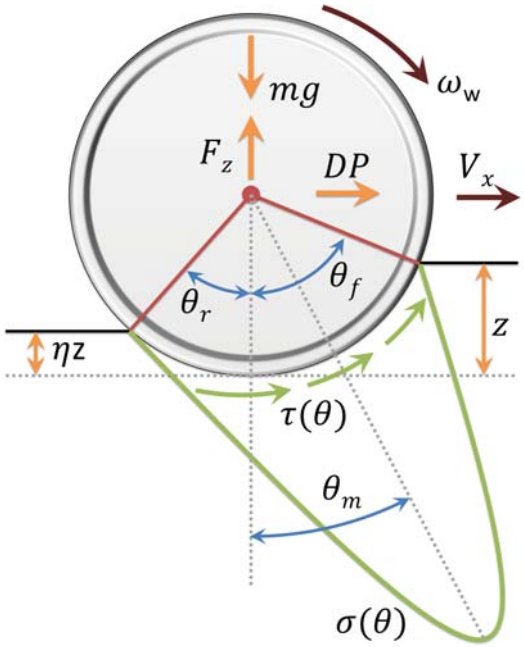

Figure 3.3: Forces and stress acting on a wheel which a typical terramechanic model calculates

soil parameters k_c, k_ϕ and n can be calculated from a minimum of two tests with two different diameter sized pressure plates, b_1, b_2. Bekker [Bek69] and Wong [Won01] have shown that the equations can be written as:

$$\log p_1 = \log\left(\frac{k_c}{b_1} + k_\phi\right) + n \log z \tag{3.3}$$

$$\log p_2 = \log\left(\frac{k_c}{b_2} + k_\phi\right) + n \log z \tag{3.4}$$

These equations would result in two parallel straight lines of the same slope on a log-log scale; a representation can be seen in Figure 3.5. The exponent of deformation n can be calculated by taking the tan of α_s as shown in Figure 3.5. At a given finite sinkage ($z = 1$) the normal pressures of the two plates should not be equal and one could say that:

$$p_1 \mid_{z=1} = \left(\frac{k_c}{b_1} + k_\phi\right) = a_1 \tag{3.5}$$

$$p_2 \mid_{z=1} = \left(\frac{k_c}{b_2} + k_\phi\right) = a_2 \tag{3.6}$$

From the above equation there is now two unknowns and two equations which can easily be solved for and k_c, k_ϕ become:

$$k_\phi = \frac{a_2 b_2 - a_1 b_1}{b_2 - b_1} \tag{3.7}$$

$$k_c = \frac{(a_1 - a_2)\, b_1 b_2}{b_2 - b_1} \tag{3.8}$$

Limitations of Bevameter Testing:

The Bevameter method assumes that the terrain is homogeneous within the depth of interest. However, not all soils are homogeneous and can lead to variations in the pressure-sinkage lines on the log-log scale. To combat this limitation is has been suggested by Bekker [Bek69] and Wong [Won01] to obtain k_c, k_ϕ, and n at varying depths. Wong [Won80] has also suggest that one can also use a weighted least squares method to determine these soil parameters.

Moreover, through empirical experimentation it has been shown that the smallest plate that should be used is 5cm and typically 10cm is the lower limit. This size issue creates a problem when trying to determine the values for planetary rovers whose wheels are often in the lower ranges of the acceptable limits [Bek69, MGS11].

To combat the issues associated with bevameter testing and parameter determination researchers have proposed various other pressure-sinkage relationships.

3.2.2 Alternative Pressure Sinkage Relationships

Wong [Won01] presents the following relationship for organic terrain:

$$p\,(z) = k_p z + \frac{4 M_m z^2}{D_h} \tag{3.9}$$

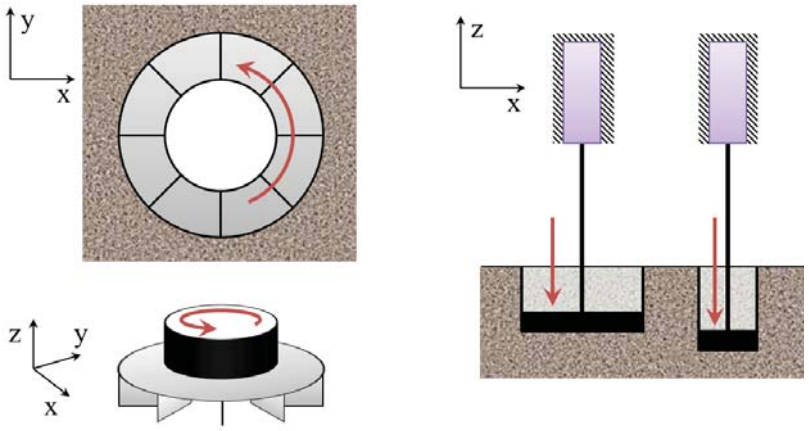

Figure 3.4: Schematic of bevameter: Left) Ring shear; Right) Penetration plates [Bek69]

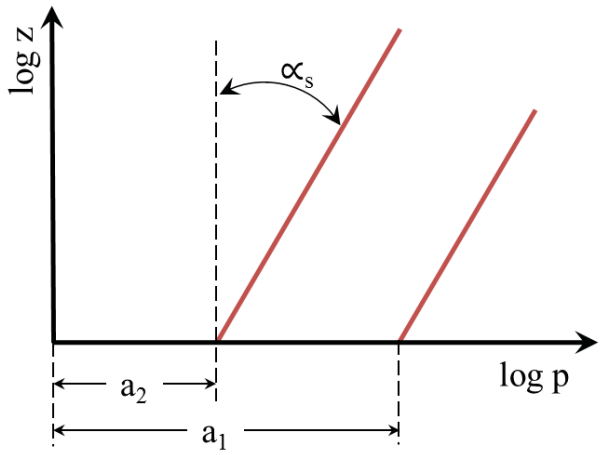

Figure 3.5: Log-log representation of the pressure sinkage relationship [Bek69]

The organic matter stiffness of the peat is considered and captured by the parameter k_p while the strength of the surface mat is modeled by M_m. D_h is the hydraulic diameter of the contact area. In snow and ice Wong [Won01] states that the relationship again changes to:

$$p(z) = p_\omega \left[-\ln\left(1 - \frac{z}{z_\omega}\right)\right] \tag{3.10}$$

where z_ω defines the asymptote of the pressure-sinkage curve while p_ω is an empirical parameter taken as a third of the pressure where the sinkage is 95% of z_ω. Reportedly this model had a 95.8% 'goodness of fit'.

These pressure-sinkage relationships do not help to explain the observed phenomena presented in Chapter 1 for lightweight mobile robots operating in sandy soil. However, recently in 2011, Meirion-Griffith and Spenko [MGS11] proposed a modified pressure-sinkage relationship which modifies Bekker's pressure-sinkage relationship so that it can be applied to wheels smaller than 50cm in diameter and a normal load under 45N. The proposed model is:

$$P = \hat{k} z^{\hat{n}} D^{\hat{m}} \tag{3.11}$$

where D is the wheel diameter and $\hat{k}$, $\hat{n}$ and $\hat{m}$ are fitting constants. The researchers claim that including $D^{\hat{m}}$ ensures that the curvature of the wheel is considered. Meirion-Griffith and Spenko's hypothesis of including a term that considers the wheel's curvature is borne from Bekker's findings. Bekker states [Bek69]:

> Predictions for wheels smaller than 20 inches in diameter become less accurate as wheel diameter decreases, because the sharp curvature of the loading area was neither considered in its entirety nor is it reflected in bevameter tests.

In rolling wheel tests, the modified pressure-sinkage relationship was found to have an average improvement of 41.8% when predicting sinkage values. Before the Meirion-Griffith and Spenko pressure-sinkage model can be used further work would need to be carried out to assess the model's applicability in dynamic

situations as the model was developed through a series of indentation tests and, at this time, the model has not yet been applied to a slipping wheel.

The well used pressure sinkage relationship proposed by Reece [Ree65] modifies Bekker's pressure-sinkage relationship to the following form:

$$p\left(z\right) = \left(ck'_c + \gamma bk'_\phi\right)\left(\frac{z}{b}\right)^n \tag{3.12}$$

Here, k'_c and k'_ϕ are dimensionless soil parameters and replace Bekker's k_c and k_ϕ parameters. Wong [Won01] recommends that for frictionless clay, the k'_ϕ term should be negligible and for cohesionless sand, the k'_c term should be negligible. These recommendations made by Wong come from reviewing Reece's original work [Ree65].

3.2.3 Normal Stress

Wong and Reece [WR67] convert the cartesian pressure-sinkage relationship of Equation 3.1 to a polar form and describe the normal stress field acting on the wheel as:

$$\sigma(\theta) = \begin{cases} r^n k(\cos\theta - \cos\theta_f)^n & (\theta_m \leq \theta < \theta_f) \\ \\ r^n k\left(\cos\theta_f - \frac{\theta-\theta_r}{\theta_m-\theta_r}(\theta_f - \theta_m) - \cos\theta_f\right)^n & (\theta_r \leq \theta < \theta_m) \end{cases} \tag{3.13}$$

where θ_f and θ_r are the wheel sinkage entry and departure angles of the wheel-soil interaction. These angles are computed by:

$$\theta_f = \cos^{-1}\left(1 - z/r\right) \tag{3.14}$$

$$\theta_r = -\cos^{-1}\left(1 - \eta z/r\right) \tag{3.15}$$

where η is a parameter that relates the measured sinkage to the depth of the track after the wheel has passed. Ishigami et al. [IMNY07] indicate that the value of η is a function of the soil properties, slip ratio and wheel surface pattern (grousers). The present authors have found no predictive analytical solution or method to estimate a value for η. Therefore, the value must come from experience, estimation, or through physical testing. The angle θ_m in Equation (3.13) is the angle at

which the maximum normal stress occurs. Some researchers have approximated this angle as the mid point between θ_f and θ_r [SID05]. Wong and Reece [WR67] proposed the following relationship:

$$\theta_m = (b_0 + b_1 i)\,\theta_f \tag{3.16}$$

where $b_0 \approx 0.4$ and $0.0 \leq b_1 \leq 0.3$ and i is the slip ratio. The slip ratio i is defined as:

$$i = \frac{\omega_w r - V_x}{\omega_w r} \tag{3.17}$$

where ω_w is the angular velocity of the wheel, r is the radius of the wheel, and V_x is the translational velocity of the wheel centre. One must also account for the shear stress acting in the wheel-soil interaction.

3.2.4 Shear Stress

The Janosi and Hanamoto equation as defined in [JH61], which is a modification of the Mohr Coulomb failure criteria and accounts for the wheel slippage, is often used to determine the shear stress τ acting along the wheel-soil interface as follows:

$$\tau(\theta) = (c + \sigma(\theta)\tan\phi)\left[1 - e^{-j(\theta)/K}\right] \tag{3.18}$$

where ϕ is the internal angle of friction, K is known as the shear deformation modulus, and j has the form:

$$j(\theta) = r\left[\theta_f - \theta - (1 - i)\left(\sin\theta_f - \sin\theta\right)\right] \tag{3.19}$$

where i is the slip ratio (Equation 3.17). The stresses can now be determined and the forces can be deduced.

3.2.5 Forces

The area integrals of the stresses in the vertical direction yield the vertical force F_z, while the area integrals of the stresses in the horizontal direction provide the drawbar pull DP.

$$F_z = rb\int_{\theta_r}^{\theta_f} (\tau(\theta)\sin\theta + \sigma(\theta)\cos\theta)\,d\theta \tag{3.20}$$

$$DP = F_x = rb \int_{\theta_r}^{\theta_f} (\tau(\theta) \cos\theta - \sigma(\theta) \sin\theta)\, d\theta \tag{3.21}$$

3.2.5.1 Drawbar Pull

The drawbar pull (DP) is a common traction performance metric and is the theoretical tractive thrust (H) minus any resistance (R) to the motion, such as friction, towing resistance, compaction and bulldozing resistance [WD07]. The drawbar pull can be directly computed from the stresses acting on the wheel-soil interface (Equation 3.21); however, some researchers [EPR+05, Bek69] have used an alternative method to calculate the drawbar pull by means of the following equation:

$$DP = H - \sum R \tag{3.22}$$

where the tractive thrust H given by the Bernstine-Bekker equation [EPR+05, Bek69]:

$$H = A_{\odot} c + W \tan\phi \tag{3.23}$$

Where $A_{\odot}$ is the area of the ground contact, c is the soil cohesion, W is the applied weight to the wheel and ϕ is the internal angle of friction. According to Richter and Hamacher [RH99] the dominant resistance is the *Compaction Resistance*, R_c which is defined for a single wheel as:

$$R_c = \frac{k_c + bk_{\phi}}{n+1} b z^{n+1} \tag{3.24}$$

Calculating the drawbar pull with Equations 3.22, 3.23 and 3.24 neglect the effects of slip (Equation 3.17). Lightweight mobile robots, such as planetary rover that are operating in sandy soil, will have wheels that are slipping. Since slip is not accounted for in the drawbar pull calculation of Equation 3.22, this style of analytical terramechanic modelling will not aid in the investigation of the phenomena of the oscillations in the tracks and the measured data of a *slipping* wheel in sandy soil.

To determine the feasibility and parameter sensitivity of an analytical model which accounts for slip, Equations 3.12 and 3.13 to 3.21 were implemented in MATLAB & Simulink. The following section describes the implementation and

results of the analytical terramechanic model.

3.3 Analytical Model Implementation

The analytical terramechanic model was designed to model the same physical scenario as the SWTB so that the full dynamics of the counter balance would not be neglected. The terramechanic model needs to be solved numerically to predict the sinkage, drawbar pull and normal force[1]. The solution methodology used to simulate the model is as follows:

1. Input all model constants and constraints and prescribe the settled or static sinkage value (i.e. 2 [mm]) for $t = t_o$.
2. Calculate θ_f, θ_r and θ_m
3. Compute the normal stress value $\sigma(\theta)$ and shear stress $\tau(\theta)$
4. Integrate the stress from θ_r to θ_f to compute the forces F_z and F_x.
5. Frictional damping F_f of the system must be applied to the vertical direction to account for any losses in the system. Sum the forces in the vertical direction to calculate the sinkage acceleration and then integrate the sinkage acceleration twice to obtain a new sinkage value for the next time-step and return to Step 2 with the updated values.

Step 1 of the simulation is carried out within a MATLAB $*$.m file prior to calling the Simulink $*$.mdl file which computes the remaining steps. Simulation steps 2 through 4 are handled by a `Level-2 M file S-Function` within the Simulink model. The important outputs from the S-Function are the wheel sinkage (z), drawbar pull (F_x) and normal force (F_z). Figure 3.6 shows a simplified schematic representation of the single-wheel testbed pulley system and the corresponding Simulink/Simscape representation of the system that computes step 5 of the simulation methodology. To compute this step one must take the normal force F_z

[1]In this thesis *Normal Load* refers to the applied force due to gravity (mg) acting on the wheel while the *Normal Force* refers to vertical force which is acting on the wheel due to the terrain and computed by the terramechanic model.

into the Simscape environment with an implementation of the pulley counterbalance system where the masses on either side of the pulley are modeled along with the pulley itself. As shown in Figure 3.6, on one side of the pulley there is only the dead weight of counter balance mass. On the other side of the pulley there is the mass of the SWTB rig and the wheel. A grounded `translational damper` block in Simscape attached to the single-wheel testbed rig side accounts for frictional losses in the vertical direction of the system. The viscous coefficient for the damper was set to 800 [Ns/m]. The losses modelled by this damper can come from the linear bearings, linear potentiometer and unaccounted for effects in the terrain deformation. The normal force F_z from the S-Function becomes the forcing function acting on the mass of the wheel side of the counter balance. Simulink/Simscape computes the displacement of the wheel and this displacement is the new sinkage value that is fed back into the soil model S-Function for the next time-step. One will notice in Figure 3.6 that there is a 1:1 gearbox and a zero input torque source between the two sides of the pulley in the Simulink/Simscape model. These blocks were needed to explicitly state the relationship between the two sides of the pulley. One could expand this Simscape implementation to model a full rover with multiple wheels and degrees of freedom and even alter the acceleration due to gravity to simulate Mars or Moon scenarios.

On average this implementation of the terramechanic model takes 2 seconds to compute 1 second of simulation data. This 2:1 computation time is on a i7-Q740 laptop computer with 8GB of RAM running Windows 7, and MATLAB/Simulink is not taking advantage of the multicore processors. In contrast to the speed of most FEA techniques the 2:1 computation ratio lends itself well to motion planning, terrain estimation or multi-body dynamic simulators. Next an analysis needs to be performed using the analytical model to identify any parameters which may help to explain or model the observed phenomena.

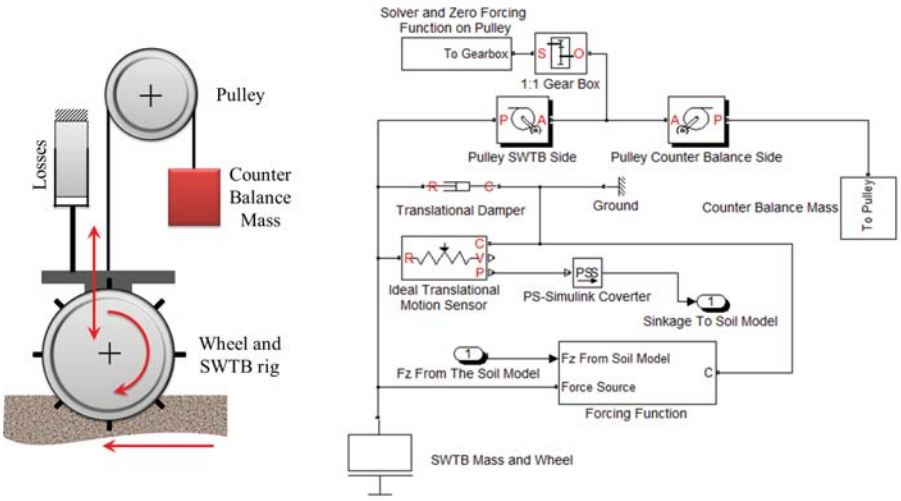

Figure 3.6: Left – Schematic of the SWTB; Right – Simulink/Simscape representation

3.4 Model Parameter Analysis

This section examines the sensitivity of selected soil parameters of the analytical terramechanic model which was implemented with the numerical algorithm described in the previous section. The parameters being examined are listed in Table 3.1 along with the values examined. Each parameter was examined by changing its value while holding all other parameters constant at the "Benchmark". The benchmark values are denoted in Table 3.1 with an asterisk ($*$). The hypothetical wheel used in the analysis has a diameter of 200mm and a normal load of 64N. Figures 3.7 and 3.8 show the sinkage and drawbar pull as a function of slip ratio for the 5 values studied for each parameter. The normal force remained constant at 64N for all of the scenarios and slip ratios examined. The purpose of this analysis is to examine if any of the parameters contained in the terramechanic model could explain the observed phenomena which was presented in Chapter 1.

3.4.1 Cohesion c

The values of cohesion c were small (0, 0.5, 1.0, 1.5, and 1.75 kPa) and are in the range for sandy soil conditions [Won01, HK81]. Figure 3.7 shows that as the cohesion increases the drawbar pull increases and the sinkage decreases for a

given slip ratio. The trend of the sinkage results is linear as a function of slip ratio, and the sinkage decreases as the cohesion value increases. The trends for the drawbar pull results appear to be a function of the slip ratio. The cohesion of the terrain should be constant during an experiment as it is a fundamental soil property and, therefore, it is not likely that a variation in the cohesion could explain the observed phenomena.

3.4.2 Dimensionless Cohesion Modulus k'_c

For the range of the dimensionless cohesion modulus k'_c values studied (10, 20, 40, 80 and 160), Figure 3.7 shows that trends of the sinkage and drawbar pull readings between two k'_c values are relatively similar as a function of the slip ratio. This initial examination suggests that variations in the k'_c parameter could be used to model the observed phenomena; however, there is no physical justification as to how or why k'_c can or would be varying while a wheel is moving through the terrain.

3.4.3 Soil Weight Density γ

The range of the soil weight density γ examined in this sensitivity study is within the typical range of many sands (12-16000 N/m^3) [HK81]. Figure 3.7 shows that there is a decrease in the sinkage as the density increases, which is intuitive: as the soil becomes more dense, the harder it is to sink into the terrain. The figure also shows that at the density increases, there is a small decrease in the drawbar pull for a given slip ratio and the trends of the result do not vary as a function of slip ratio.

Density of a granular material can vary if vibrated or shaken—this is how crushed stone substrates for roadways are compacted prior to paving. It is possible that there are small vibrations which cause a slight variation in the density of the loose sandy terrain as a wheel travels over it in the SWTB. This small variation in the density would result in small variations in the sinkage and the drawbar pull for a given slip ratio. The results of this sensitivity analysis suggest that small variations in the density could be playing a role in the phenomena observed in Chapter 1. Moreover, a change in density compliments the domination of compaction resistance which Richter and Hamacher [RH99] identified for planetary micro rovers, because compaction suggests a change in density.

3.4.4 Dimensionless Friction Modulus k'_ϕ

The results in Figure 3.7 of the analysis yielded virtually identical results to the dimensionless cohesion modulus. Thus, it is possible that k'_ϕ could be varying during an experiment; however, for a given amplitude of oscillation the variation is dependant on the original value of k'_ϕ and there is no physical reason explaining how or why k'_ϕ is varying as the wheel travels through the terrain.

3.4.5 Shear Deformation Modulus K

For sandy soils the shear deformation modulus K is very small [HK81, Won01, ID04]. Figure 3.8 shows that the drawbar pull values of the terramechanic model is very sensitive to the value of the modulus, while the sinkage exhibits virtually no variation as the values increase. This decoupling of the sinkage and drawbar pull results suggest that it can be used to aid in tuning of a terramechanic model so that the model can estimate the mean values of the sinkage and drawbar pull. Ishigami et al. [IMNY07, Ish08] proposed four different empirical relationships which related the shear deformation modulus as a function of the steering angle (or slip angle) and the terrain. These relationships allowed for increased performance to estimate the mean values of the drawbar pull for the new three dimensional *wheel-and-vehicle dynamic model*. Due to the high sensitivity and the known use of the shear deformation modulus being used as a parameter to model the mean values for a terramechanic model, the shear deformation modulus is not well suited to model the observed phenomena.

3.4.6 Sinkage Exponent n

Figure 3.8 shows that, as the sinkage exponent increases, the sinkage and the drawbar pull also increase. The variation in the sinkage and drawbar pull appears to be linearly related to the change of the sinkage exponent. This result suggests that variations in the sinkage exponent n could be used to model the observed phenomena; however, there is no physical justification as to how or why n is varying as the wheel travels through the terrain.

3.4.7 Internal Angle of Friction ϕ

Figure 3.8 shows that the drawbar pull increases as the internal angle of friction increases. The sinkage exhibits no sensitivity to variations in the internal angle

of friction for the values studied. Since the sinkage does not vary as a function of the internal angle of friction, this parameter does not assist in explaining the observed oscillations in the drawbar pull.

3.4.8 Rear of Wheel Sinkage Relationship η

Figure 3.8 shows that the drawbar pull and the sinkage are highly sensitive to variations in the rear of the wheel sinkage relationship term η. Ishigami et al. [IMNY07] stated that the value of η is a function terrain, slip ratio and the surface of the wheel (grousers). It is possible that variations in η could explain or be used to model the observed phenomena presented in Chapter 1. However, if one varies η it is directly linked to the sinkage calculations of Equation 3.15, meaning, it does not explain how or why the sinkage is changing—only that it is. The root cause of the phenomena would remain unaccounted for. Moreover, varying η conflicts with published work, as Iagnemma and Dubowsky [ID04] used experimental observation and prescribe η to zero for various terrains. Ishigami et al. [IMNY07] set η at values between 0.9 and 1.1 depending on the operating conditions but did not mention that it varied during the course of an experiment. During testing on the new SWTB it was difficult to quantify any variations of η as a function of time and thus an empirical visual estimation was made for each test case.

Table 3.1: Soil Parameter Examined in Sensitivity Analysis

Parameter	Test 1	Test 2	Test 3	Test 4	Test 5	Units
c	0	0.50	1.00*	1.50	1.75	kPa
k'_ϕ	10	20	40*	80	160	–
k'_c	10	20	40*	80	160	–
K	0.005	0.01	0.03*	0.05	0.06	m
ϕ	20	25	30*	35	40	Degrees
n	0.9	0.95	1*	1.05	1.1	–
γ	12000	13000	14000 *	15000	16000	N/m^3
η	0	0.15	.5	.75	1*	–

* Benchmark value

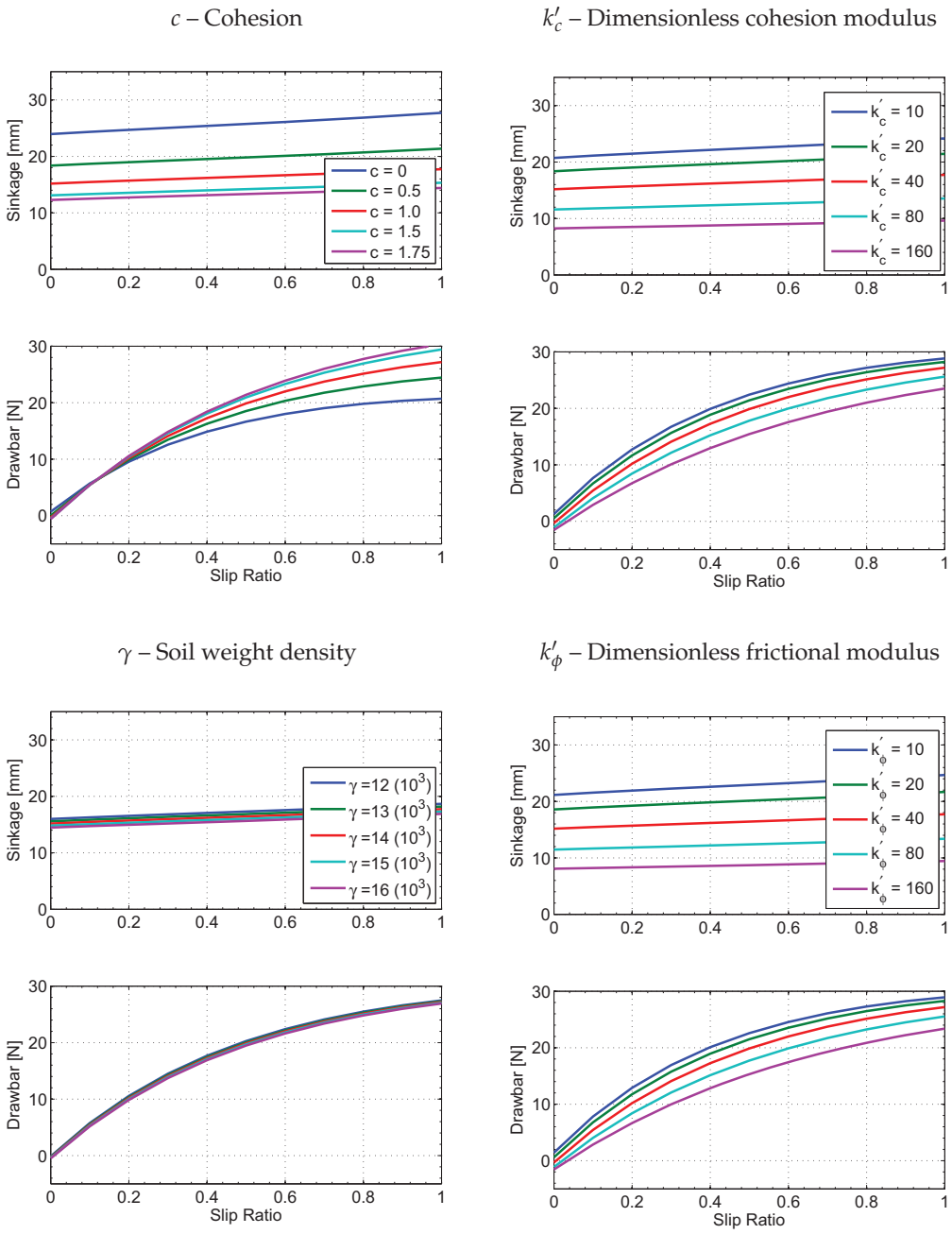

Figure 3.7: Sensitivity Analysis for cohesion c, dimensionless fiction and cohesion modula k_c', k_ϕ' and the internal angle of friction ϕ.

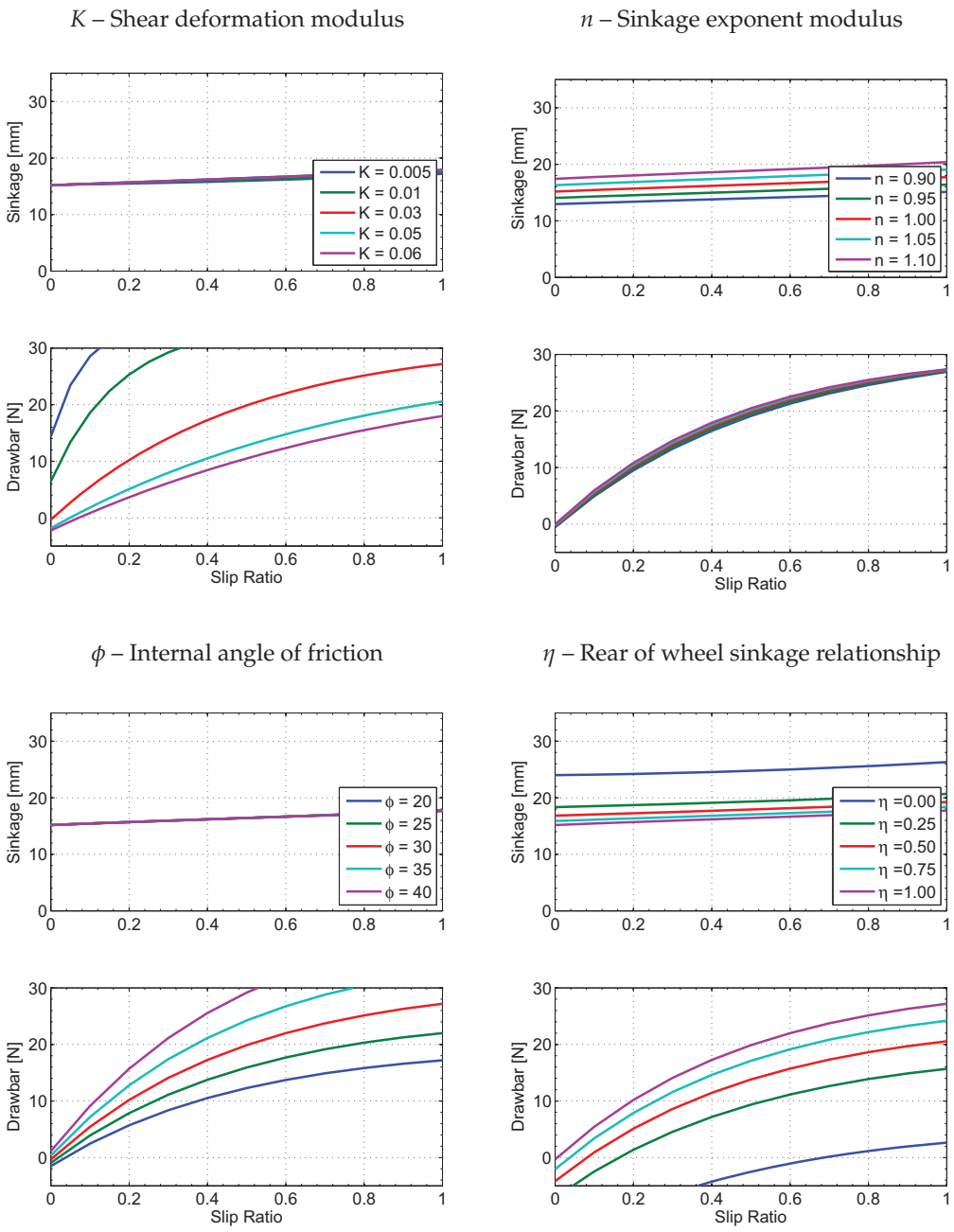

Figure 3.8: Sensitivity Analysis for the shear deformation modulus K, sinkage exponent n, soil weight density γ and the rear of wheel sinkage relationship η.

3.5 Discussion of Analytical model

The preceding section outlined a traditional terramechanic model for a slipping wheel. The basis of this model is one of the most common forms of a terramechanic model for modelling the wheel-soil interaction [Lya10]. Due to it's macro scale and speed, the analytical model is well suited for motion planning, multi-body dynamic simulations and parameter estimation. However, this model does not explicitly compute nor can it accurately compute the state of stress of a point within the wheel or the terrain, especially when grousers are present.

Even though the traditional terramechanic model is not able to capture the full dynamic response, researchers have adapted the model parameters to help estimate the effect wheel grousers have on the mean values of the forces acting on the wheel. For example, Iagnemma et al. [IBD04] proposed that increasing the effective radius of the wheel can help account for the presence of grousers. The rational for this suggestion stems from the fact that, when grousers are present, the radius at which the shear stress acts is no longer at the wheel peripheral, as assumed in the smooth rigid wheel model. Rather, the soil is now shearing at some distance away from the wheel, typical past the grouser length, due to the presence of the grousers. Ishigami et al. [IMNY07] indicate that the departure angle (related to η) can be used to help model the grousers. The departure angle is directly affected by the grousers since a grouser can transport material from beneath the contact interface and deposit the material behind the wheel. Ishigami et al. [INY09] also indicate that the shear deformation modulus K can be adjusted to represent the effects of grousers on the wheel because grousers will affect the shear stress. While these methods can be used to help predict the mean values of the wheel sinkage and forces when grousers are present, the observed dynamic oscillations still remain unaccounted for. Ding et al. [DDG$^+$11, DGD$^+$08] has stated that high-fidelity and high-speed simulation systems are a *key resource for designing* planetary rovers. Therefore, to improve the fidelity of modelling the wheel-soil interaction without sacrificing speed, analytical terramechanic modelling will be advanced for this doctorial research.

The values for the soil parameters used in the analytical model throughout this research were determined as follows: the internal angle of friction and the

shear deformation modulus were experimentally determined through laboratory testing to be 28° and 0.036m, respectfully. The internal angle of friction was determined through a series of direct shear test while the shear deformation modulus was determined through a series of ring shear tests. The unit weight density of the dry loose sandy soil was measured to be 13734 N/m^3 and based on 5 tests. The rear of wheel sinkage relationship η was estimated through visual observations during testing on the SWTB and recorded. Many researchers [Won01, Bek69, ID04] have stated that, for sandy terrain, the sinkage exponent is or very close to unity; therefore, n has been set to 1. Citing Reece's original work [Ree65], Wong [Won01] suggests that for dry, cohesionless sand, k'_c should be negligible; therefore, k'_c has been set to zero thus making the cohesion c value irrelevant. Leaving only the dimensionless friction modulus as an empirical tuning parameter. It was found that the manually tuned value of $k'_\phi = 80$ worked sufficiently well for a majority of the cases studied in this research. These parameters are summarized in Table 3.2. The specific sandy soil used in this doctorial thesis does not explicitly match a Mars terrain simulate discussed by Perko et al. [PNG06]. However, the values of the soil parameters used in this thesis are comparable to the range of soil properties discussed by Perko et al..

Table 3.2: Summary of Final Parameters

Parameter	Value	Unit
c	0.00	kPa
k'_ϕ	80.00	–
k'_c	0.00	–
K	0.036	m
ϕ	28	degrees
n	1	–
γ	13734	N/m^3
η	0.6 - 1.10	–

The next chapter will examine how the analytical terramechanic model can be modified to account for the observed dynamic oscillations.

CHAPTER 4

SMOOTH WHEEL MODEL

This chapter extends traditional terramechanic modelling for lightweight mobile robots operating on sandy soil to incorporate the fluctuations in the forces observed during experimental work with a smooth rigid wheel. To model these fluctuations, a new dynamic pressure-sinkage relationship was developed. The resulting two-dimensional model is validated with the unique single-wheel testbed designed from a Blohm Planomat 408 computer-numerically-controlled (CNC) creep-feed grinding machine. For the experimental conditions used in this research, the resulting model is able to predict the mean and fluctuating values in the sinkage, drawbar pull, vertical forces for a variety of slip ratios and normal loads tested with a rigid smooth wheel operating in sandy soil.

4.1 Introduction

During testing of a smooth rigid wheel on the SWTB, a steady-state ripple patterns was noticed in the wheel markings left in the sandy soil, along with distinct and repeatable oscillations in the measured wheel-soil interaction force and torque data. The single-wheel testbed research supported by NASA and performed by Apostolopoulos et al. [AWHT03] also revealed repeating ridges 5cm wide and 3cm tall in the resulting wheel track. Apostolopoulos et al.'s [AWHT03] wheel had a mass of 15.2 kg, a radius of 70cm along the compressed axis, and a contact width of approximately 1m. In the images presented within Ishigami's PhD thesis [Ish08], similar repeating ridges were also noticed in the track of a smooth rigid wheel operating in a Lunar simulant or Toyoura Sand. Ishigami's

work did not mention or focus on these ridges in the wheel track but rather the overall terramechanics for lunar exploration robots.

Recent wheel-soil interaction models, such as Ishigami et al. [IMNY07], have been developed to capture the mean forces acting on a wheel. Ishigami et al. [IMNY07] refined the traditional Bekker formulation [Bek69] and referenced other researchers in the field of terramechanics such as Wong [Won01], Reece [Ree65], Hanamoto [JH61] and Hegedus [HU60] to validate a three-dimensional model that accounts for slippage and lateral forces. However, the model does not account for the steady-state oscillations in the measured data observed by the present author. Such variable loading is often detrimental to drivetrains and various vehicle components; therefore, an advancement in the fidelity of current models needs to be made to fully capture these effects and assist in the design of planetary rovers and other lightweight mobile robots.

4.2 Model Development

The equations presented in this section appear also appear in Chapter 3; however, they have been repeated here for readability purposes. There are many different methods of modelling the wheel-soil interaction including analytical [Bek69, Won01, Lya10] and finite element [Fer04, NFO$^+$07, KSJN07] models. The present work is based on traditional analytical terramechanics approaches described by Bekker [Bek69] and Wong [Won01]. As shown in Chapter 3 traditional terramechanics approaches [Bek69, Won01] calculate the stresses and forces acting on the wheel by assuming that the pressure p under a sinking wheel is an exponential function as follows:

$$p(z) = kz^n \tag{4.1}$$

where z is the sinkage, n is the sinkage exponent, and k is an empirical coefficient.

The corresponding normal stress distribution under a moving wheel can be represented by the following equation as described by Wong and Reece [WR67]:

$$\sigma(\theta) = \begin{cases} r^n \left(ck'_c + \gamma b k'_\phi\right) \left(\frac{\cos\theta - \cos\theta_f}{b}\right)^n & (\theta_m \leq \theta < \theta_f) \\ r^n \left(ck'_c + \gamma b k'_\phi\right) \left(\frac{\cos\theta_f - \frac{\theta-\theta_r}{\theta_m-\theta_r}(\theta_f-\theta_m) - \cos\theta_f}{b}\right)^n & (\theta_r \leq \theta < \theta_m) \end{cases} \tag{4.2}$$

where θ_f and θ_r are determined by the geometry as:

$$\theta_f = \cos^{-1}(1 - z/r) \tag{4.3}$$

$$\theta_r = -\cos^{-1}(1 - \eta z/r) \tag{4.4}$$

and η is a parameter that is related to the height of the terrain in the track formed behind the wheel. Ishigami et al. [IMNY07] stated that the value of η can be a function of the terrain, slip ratio and the surface of the wheel. For the present study η was estimated through the observations of the experimental testing. The angle θ_m is the angle at which the maximum normal stress occurs. Some researchers have approximated this angle as the mid-point between θ_f and θ_r [SID05]. Reece and Wong [WR67] proposed the following relationship:

$$\theta_m = (b_0 + b_1 i)\,\theta_f \tag{4.5}$$

where $b_0 \approx 0.4$ and $0.0 \leq b_1 \leq 0.3$ and i is the slip ratio.

The shear stress acting along the full length of the wheel-soil interface is calculated by Janosi and Hanamoto's equation [JH61]:

$$\tau(\theta) = (c + \sigma(\theta)\tan\phi)\left[1 - e^{-j(\theta)/K}\right] \tag{4.6}$$

where ϕ is the internal angle of friction, K is the shear deformation modulus, and j can be written in the form used by Ishigami [IMNY07] as follows:

$$j(\theta) = r\left[\theta_f - \theta - (1 - i)\left(\sin\theta_f - \sin\theta\right)\right] \tag{4.7}$$

The corresponding slip ratio i is defined as:

$$i = \frac{\omega_w r - V_x}{\omega_w r} \tag{4.8}$$

where ω_w is the angular velocity of the wheel, r is the radius of the wheel, and V_x is the translational velocity of the wheel centre. The resulting vertical force F_z, drawbar pull DP and Torque T, are the area integrals of the stresses acting on the wheel surface in the associated directions as follows:

$$F_z = rb \int_{\theta_r}^{\theta_f} \left(\tau\left(\theta\right) \sin\theta + \sigma\left(\theta\right) \cos\theta\right) d\theta \tag{4.9}$$

$$DP = F_x = rb \int_{\theta_r}^{\theta_f} \left(\tau\left(\theta\right) \cos\theta - \sigma\left(\theta\right) \sin\theta\right) d\theta \tag{4.10}$$

$$T = r^2 b \int_{\theta_r}^{\theta_f} \tau\left(\theta\right) d\theta \tag{4.11}$$

4.3 Pressure-Sinkage Relationship

The traditional formulation described in the previous section needs to be further developed to account for the steady-state oscillations in forces of a smooth rigid wheel traversing in sandy soil. Figure 4.1 shows a sample of the ripples left in the sandy soil behind the wheel for a slip ratio of 0.75 under 15N, 48N and 64N normal loads. Examining the wheel track in Figure 4.1, it can be seen that the distance from valley to valley in the ripples is between 20 and 25mm for all three normal load cases. At a slip ratio of 0.75 the CNC grinding machine's horizontal motion was commanded to 54.15 in/min (23mm/s) by the FANUC controller– which means that a sand ripple would be produced at an approximate rate of once per second. Figure 4.2 shows the corresponding wheel torque and drawbar pull plotted as a function of time for the 15N normal load, clearly showing the resulting oscillatory pattern in both signals with a period of approximately 1 second. The correlation between the ripple spacing and period of the oscillations in the measured data was consistent for all other slip ratios and normal loads where the ripples were noticed (positive drawbar pull conditions).

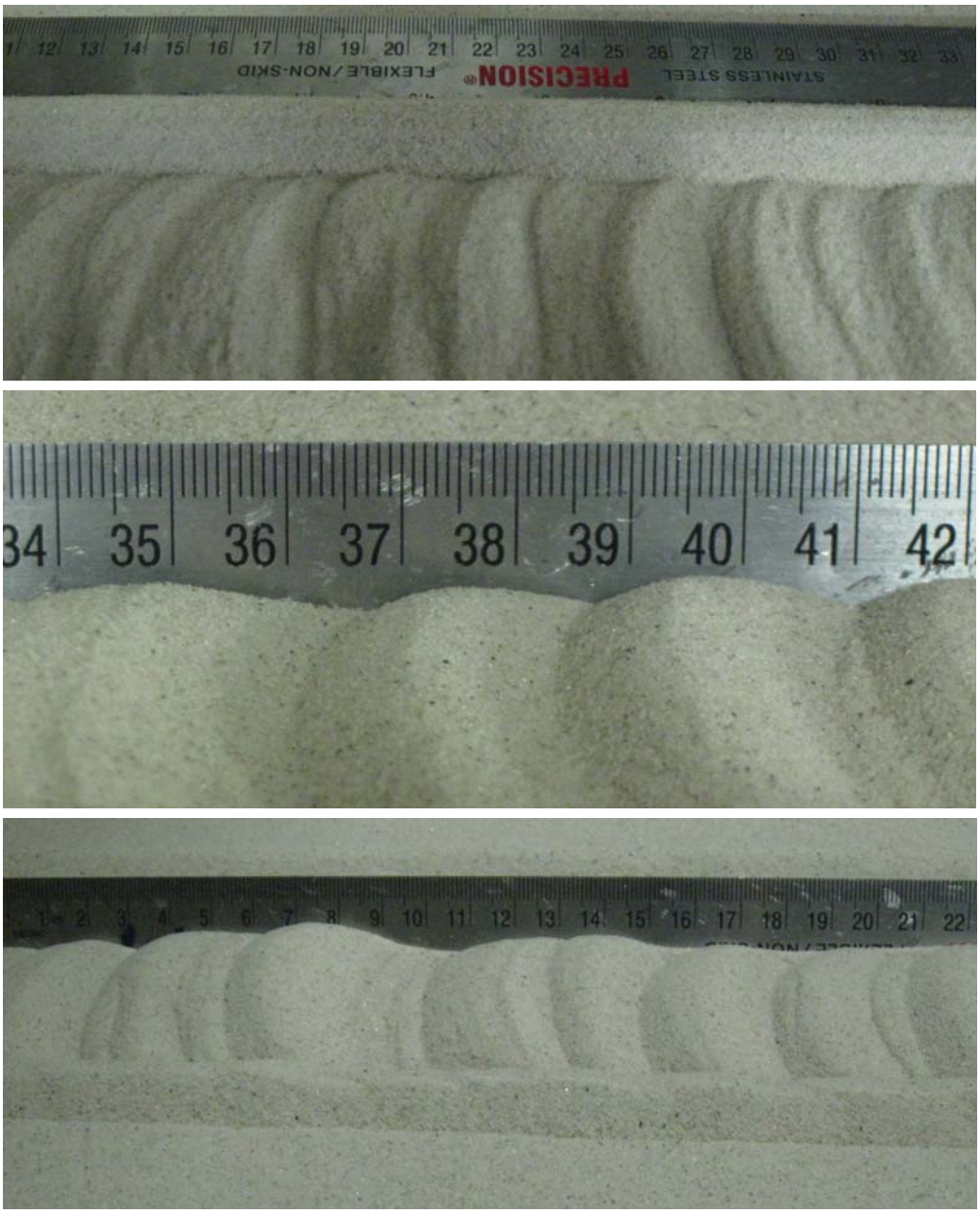

Figure 4.1: Example of tread pattern at 75% slip: Top) 15N normal load; Middle) 48N normal load; Bottom) 64N normal load.

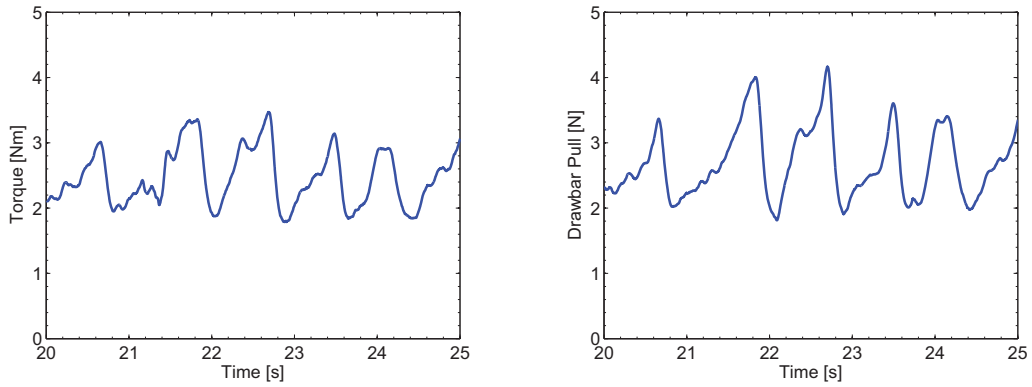

Figure 4.2: Example oscillatory pattern in the torque and the drawbar pull for a slip ratio of 0.75 and a 15N normal load

The observed steady-state oscillation in wheel torque implies that the shear stress $\tau(\theta)$ in Equation (4.11) must be periodically rising and falling. Shear stress is a function of the normal stress $\sigma(\theta)$ as shown in Equation (4.6), and the normal stress is related to the pressure-sinkage relationship shown in Equations (4.1) and (4.17).

Many variations and alternative formulations of the pressure-sinkage relationship have been presented over the years [Won01, Lya10]. A widely used solution for k in Equation (4.1) is presented by Bekker [Bek69, Lya10] as follows:

$$k = \frac{k_c}{b} + k_\phi \tag{4.12}$$

so that, from Equation 4.1

$$p(z) = \left(\frac{k_c}{b} + k_\phi\right) z^n \tag{4.13}$$

where b is the smaller dimension of the wheel's contact patch. As pointed out by Wong [Won01], Equation (4.13) is an empirical equation, and Hambleton and Drescher [HD08] has said that Bekker's parameters k_c, k_ϕ are not 'true' soil constants as their values depend greatly on the equipment and experimental conditions used to obtain them.

Another very common variation of this relationship is the Reece [Ree65] formulation which incorporates the density and cohesion of the soil as follows:

$$p(z) = \left(ck'_c + \gamma bk'_\phi\right)\left(\frac{z}{b}\right)^n \tag{4.14}$$

where k'_c and k'_ϕ are dimensionless pressure-sinkage parameters that have modified the pressure-sinkage relationship, given in Equation (4.1). Reece's model has been verified by penetration tests using various aspect ratios and implies that the pressure p is a function of the terrain's standard material properties including density γ and cohesion c, rather than purely empirical parameters obtained from a Bevameter test. Note that Reece's validated relationships between density and pressure dictate that if the density varies in the terrain, the pressure changes and the associated forces and stresses calculated from this pressure must also vary. Citing Reece's original work [Ree65], Wong [Won01] suggests that for dry, cohesionless sand k'_c should be negligible; therefore, k'_c has been set to zero in the present work because of the dry sand used in the testing. The k'_ϕ term has been left as a manual tuning parameter for the terramechanic model.

It is well known that as the density of a substance increases, the more pressure or force can be exerted on it before it fails. This phenomenon is especially true for granular materials such as sands [HK81]. It is also known that as the void ratio of a sand decreases, the strength of the sand increases [HK81], where the void ratio e is defined as:

$$e = \frac{V_v}{V_s} \tag{4.15}$$

where V_v is the volume of the voids and V_s is the volume of the substance.

Figure 4.3 shows the cumulative percentage of the grain-size from a standard sieve test for the dry sand used in this work. The cumulative percentage graph indicates a relatively normal distribution and such a grain-size distribution suggests that smaller grains could fall into voids created by the larger grains. When the sand is not fully compacted the void ratio would be relatively high—between 0.65 and 0.85 [HK81]; however, if a sample was densely packed the void ratio could drop to 0.2 or lower. This change in the void ratio has a direct effect on the density and strength of the sand [HK81].

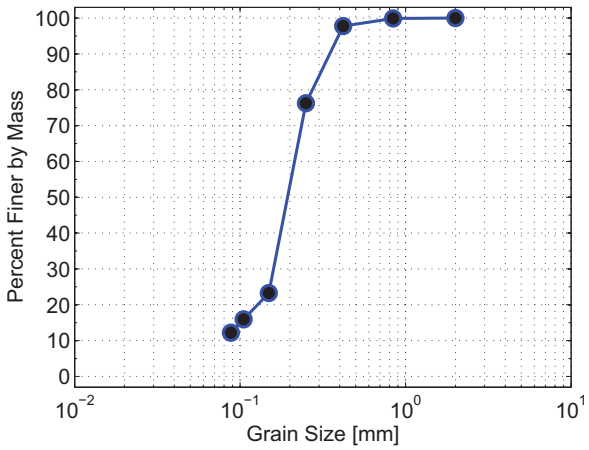

Figure 4.3: Cumulative percent of the grain size of the test sand

As the wheel traverses over the sand there are varying degrees of deformation occurring along the soil-wheel boundary and within the soil structure itself. There is more deformation near the soil-wheel interface and less as one moves farther away from the interfacing surfaces. It is hypothesized that this deformation allows some of the voids to be filled by moving sand particles, essentially lowering the local void ratio, increasing the local density of the sand around the wheel, and increasing the pressure and corresponding normal stress experienced by the wheel (producing the observed oscillations in the measured data). Wong [Won89] described how soils react with varying pressures for repetitive loading of a tracked vehicle. The same theory can be applied to a generalized sample of material that follows the Mohr-Coulomb relationship which is illustrated in Figure 4.4. Referring to the left-hand graph of Figure 4.4 one can see that, as the displacement increases for a given pressure (P_1), the stress level will increase to τ_1. Now, if the pressure were to increase to (P_2), due to a local increase in sand density around the wheel, the stress level would be able to climb to a new level which was not obtainable by the first confining pressure. Likewise if the pressure were to increase further to (P_3) the stress would be allowed to climb even higher. This phenomena could explain the increasing stresses seen in Figure 4.2. To account for the decrease in stress one must look at the right-hand side of Figure 4.4. If one was at stress level τ_3 at a confining pressure of P_3 and the pressure were

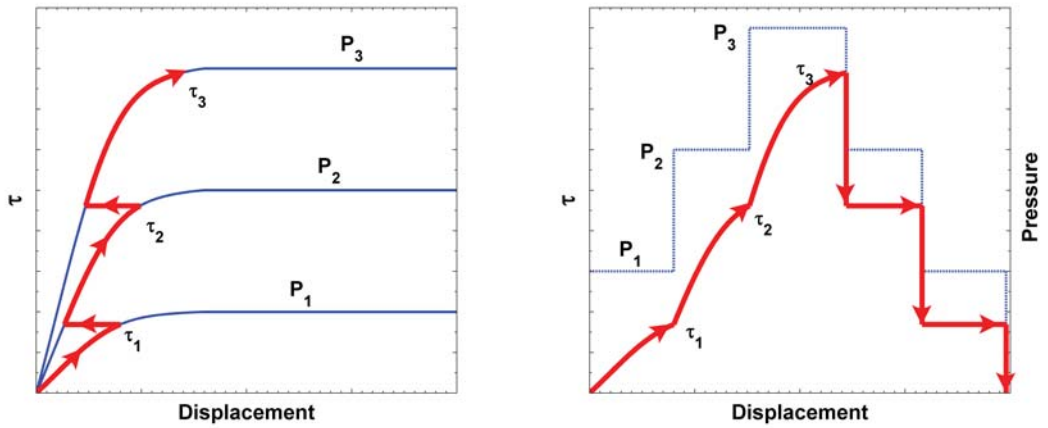

Figure 4.4: Stress, Pressure and Displacement relationships [Won89]

to drop to P_2, as the wheel continues to move forward into fresh (lower-density) sand or due to an initial shear-stress induced failure and loosening of the soil, the shear-stress would drop to the maximum allowable stress level at P_2 (which would be the plastic limit of the P_2 curve). If the pressure were to drop again to P_1, the stress would drop to the plastic region of the P_1 curve. The continuous displacement of the sand around the wheel would cause the density to gradually increase and the process would repeat. This cyclic loading and unloading due to changes in the local sand density could explain how the shear stress levels are able to fluctuate in the steady-state torque measurements of Figure 4.2. To capture this effect analytically, additional terms need to be added to the traditional terramechanic model.

4.4 Proposed Model Parameters

Given the previous discussion on how local density changes around the wheel could be responsible for influencing the stresses experienced by a rigid wheel traversing through sandy soil and producing the observed oscillations in wheel forces, it is proposed that the following new pressure sinkage relationship is able to capture the phenomenon:

$$p(z) = \left(ck'_c + \gamma bk'_\phi\right)\left(\frac{z}{b}\right)^n + A\sin(\omega t + \Phi) \tag{4.16}$$

This formulation takes the common Reece pressure sinkage relationship [Ree65] and adds on an $A\sin(\omega t + \Phi)$ term to account for the dynamic changes which oscillate about the mean pressure $p = \left(ck'_c + \gamma bk'_\phi\right)\left(\frac{z}{b}\right)^n$. The $A\sin(\omega t + \Phi)$ is a simple sine wave function; however, it is recognized that it could be replaced with a more complex Fourier series. The $A\sin(\omega t + \Phi)$ was chosen as an approximation for the observed phenomena because it is simple to numerically integrate and characterize the new A, ω and Φ terms. While higher-order terms in a Fourier series would be difficult to characterize from the current experiments, future work could involve exploring these higher-order terms. The resulting new normal stress equation from Equation (4.16) becomes:

$$\sigma(\theta) = \begin{cases} r^n\left(ck'_c + \gamma bk'_\phi\right)\left(\frac{\cos\theta - \cos\theta_f}{b}\right)^n \ldots \\ \qquad\qquad + A\sin(\omega t + \Phi) & (\theta_m \leq \theta < \theta_f) \\ r^n\left(ck'_c + \gamma bk'_\phi\right)\left(\frac{\cos\theta_f - \frac{\theta - \theta_r}{\theta_m - \theta_r}(\theta_f - \theta_m) - \cos\theta_f}{b}\right)^n \ldots \\ \qquad\qquad + A\sin(\omega t + \Phi) & (\theta_r \leq \theta < \theta_m) \end{cases} \tag{4.17}$$

The Φ term in the proposed model is a simple phase shift that can be used to tune the model results with experimental data. It is proposed that the amplitude A of the normal stress term in Equation (4.17) would be expected to be related to the local change in weight density of the soil $d\gamma$ around the wheel, as well as the contact length l_c since this length characterizes the interface between the wheel and the sand that would cause the sand grains to move and fill in the voids. The

resulting relationship is summarized as:

$$A \propto l_c d\gamma \tag{4.18}$$

where l_c is calculated by:

$$l_c = (\theta_f + (-\theta_r)) \cdot r, \quad or \quad l_c = \theta_{lc} \cdot r \tag{4.19}$$

Note that the proposed relationship in Equation (4.18) also satisfies a dimensional analysis since the change in weight density units [N/m^3] and contact length units [m] would result in an amplitude A with units [Pa] as desired.

To complete the new formulation, it is expected that the frequency ω in Equation (4.16) and (4.17) would be related to the relative motion between the wheel periphery and the terrain. The slip ratio i in Equation (4.8) characterizes this relative motion resulting in the following proposed relationship:

$$\omega \propto i \tag{4.20}$$

4.5 Results

4.5.1 Density

It was hypothesized in Section 4.3 that it is the local density change around the wheel that causes the observed oscillations in wheel force and torque due to the void ratio changing as a slipping wheel engages the sandy soil. Key to validating this hypothesis is to demonstrate that the void ratio of the sand can alter quickly when excited.

Figure 4.5 shows a schematic of the experimental setup used to verify that small displacements can induce a density change in the experimental sandy soil. The sand is contained in a ridge box which is excited by a linear actuator and powered through a function generator. A Point-Grey Dragonfly2 digital camera is attached to the sand box so that it always has the same view of the settling sand and the scale markers inside the sand box. The vertical post in Figure 4.5 is attached to the ground so that a fixed reference fame can be used to determine the horizontal

movement. The camera captures images at a rate of 30 frames per second.

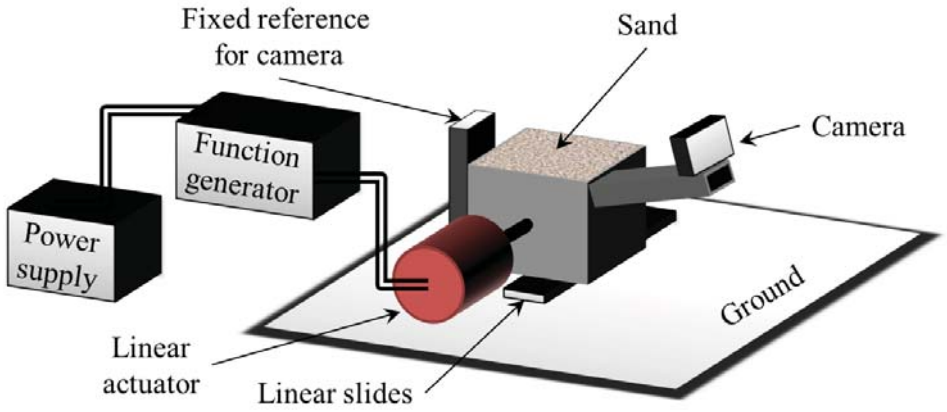

Figure 4.5: Schematic of experimental setup for the sand shacking experiments

Figure 4.6 shows time-lapse images of the experimental sand on a shaker table providing 30Hz sinusoidal excitation with a displacement of 2mm. In the figure the entire sandbox is oscillating in the horizontal direction along linear slides. From Figure 4.6 is was found that within 0.5 seconds there is over a 6.5% percent change in the volume (or density) and within 3 seconds there is a 14% percent change in volume. Therefore, the experimental sand's density is sensitive to relatively small amounts of displacement lending credibility to the proposed model. This result also demonstrates the importance of ensuring that, after each experimental run with the SWTB, the sand be mixed before being leveled so that the initial loose randomly packed structure and void ratio of the sand can be maintained and repeatability of the results can be achieved.

4.5.2 Contact length

Using the SWTB a series of tests were performed by adding mass to the SWTB which resulted in three different normal load conditions (15N, 48N and 64N) for the smooth wheel described in Table 4.1. These normal load conditions refer to the *weight* of the test system. The 15N normal load case was used in this research as a benchmark for the model development and experiments were carried out with this loading condition for slip ratios of 0.25, 0.50, 0.60, 0.75 and 0.90. The 48N and 64N normal load tests were used for model validation and experiments

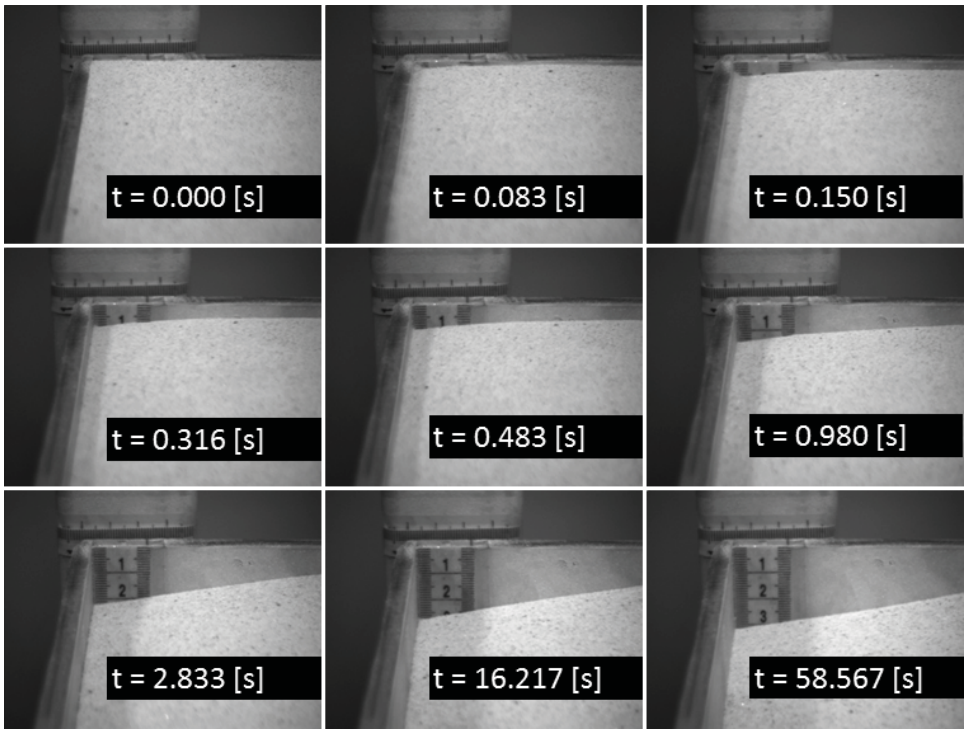

Figure 4.6: Shaking Sand

were carried out with these loading conditions for slip ratios of 0.25, 0.50, 0.75 and 0.95. In each loading case, once the drawbar pull was positive, ripples were noticed in the track of the wheel and corresponding oscillations were observed in the experimental data. By examining the torque data it was found that the measured amplitude of the oscillations grew as the slip ratio and normal load increased. These results can be seen in Figure 4.7 (Top). The graph shows the mean oscillatory amplitude values of the torque and the bounding bars indicate the associated torque oscillation limits for each test case.

It was noticed that the mean of the oscillatory amplitude trend seen in Figure 4.7 (Top) was very similar to that for the sinkage values of the corresponding normal load cases, as seen in Figure 4.7 (Bottom). The contact length l_c is directly related to the sinkage and varies as a function of the normal load, similar to the way the sinkage does. Moreover, l_c is the characteristic length which represents the wheel-soil interface that would cause the sand grains to move and fill in the voids. Plotting the amplitude of the torque as a function of the contact length

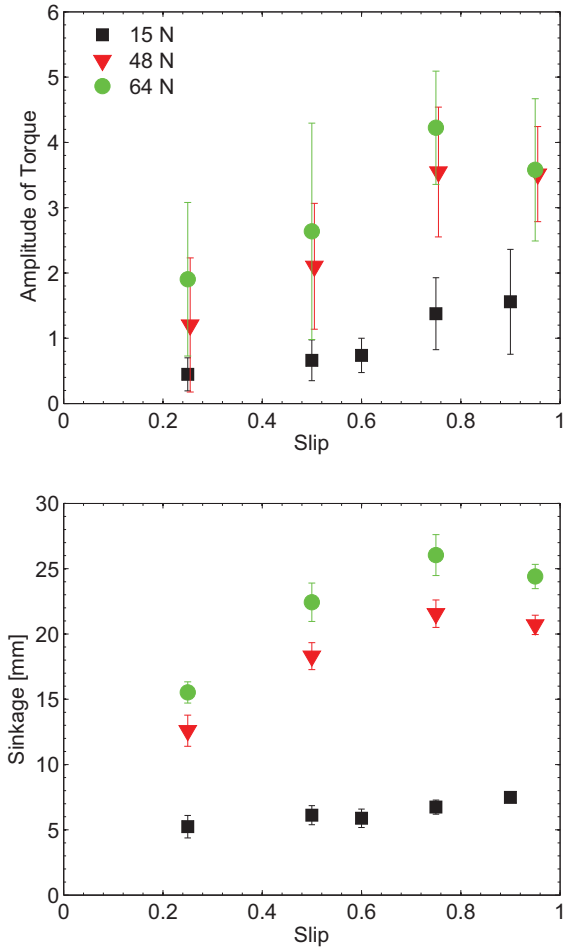

Figure 4.7: Top) Amplitude of torque oscillations as a function of slip ratio. Bottom) Sinkage data as a function of slip ratio

reveals a linear relationship as seen in Figure 4.8. One will also notice that the slope of the fitted line for each normal load condition is very similar. The R^2 value for the $15N, 48N$ and $64N$ normal loads are 0.91, 0.90 and 0.85, respectfully.

Therefore, it can be said that A is a function of the change in the local density and the contact length and can be written as:

$$A = l_c \cdot d\gamma \cdot k'_a \tag{4.21}$$

where k'_a is a dimensionless amplitude factor which was tuned to a value of 2.0 for all test cases in this chapter.

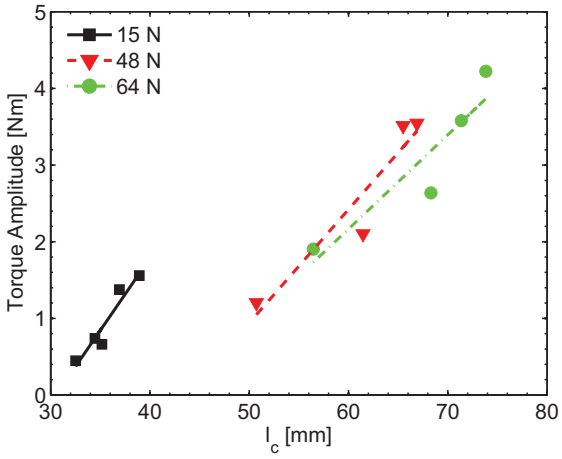

Figure 4.8: Amplitude of torque oscillations vs. the contact length

For terrains that do not exhibit the observed oscillations, k'_a would be zero and, as a result, one would be left with the traditional terramechanic model. It should also be pointed out that if there is no change in density there would be no oscillations and the additional term in the new pressure sinkage equation would be zero. For the simulations carried out in this work a value of $\gamma \cdot 0.10$ was used for $d\gamma$, which implies that the density varied by 10% from the nominal value γ. This change in density appeared reasonable for a slipping wheel given the 6.5% change (0.5s) and 14% change (3.0s) observed in Figure 4.6.

Table 4.1: SWTB Parameters

Parameter	Value	Units
Wheel radius, r	100	mm
Wheel width, b	75	mm
Angular velocity of wheel, ω_w	0.91	rad/s
Sand depth	29	cm
Horizontal travel	950	mm

4.5.3 Frequency

To develop a formulation for the new ω parameter, the frequency of the oscillations was plotted against the slip ratio. The 15N benchmark normal load was used to develop the relationship between ω and i, while the other two normal

loads of 48N and 64N were used as test cases. Figure 4.9 shows the relationship between the frequency and slip ratio for all three normal load cases. A first order least-squares fit was performed on the 15N normal load data, as proposed by Equation (4.20) in Section 4.4, resulting in:

$$\omega = -36.9i + 36.5 \tag{4.22}$$

With an R^2 value of 0.94, this fitted curve reasonably approximates the frequency of the oscillations for all normal loads and slip ratios studied. Even with an R^2 value of 0.94 one must remember that Equation 4.22 is an empirical fit to the given data and, as such, there will be some degree of error associated with the approximation. To visualize the error, Figure 4.10 presents the averaged single sided frequency spectrums of five test runs for a smooth ridge wheel operating at a slip ratio of 0.75 for the three normal loads (15N, 45N and 64N). The oscillation frequency that Equation (4.22) predicts is higher than the actual oscillation frequency from the experimental data. The oscillation frequency of interest is distinguished by the noticeable peak in the FFT. The over prediction is not surprising when one notices in Figure 4.9 that, at a slip ratio of 0.75, the fitted line is higher than all three data points. The maximum error at this particular slip ratio is 0.37Hz; therefore, it is expected that a phase shift will be noticed when overlaying experimental and simulation data as a function of time. One will notice that the actual frequency for all three cases in Figure 4.10 is very close to 1Hz, which corresponds to a horizontal displacement of approximately 23mm at a slip ratio of 0.75. Moreover, when examining the data from Figure 4.10 it can be seen that the data does not produce a discrete peak at a specified frequency but rather a distribution around a frequency. This distribution indicates that one will see variations in the period of the oscillations in the measured data and the spacing of the ripples. Returning to Figure 4.1, the figure shows that the spacing between the ripples is approximately 23mm for all three normal loads, confirming that the ridges in the sand correspond to a repeatable oscillation in the measured data and that these oscillations are independent of the normal load. One will also notice some degree of variation in the oscillations in the ripple spacing as predicted by

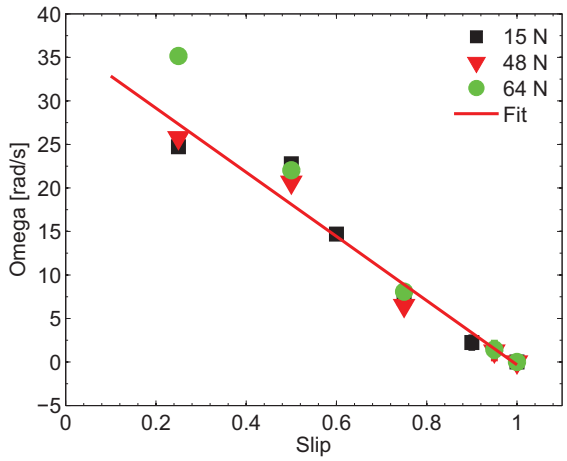

Figure 4.9: Omega vs Slip Ratio curve fitting

the FFT data. The small changes in the frequency of the oscillations in the measured data and the ripples can be attributed to natural density variations in the initial conditions of the terrain.

4.5.4 Simulation and Experimental Comparison

The numerical simulations were carried out in the MATLAB/Simulink environment by taking advantage of the Simscape blockset. The test equipment was described in Chapter 2 and the numerical solution process is similar to what was described in Chapter 3—the modified algorithm can be found in Appendix A. Table 4.2 summarizes the model parameters used. The measurements of interest for the present work are the sinkage, drawbar pull and vertical forces. The new dynamic terramechanic model was calibrated with the tuning case of a 15N normal load and a slip ratio of 0.25 for these three measurements of interest. The performance of the model was first examined by varying the slip ratio at the 15N loading case. The model's performance was then examined by increasing the loading conditions to 48N and 64N while varying the slip ratio at these high normal loads. The model parameters that were tuned for the normal load of 15N and a slip ratio of 0.25 were held constant throughout these simulations.

The only parameter that changed from one test to another is η. For the 15N normal load, η was visually inspected from the experimental work. After a test

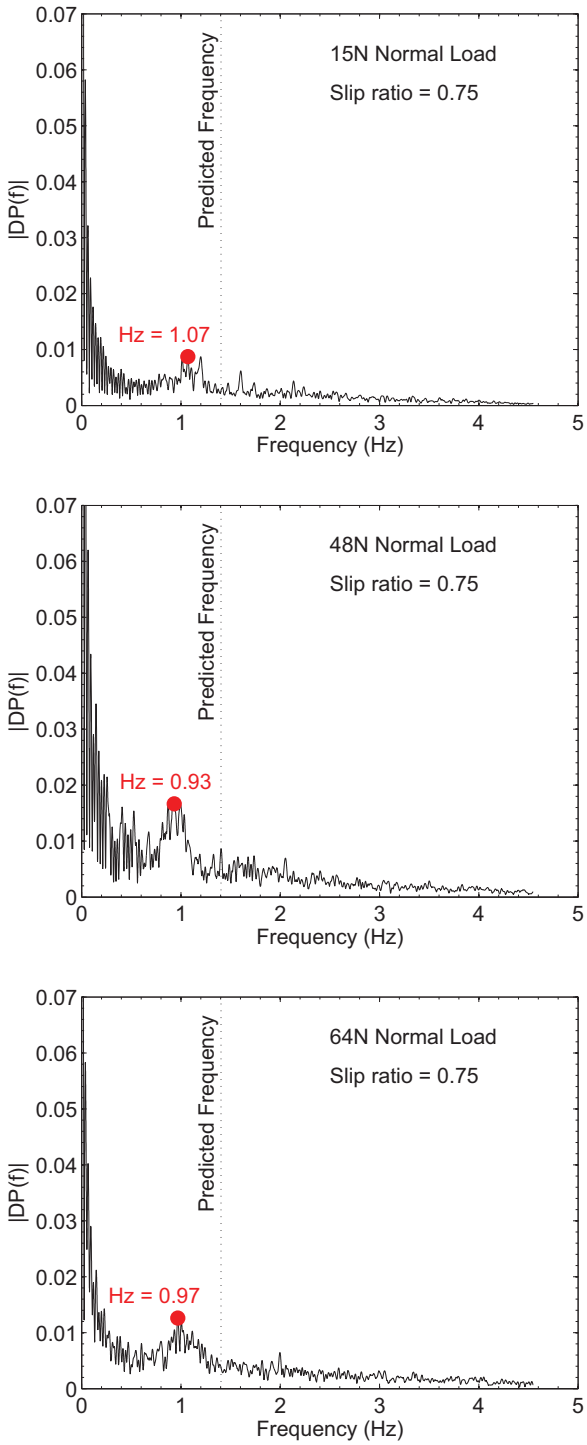

Figure 4.10: Single sided frequency spectrums of a smooth rigid wheel operating at a slip ratio of 0.75 and a normal load of 15N normal load (TOP); 48N normal load (MIDDLE); 64N normal load (BOTTOM)

run the height of the wheel track was compared to the sinkage and a value for η was then calculated. It was found that η was 0.85 for the 0.25, 0.50, 0.6 and 0.75 slip ratio cases and 0.85 for the 0.90 slip ratio case. For the 48N normal load, η was determined to be 0.5 for the 0.25, 0.50 and 0.75 slip ratio cases, and 0.85 for the 0.95 slip ratio case. Lastly, for the 64N normal load, η was approximated at 0.6 for all slip ratio cases. Since the linear velocity of the terrain is altered to control the slip ratio, the duration of the 950mm traverse varied. A 0.25 slip experiment lasts a total of 13 seconds with a steady-state region of 2 to 7 seconds, while a 0.95 slip run will take 207 seconds to complete, with over 200 seconds of steady state operation.

Table 4.2: Model Parameters

Parameter	Value	Units	Comments
c	0.0	kPa	Soil Cohesion
K	0.036	m	Shear deformation modulus
ϕ	28	deg	Internal angle of friction
k'_ϕ	80		Pressure-sinkage modulus
k'_c	0		Pressure-sinkage modulus
k'_a	2		Pressure-sinkage modulus
γ	13734	kg/m^2s^2	Soil weight density
b_0	0.4		Used to determine θ_m
b_1	0.2		Used to determine θ_m
$F_{friction/damping}$	800	Ns/m	Vertical Viscous Friction

It is important to note that the model was tested over a wide range of slip conditions which a planetary rover may encounter. While slip ratios of 0.75 and 0.95 are not ideal, they may be unavoidable. For example, NASA's Mars Exploration Rover, "Spirit", was entrenched for several weeks and periodically operated in high slip conditions [ABIB$^+$10]. As exploration of Mars continues, rovers will likely continue to find themselves in high slip conditions and, therefore, there is a need to better model these operation conditions for designers and mission specialists.

The proposed model is able to approximate the experimental data for many of the test points and cases for the sinkage, drawbar pull and normal force. It should be noted that the new terms in the proposed model which capture the observed oscillations in the measured data do not influence the mean values predicted by

the highly-developed and well-used terramechanic model on which this work is based [Ish08, IMNY07, INY09, Bek69, Won01, Ree65, Lya10, WR67, SID05, IBD04, ISD02, IKSD04, ID04, MGS11]; rather, the predicted oscillation are superimposed onto the mean values. Figures 4.11 shows the sinkage, drawbar pull and normal force plotted as a function of time for a smooth rigid wheel operating at a slip ratio of 0.25 with a normal load of 15N. Table 4.3 shows the RMS data for the tuning case of a slip ratio of 0.25 with a normal load of 15N. One will notice that the sinkage results are very appropriate while the drawbar pull and normal force oscillations are slightly under predicted both visually in Figure 4.11 and in the RMS data presented in Table 4.3. An increase to k'_a would result in an improvement to drawbar pull and normal force oscillations but would significantly compromise the sinkage oscillations results. To examine the effect of k'_a, Figure 4.12 presents the mean adjusted sinkage, drawbar pull and normal force plotted as a function of time for a smooth rigid wheel operating at a slip ratio of 0.25 with a normal load of 15N but with an increasing value of k'_a (1.0, 2.0, 3.0 and 4.0). In these graphs, the mean of the experimental and simulation data has been adjusted to zero for the displayed time frame so that the amplitude and phase of the new model terms can be easily examined and compared. The plots show that as k'_a increases the amplitude of the oscillations increase in all three measurements. When k'_a is set to 3.0 and 4.0 the sinkage oscillations are over exaggerated. Therefore, it was felt that setting k'_a at 2.0 was appropriate by visually inspecting the results of Figure 4.12 and the RMS delta difference was 0.016, 0.232 and 1.102 for the sinkage, drawbar pull and normal force, respectfully.

To highlight the contribution to the established terramechanic model, Figure 4.13 presents the mean adjusted overlays of the predicted and experimental sinkage, drawbar pull and normal force plotted as a function of time. The slip ratios in the figure are 0.25, 0.50, 0.75 and 0.95 for a normal load of 15N. The slip ratio of 0.25 was used as a tuning case for other cases examined in this chapter. The experimental data in these figures are for a single experiment since averaging the data over several experiments would distort the amplitude and phase of the oscillations. RMS data comparing the simulations and the experimental results is complied in Tables 4.3, 4.4 and 4.5 which numerically quantifies the model. The

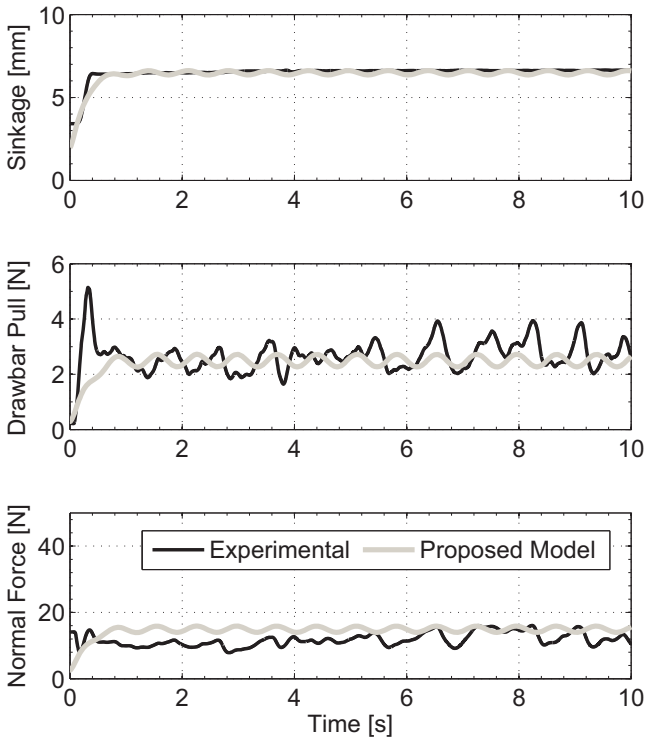

Figure 4.11: Simulation of a rigid wheel operating at 0.25 slip and a 15N normal load overlayed with experimental data

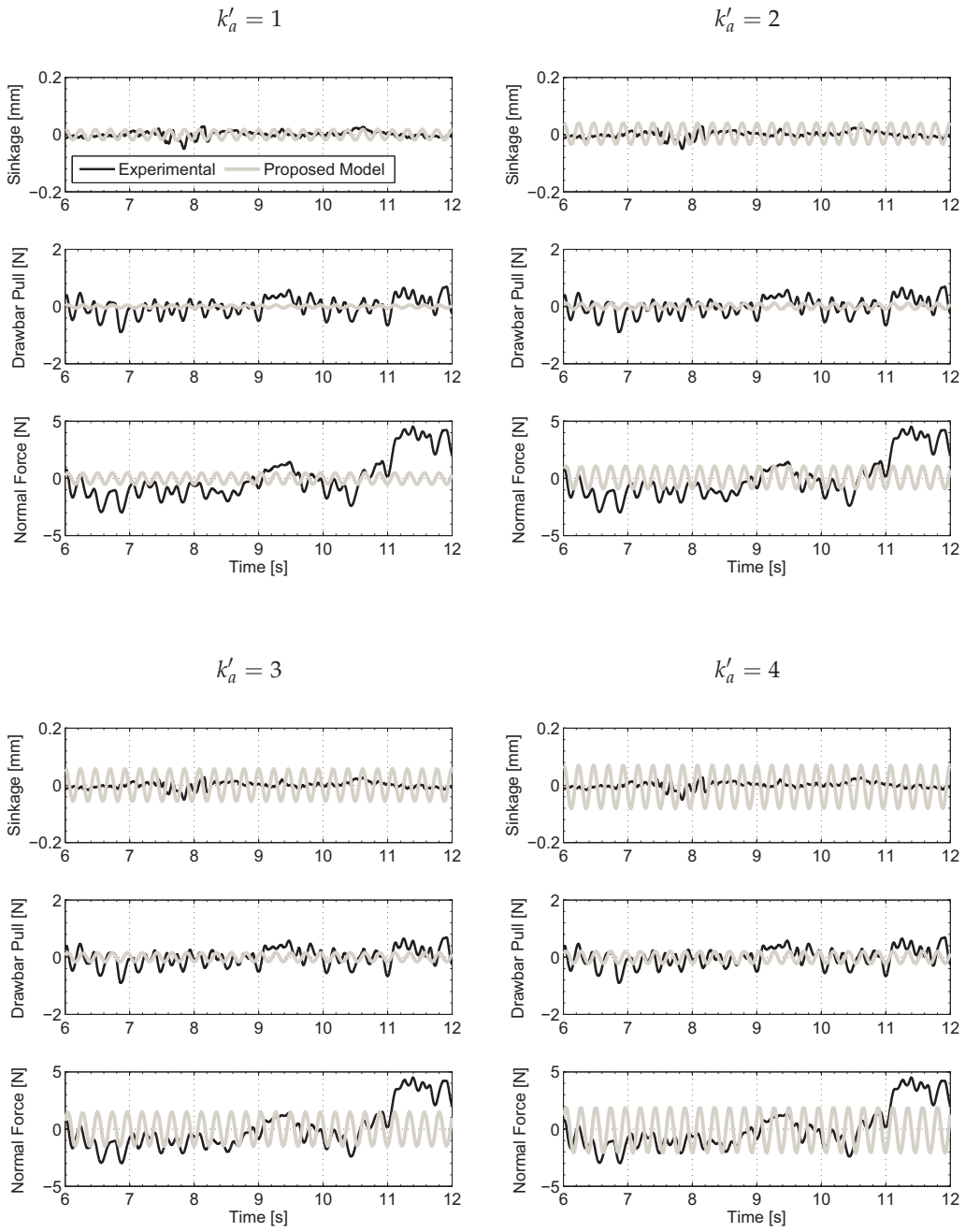

Figure 4.12: Mean adjusted simulation data of a smooth rigid wheel operating at a 0.25 slip ratio with a 15N normal load overlayed with experimental data for various values of k'_a.

table also presents the difference or delta between these two RMS calculations. The RMS data confirms that the dynamic model is able to reasonably capture the dynamic effects for a variety of test cases.

Figure 4.13 shows that the amplitude of oscillation in the sinkage is very low and this observation is confirmed by the RMS values of the sinkage data presented in Table 4.3. It can be seen that the experimental sinkage data does not clearly exhibit an oscillatory pattern. The lack of an oscillatory pattern could be caused by friction or stiction in the linear bearing and potentiometer. Examining the 0.75 slip case (Bottom Left of Figure 4.13) one notices that sinkage oscillations are not present and there is almost no experimental variation for the time span shown. One will also notice in the same test case that the amplitude of the normal force is under predicted. This coupled result suggests that there could be a stiction phenomena which would explain why the wheel is not moving but the normal force is able to vary. Stiction allows one to exert more force on an object with no movement until the force has increased beyond the required break-away force.

Figure 4.13 shows reasonable results for the 0.25 and 0.50 slip ratio cases which is quantified by the RMS data of Table 4.3. The highest slip ratio case of 0.95 (Bottom Right of Figure 4.13) shows reasonable results for the drawbar pull and normal force; however, the sinkage results do not correspond very well. The model is predicting a peak-to-valley oscillation of approximately 0.6mm while the experimental results are showing no indication of these oscillations. A friction phenomena may also be playing a role in these results. At the low normal load of 15N the Coulomb friction model used in this work may not be sufficient to model the full dynamic effects of a smooth rigid wheel operating in loose sandy soil. There is likely a complex friction phenomena (stiction/friction) that is influencing the results at these low normal loads and low speeds. A more complex friction model may increase the accuracy of the terramechanic model; however, further experimental testing would be needed to quantify the friction in the system and this task is not simple or trivial. Adding a simple stiction model which was mentioned previously would not be sufficient or realistic as a simple stiction model would introduce discontinuities in the signals of interest and no noticeable

discontinuities were present in the measured data.

There is, as expected, a phase shift between the simulated and experimental results of Figure 4.13. This phase difference is due to the empirical relationship described by Equation 4.22 which was developed. One will notice that the period of the oscillations does increase as the slip ratio increases for both the simulated and experimental results. Moreover, one will notice slight disturbances in the experimental oscillations. A very noticeable example of these disturbances would be at 7.5 seconds in the 0.75 slip ratio case (bottom left of Figure 4.13) and at 11 seconds of the 0.25 slip ratio case (top left of Figure 4.13). These disturbances could be caused by the sand's natural and inherent local variability in the void ratio and, hence, the density of the terrain is also variable prior to the wheel-soil interaction. It is unrealistic to have a perfectly uniform void ratio in the sand prior to a test even after the terrain preparation (described in 2.2). Therefore, if there is a section with slightly more or slightly less voids in a specific area, then the frequency and amplitude of the oscillations will vary since the sand has a pre-existing condition. On average, the equations presented in Section 4.3 effectively capture the overall phenomena. One could add stochastic variables to the model if these delays or variations are of importance.

Figures 4.14 and 4.15 presents the mean adjusted overlays of the predicted and experimental sinkage, drawbar pull and normal force plotted as a function of time for slip ratios 0.25, 0.50, 0.75 and 0.95, for normal loads of 48N and 64N. At both of these normal loads the model is able to reasonably predict measured data for the 0.25 and 0.50 slip ratio cases; however, at the two higher slip ratios the discrepancy between the predicted model results and the experimental data is larger. It is important to keep in mind that previous terramechanic models would not have predicted any oscillations in the data at these high slip ratios. Also note that, while the dimensionless k'_a term could be increased to better represent the experimental data at these high slip ratios, the sinkage oscillations would also greatly increase. Moreover, one must remember that this model was tuned at a normal load of 15N and a slip ratio of 0.25 so it is not unreasonable to expect some deviation from the predicted and experimental results. In general the model is able to better capture the dynamic oscillations observed in the data in a predictive

mode of operation for both normal load and slip ratio.

Table 4.3: RMS Data for 15N Normal Load

Sinkage in millimeters

Slip Ratio	RMS Experimental	RMS Proposed Model	$\|\Delta\|$ Difference
.25[1]	0.011	0.027	0.016
.50	0.086	0.045	0.040
.75	0.03	0.096	0.067
.95	0.023	0.198	0.175

Drawbar Pull in newtons

Slip Ratio	RMS Experimental	RMS Proposed Model	$\|\Delta\|$ Difference
.25[1]	0.309	0.076	0.232
.50	0.395	0.123	0.271
.75	0.554	0.156	0.397
.95	0.062	0.074	0.012

Normal Force in newtons

Slip Ratio	RMS Experimental	RMS Proposed Model	$\|\Delta\|$ Difference
.25[1]	1.812	0.710	1.102
.50	1.616	0.699	0.917
.75	2.133	0.656	1.477
.95	0.382	0.238	0.144

[1] Denotes the slip ratio which the model was tuned with

Table 4.4: RMS Data for 48N Normal Load

Sinkage in millimeters

Slip Ratio	RMS Experimental	RMS Proposed Model	$\|\Delta\|$ Difference
.25	0.359	0.054	0.305
.50	0.100	0.084	0.016
.75	0.231	0.170	0.061
.95	0.167	0.273	0.106

Drawbar Pull in newtons

Slip Ratio	RMS Experimental	RMS Proposed Model	$\|\Delta\|$ Difference
.25	0.882	0.22	0.662
.50	1.032	0.214	0.818
.75	1.251	0.264	0.986
.95	1.215	0.137	1.079

Normal Force in newtons

Slip Ratio	RMS Experimental	RMS Proposed Model	$\|\Delta\|$ Difference
.25	2.558	1.562	0.996
.50	3.311	1.366	1.945
.75	4.666	1.21	3.456
.95	4.511	0.337	4.174

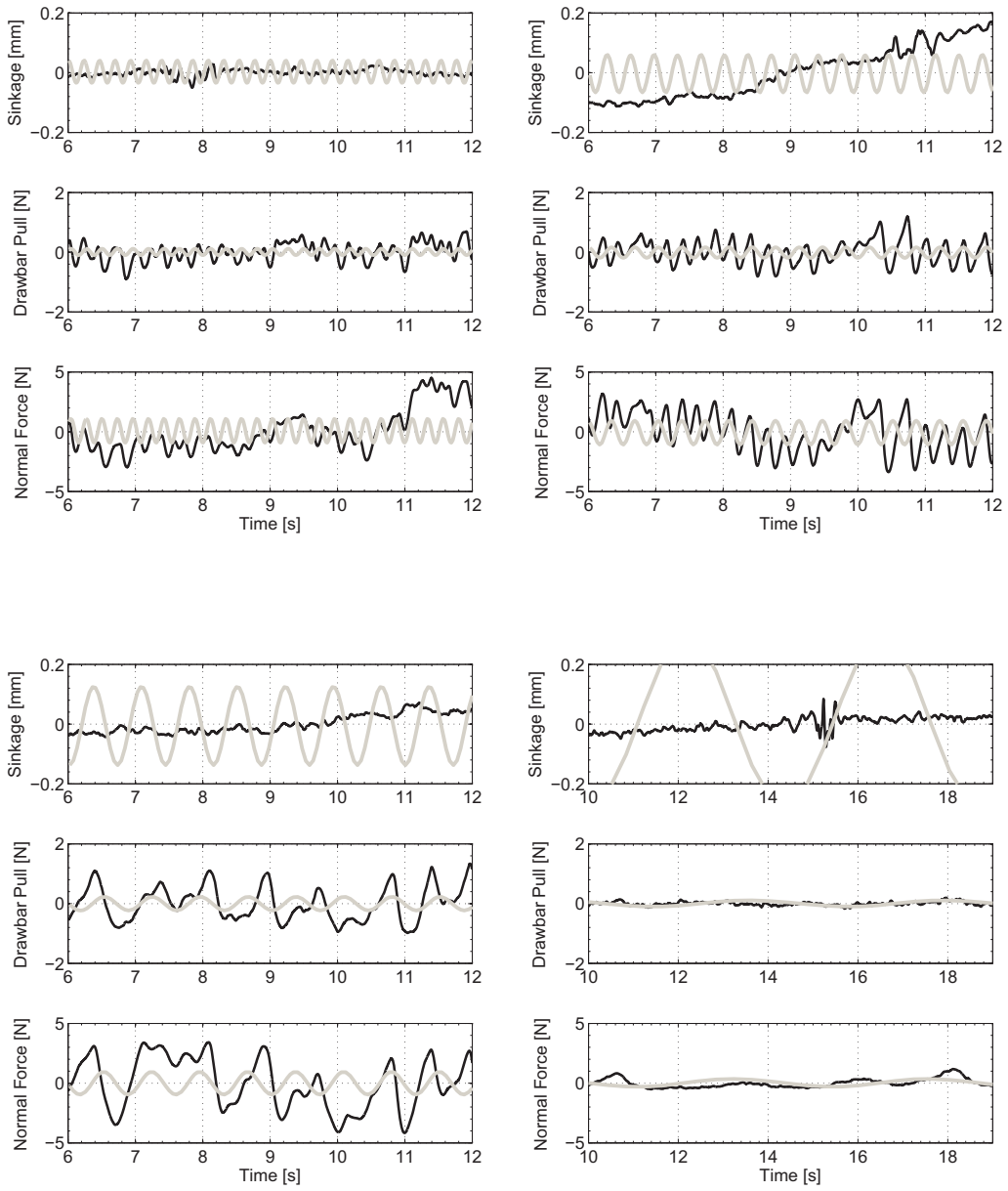

Figure 4.13: Mean adjusted simulation data of a smooth rigid wheel operating with a 15N normal load overlayed with experimental data. Top Left) 0.25 slip ratio; Top Right) 0.50 slip ratio Bottom Left) 0.75 slip ratio; Bottom Right) 0.95 slip ratio

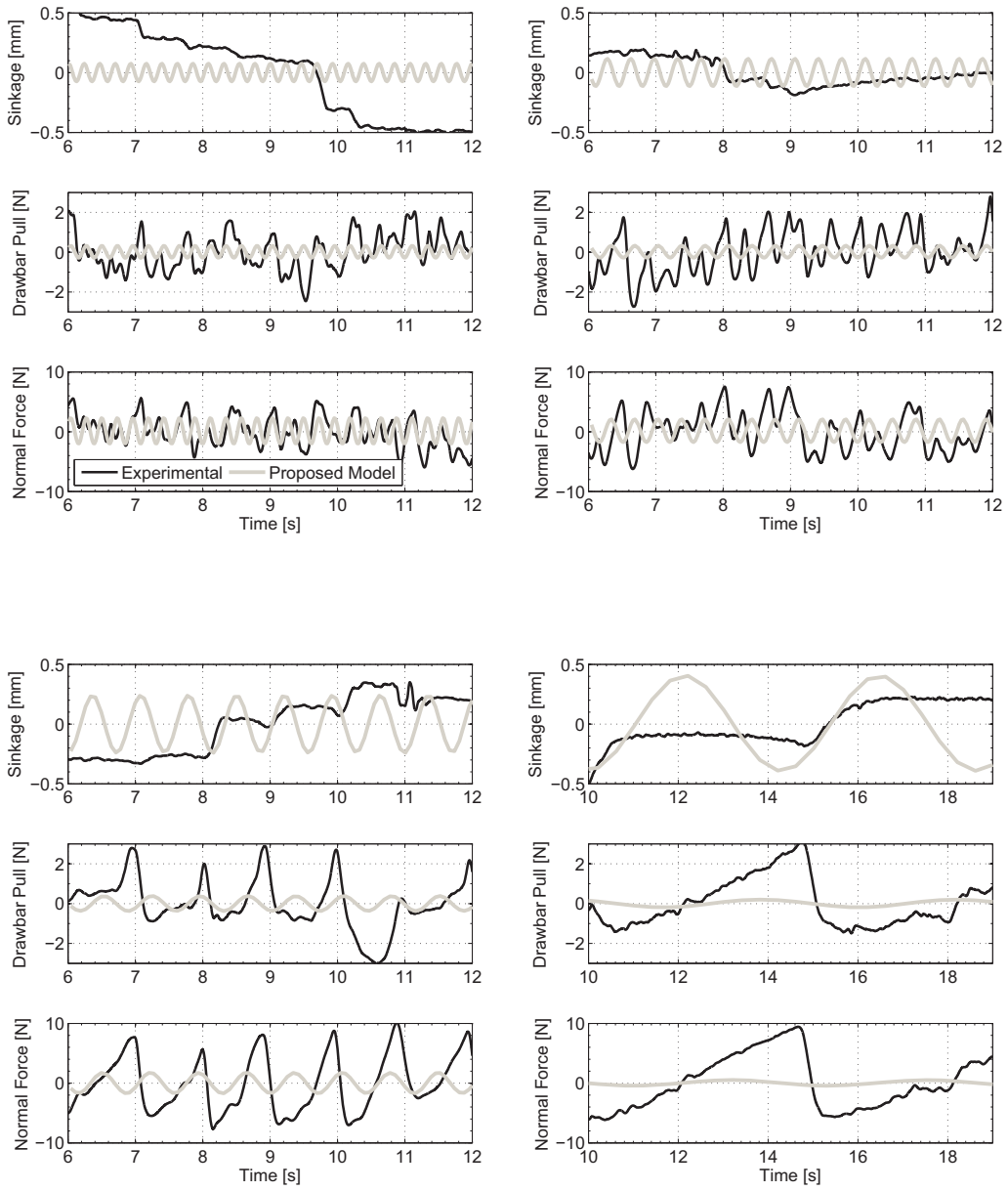

Figure 4.14: Mean adjusted simulation data of a smooth rigid wheel operating with a 48N normal load overlayed with experimental data. Top Left) 0.25 slip ratio; Top Right) 0.50 slip ratio Bottom Left) 0.75 slip ratio; Bottom Right) 0.95 slip ratio

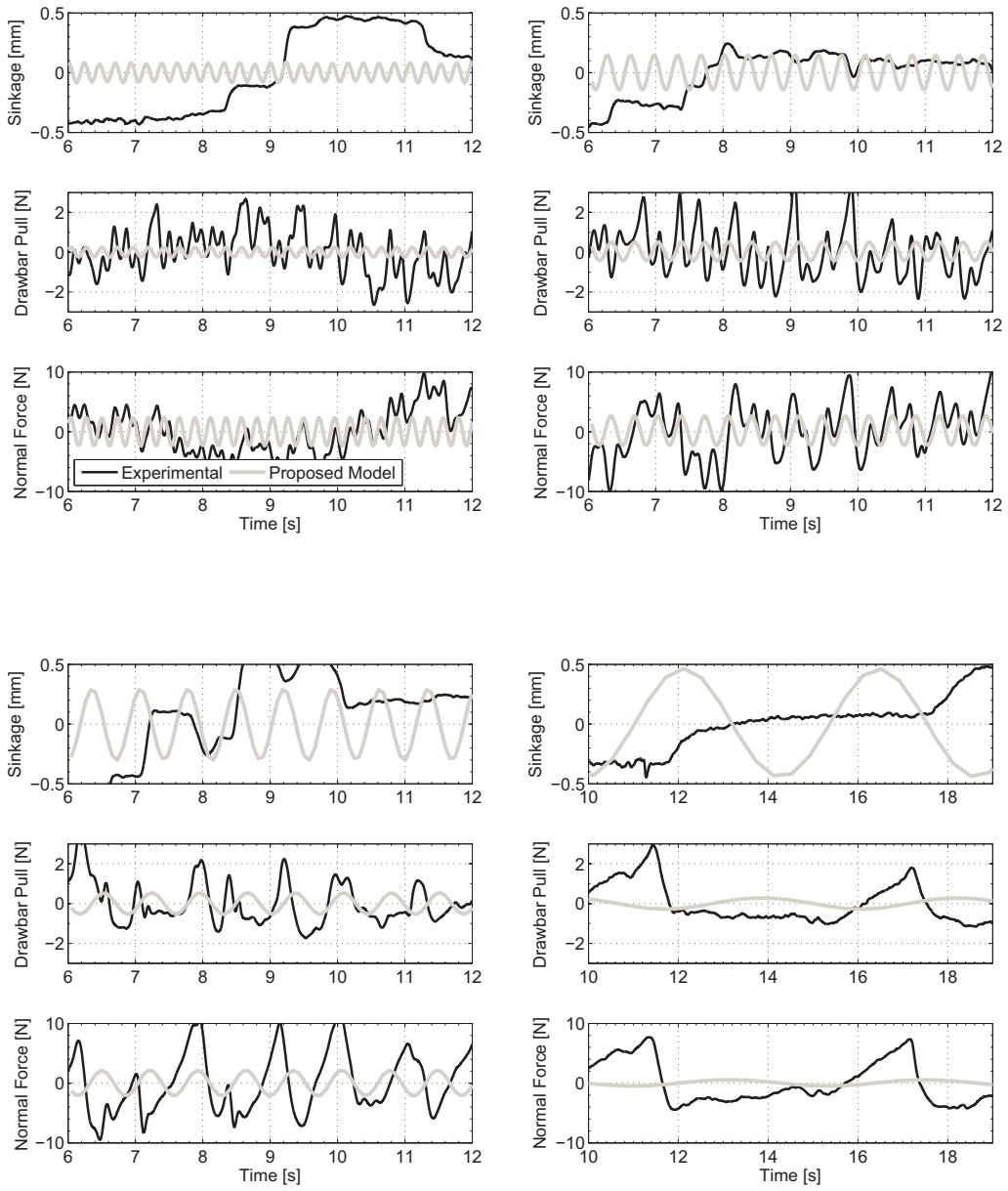

Figure 4.15: Mean adjusted simulation data of a smooth rigid wheel operating with a 64N normal load overlayed with experimental data. Top Left) 0.25 slip ratio; Top Right) 0.50 slip ratio Bottom Left) 0.75 slip ratio; Bottom Right) 0.95 slip ratio

Table 4.5: RMS Data for 64N Normal Load

Sinkage in millimeters

Slip Ratio	RMS Experimental	RMS Proposed Model	$\|\Delta\|$ Difference
.25	0.356	0.052	0.303
.50	0.184	0.106	0.078
.75	0.476	0.211	0.264
.95	0.437	0.311	0.126

Drawbar Pull in newtons

Slip Ratio	RMS Experimental	RMS Proposed Model	$\|\Delta\|$ Difference
.25	1.121	0.186	0.935
.50	1.245	0.337	0.908
.75	0.988	0.381	0.607
.95	1.135	0.196	0.939

Normal Force in newtons

Slip Ratio	RMS Experimental	RMS Proposed Model	$\|\Delta\|$ Difference
.25	3.784	1.761	2.023
.50	4.352	1.774	2.578
.75	5.248	1.513	3.734
.95	3.513	0.379	3.130

4.6 Summary

This chapter presents a new dynamic pressure-sinkage relationship for modeling the observed oscillations in drawbar pull and normal force for a smooth rigid wheel on dry sand. The proposed model was validated over a wide range of slip ratios and normal loads. The SWTB used for the validation is unique since the terrain is translated instead of the wheel assembly. Also, the SWTB is capable of very small normal loads because of the counterbalance system employed.

The experimental data showed a repeatable low frequency oscillation in the force data that could be correlated to visual ripples in the track left by the wheel. The proposed model accounts for this harmonic by adding an $A\sin(\omega t + \Phi)$ term into the traditional pressure-sinkage relationship. The final form of the new dynamic pressure-sinkage relationship is:

$$p(z) = \left(ck'_c + \gamma b k'_\phi\right)\left(\frac{z}{b}\right)^n + d\gamma l_c k'_a \sin(\omega(i)t + \Phi) \tag{4.23}$$

The experimental results agree reasonably well with the drawbar pull data for most slip ratio cases and normal loads tested. However, this model is for a *smooth wheel* which means that there is no *tread*, *grousers* or any other traction aids on the surface of the wheel. A smooth wheel model is more of a theoretical or academic case and thus one must extend the knowledge built in this chapter to a wheel with *grousers*.

CHAPTER 5

GROUSER WHEEL MODEL

Many planetary rovers have wheels with grousers, which are radial paddles on the wheels that are used to improve the tractive effort of a wheel [LGD08]. An example of a grouser wheel can be seen in Figure 5.1. The existing Bekker and Wong terramechanic models do not inherently capture the dynamic effects (oscillations) caused by grousers as seen in Figure 5.2. This figure shows experimental data of the wheel sinkage, drawbar pull and normal load plotted as a function of time, which has been superimposed over the simulation results of an existing terramechanic model for a rigid wheel. The experimental data was collected from the single-wheel testbed (SWTB) described in Chapter 2 for a 200mm diameter wheel having 16, 10mm long grousers, operating at 0.25 slip and a 66N normal load. In Figure 5.2 the wheel begins from rest and then starts its traverse through the loose sandy soil. One can clearly see the oscillations in the measurements caused by the wheel's grousers. As shown in Figure 5.2, the existing analytical terramechanic model was developed to predict the mean values for the sinkage, drawbar pull and normal load; however, the oscillations are not unaccounted for. A summary of the soil and wheel parameters used in Figure 5.2 and for the rest of this chapter can be found in Table 5.1.

This chapter builds on the dynamic smooth wheel terramechanic model of Chapter 4 to develop a new analytical model that captures the dynamic effects caused by the addition of grousers. The resulting proposed model is then validated by using experimental data collected from a SWTB.

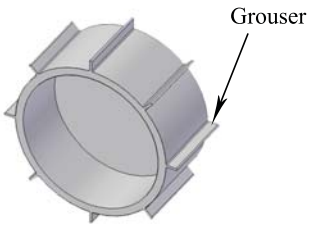

Figure 5.1: An example of a grouser wheel

Table 5.1: Summary of Parameters

Parameter	Value	Unit	Comments
k'_c	0	–	Dimensionless cohesive modulus
k'_ϕ	80	–	Dimensionless frictional modulus
K	0.036	m	Shear deformation modulus
n	1	–	Sinkage exponent
γ	13734	N/m^3	Soil weight density
$d\gamma$	$0.1 \times \gamma$	N/m^3	Change in soil weight density
r	0.1	m	Radius of wheel
b	0.075	m	Width of wheel
η	1.15	–	Rear of wheel sinkage relationship
ϕ	28	deg	Internal angle of friction
c	0	kPa	Soil cohesion
h_b	0.01	m	Grouser length
C_f	800	Ns/m	Viscous friction coefficient
k'_g	0.06	–	Dimensionless grouser amplitude coefficient
k'_a	0.03	–	Dimensionless density amplitude coefficient

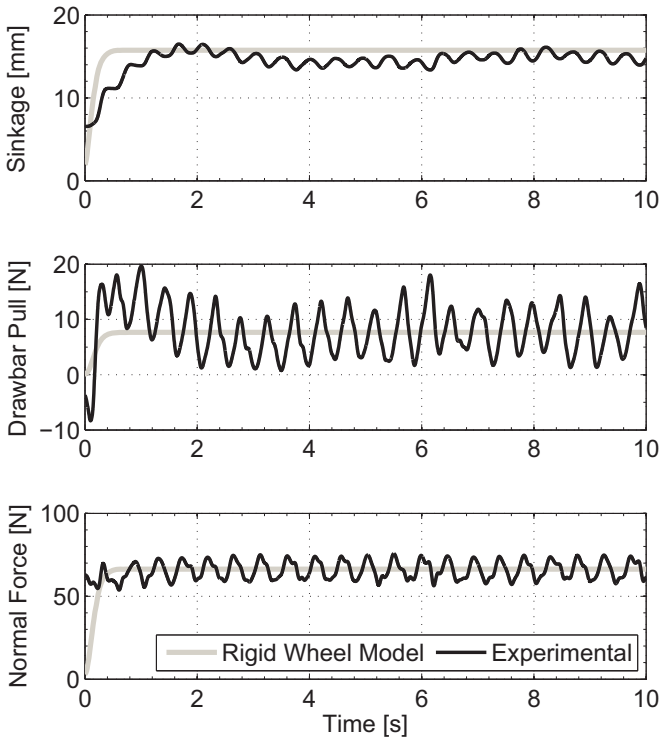

Figure 5.2: Experimental data of a rigid wheel with 16, 10mm long grousers, operating at 0.25 slip and a 66N normal load overlayed with a typical terramechanic model [IMNY07] for a rigid wheel

5.1 Proposed Dynamic Model

This researcher proposes that the oscillations seen in the sinkage, drawbar pull and normal load caused by the grousers can be accounted for by enhancing the dynamic pressure-sinkage relationship (Chapter 4) for a smooth wheel as follows:

$$p\left(z\right) = \left(ck'_c + \gamma bk'_\phi\right)\left(\frac{z}{b}\right)^n + A\sin(\omega t + \Phi) \tag{5.1}$$

where t is time and Φ is an optional phase shift that can be applied to the model to account for the initial orientation of the grousers. The A term is the amplitude of the oscillation and ω is the frequency at which they occur. Through the work done in Chapter 4 a solution was presented as $A = d\gamma l_c k'_a$ for a smooth wheel; however, a new solution must be formulated for a wheel with grousers.

Figure 5.3 shows the normal stress distribution that has been proposed by Karafiath and Nowatzki [KN78] when grousers or lugs are present. A traditional terramechanic model will attempt to estimate the average normal stress value as shown in Figure 5.3. However, when the grousers are moving through the terrain the location of the maximum normal stress and the value of the maximum and mean normal stress will fluctuate as a function of time. The dynamic pressure-sinkage model should estimate these fluctuations and variations in the pressure-sinkage relationship that are caused by the presence of grousers. The following sections present solutions of how to determine the two new terms ω and A in the grouser specific model.

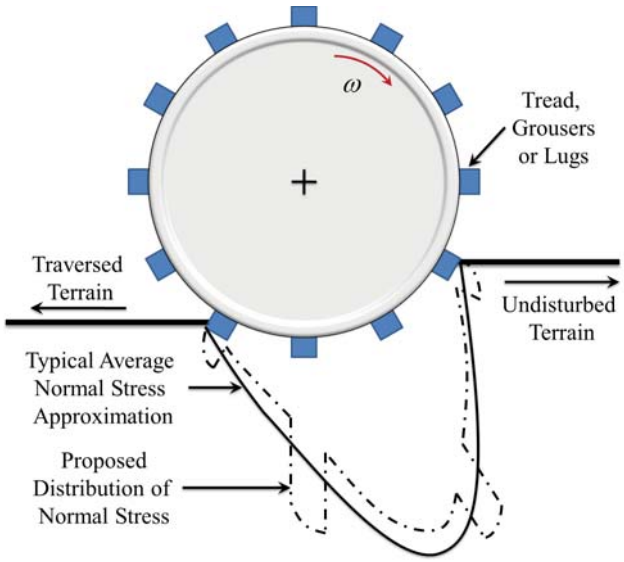

Figure 5.3: A wheel with grousers and the proposed stress distribution [KN78]

5.1.1 *Frequency ω*

It is reasonable to assume that the frequency ω is related to the spacing of the grouser blades and the speed of rotation. As each blade comes into contact with the soil there will be an increase in the stresses. Thus, the frequency term ω in Equation (5.1) becomes:

$$\omega = \frac{\omega_w}{n_g} \tag{5.2}$$

where n_g is the number of grousers and ω_w is the angular velocity of the wheel in radians per second.

5.1.2 Amplitude A

It is proposed that there are two main factors contributing to the amplitude term A such that:

$$A = A_\sigma + A_\gamma \tag{5.3}$$

where the first factor A_σ is related to the active and passive stresses which the terrain experiences due to the presence of a grouser. The second factor A_γ is related to the change in the local soil density around the wheel and grouser caused by the soil deformation occurring as the wheel traverses over the terrain and builds from the work done in Chapter 4.

5.1.2.1 Active and Passive Stresses; A_σ

Wong [Won10] outlines how active and passive stresses can be applied to a grouser blade to calculate the maximum tractive effort it can deliver. It is proposed that the amplitude of the oscillations in the pressure sinkage relationship can be related to these active and passive stresses. Both stresses act in the same direction as the shear stress and, therefore, contribute additional components to the vertical and horizontal forces. The passive stresses act on the face of the grouser coming into contact with the terrain (the front face of the grouser). Active stresses may be acting as the soil moves away from the grouser blade and, if present, would act on the rearward side of the grouser (the back face of the grouser). The two stresses act in opposite directions, hence their net sum adds to the forces acting on the wheel if both stresses are present. Figure 5.4 shows the active and passive failure stress zones on the front face and rear face of a grouser moving though the terrain. The theory assumes that there is no stress acting perpendicular to the active or passive stresses. For the grouser blade the theory would then assume that there is no stress acting in the radial direction along the face of the grouser blade. This assumption, however, is inaccurate for the sandy-soil conditions used in the current study. Due to the flow of the sand grains there will be some degree of stress acting on the faces of the grouser in the radial direction which is perpendicular to the active and passive stress directions. Moreover, the

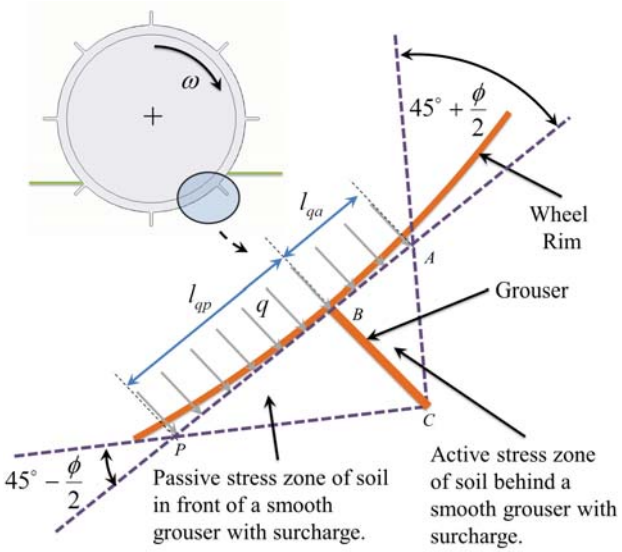

Figure 5.4: Active and Passive stress zones on a wheel when grousers are present

stress field will not be perfectly triangular as shown in Figure 5.4 which has been idealized by the active and passive theory. Wong [Won89] has shown the complex flow fields of sand grains around a grouser blade and, in practice, the active and passive stresses from the grousers can affect the normal and shear stress simultaneously. This research will use the theoretical calculations of the active and passive stress to estimate the variations in the normal stress field, and the modified Mohr-Coulomb relationship will be used to determine the corresponding shear stress. To examine the theoretical contribution of the active and passive stresses, the two stresses were computed and added to the shear stress (Equation 3.18) at the appropriate angular position of the wheel grouser.

In this theoretical case-study the wheel is 10 cm in diameter with 3 grousers in contact with the terrain. The grousers are 15mm long by 3mm thick and the wheel is operating at a slip ratio of 0.4 with a sinkage of 5cm while η is 0.5. The results of this case-study are shown in Figure 5.5 which plots the calculated normal and shear stress as a function of angular position along the wheel for an instant in time. One can see the additional shear stress components from the active and passive stresses on the faces of the grousers. Figure 5.5 shows that the passive stresses are significantly larger than the active stresses and, therefore, the passive

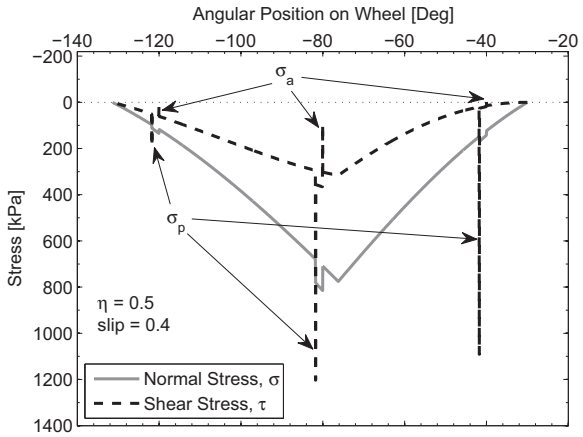

Figure 5.5: Normal and shear stress along the face of the wheel with active and passive stress added to the shear stress for an instant in time

stresses will dominate the net effect of the additional shear stress. Moreover, for active stresses to be acting on the rear of the grouser face, the rear blade face must be in contact with the soil. In practice this may not always be true depending on the wheel speed and terrain conditions [Won89]. As a result of this analysis, for the sandy soil, used in this research it was found that the passive stress from the grousers in contact with the terrain will dominate the active and passive stress contributions to the amplitude term A in Equation (5.1). Passive stresses are computed by [Won10]:

$$\sigma_p = \gamma z N_\phi + q N_\phi + 2c\sqrt{N_\phi} \tag{5.4}$$

where the flow value N_ϕ is given by:

$$N_\phi = \tan^2\left(45^\circ + \frac{\phi}{2}\right) \tag{5.5}$$

In Equation (5.4), the parameter q is known as surcharge. The surcharge is the additional pressure applied to the surface of the terrain from external sources. For the wheel-soil interaction this surcharge would come from the normal stress of the smooth wheel sections in between the grousers which is computed by using the pressure-sinkage relationship. The length over which this surcharge acts is

calculated by [Won10]:

$$l_{qp} = \frac{h_b}{\tan^2\left(45^\circ - \frac{\phi}{2}\right)} \tag{5.6}$$

Equation (5.4) assumes that the surcharge is uniform across l_{qp}; however, the pressure sinkage relationship (Equation (5.1)) states that every depth of the wheel-soil interface will experience a different pressure and, as a result, the surcharge for the wheel-soil interaction is not uniform. Equation (5.4) also assumes that the surcharge is evenly distributed along the length l_{qp}; however, due to the curvature of the wheel, this assumption is also not valid for the wheel-soil interaction. To overcome these issues, it is proposed that the mean pressure from the pressure-sinkage relationship acting along the wheel-soil interface bounded by l_{qp} is used to approximate the surcharge. The authors also propose that the mean of the maximum passive stresses from the grousers in contact with the terrain $\bar{\sigma_p}$ are proportional to the amplitude term A in Equation (5.3). Thus,

$$A_\sigma = k'_g \bar{\sigma_p} \tag{5.7}$$

where k'_g is an empirical dimensionless coefficient. Equation (5.7) can then be used to estimate the variations in the normal stress amplitude caused by the passive stress of the grousers traveling though the terrain. Having presented a solution for A_σ in Equation (5.3), a solution for A_γ is now needed to estimate the changes in the normal stress amplitude caused by variations in the local terrain density.

5.1.2.2 Change in Local Density; A_γ

As a grouser wheel travels through loose sandy soil there are varying degrees of deformation occurring along the wheel-soil interface and within the soil structure itself. There is more deformation near the interface and the grousers, and less deformation as one moves farther from the interfacing surfaces. It is hypothesize that this deformation allows some of the voids in the random sand structure to be filled by the moving sand grains. Decreasing the the local void ratio will increase the density of the sand around the wheel. This change in density effectively increases the strength of the sand and causes an increase in the normal and shear

stress which the wheel can exert on the terrain. Thus, A_γ will have the same form which was presented in Chapter 4:

$$A_\gamma = k'_a l_c d\gamma \tag{5.8}$$

where, k'_a is an empirical dimensionless coefficient and the dimensional analysis is satisfied.

5.2 Dynamic-Pressure Sinkage Model for Grouser Wheels

Substituting the previous solutions for frequency ω and amplitude A into Equation (5.1) yields the final proposed dynamic pressure-sinkage relationship for the terramechanic model:

$$p(z) = \left(ck'_c + \gamma b k'_\phi\right)\left(\frac{z}{b}\right)^n + (k'_g\bar{\sigma_p} + k'_a l_c d\gamma)\sin\left(\frac{\omega_w}{n_g}t + \Phi\right) \tag{5.9}$$

The proposed model was validated with the SWTB and the numerical simulations were carried out in the MATLAB/Simulink environment by taking advantage of the Simscape blockset. The test equipment was described in Chapter 2 and the numerical solution is similar to what was described in Chapter 3 with the modified algorithm found in Appendix B. The next section will present and discuss a selection of test cases for the experiments carried out with the SWTB and the corresponding simulations that were performed.

5.3 Experimental Results

When examining the experimental data from the SWTB, the frequency relationship relating the number of grousers to the angular velocity of the wheel (Equation 5.2) was confirmed by performing a fast fourier transform on the measured data. Figure 5.6 shows the cumulative results of a single-sided frequency spectrum for the drawbar pull of a wheel with 16, 10mm grousers operating at various conditions. The dominant and consistent peak at 2.1Hz is the frequency of interest and matches the predicted frequency from Equation 5.2. To confirm the

validity of Equation 5.2 a variety of operating conditions were examined. Using (A) in Figure 5.6 as a baseline, the normal load was increased in (B) and (C) with no appreciable change in the frequency or the expected result. Comparing (A) with (D), the slip ratio was increased and again there was no appreciable change in the frequency results. Comparing (A) to (E), the grouser length was increased from 10 to 23mm and, as predicted, there was no change in the frequency. Finally, the number of grousers were doubled from (A) to (F) and, as expected, one can see that the frequency doubles. This testing confirms that Equation 5.2 correctly predicts the frequency of the oscillations.

Figure 5.7 shows a digital image of the disturbed terrain on the SWTB after a grouser wheel has passed through, along with a schematic of the point of view. When grousers are present there is a repeatable ridge pattern which is left in the sand after the wheel has traversed the terrain. These ridges correspond to the grousers leaving the wheel-soil interface. It is interesting to note that the ridges occur at the same frequency as the oscillations observed in the sinkage, normal load and drawbar pull (2.1Hz). These types of ridges or waves have been observed by grouser wheels on Mars [ABIB+10] and in other work here on Earth performed by Ding et al. [DGD+11]. Models that can capture the observed oscillations are needed so that mission specialists of future endeavors have access to higher fidelity models to help determine the mobility capabilities of the rover.

Figure 5.8 shows the peak-to-valley amplitude of the drawbar pull as a function of normal load and slip ratio. The surfaces shown in the figure are interpolated for display purposes. One can see that as the normal load increases the magnitude of the drawbar pull oscillations increases. To capture this amplitude increase as a function of normal load, parameter A in Equation (5.1) or (5.3) will need to increase as a function of the normal load. To better understand the data at slip ratios higher than 0.5 one must examine the contact length of the wheel-soil interface.

Figure 5.9 plots experimental results of the contact length as a function of normal load and slip ratio where the surfaces shown have been interpolated for display purposes. One will notice, particularly for the lowest normal load of 15N, that there is a linear trend of increasing contact length until a slip ratio of 0.5, at

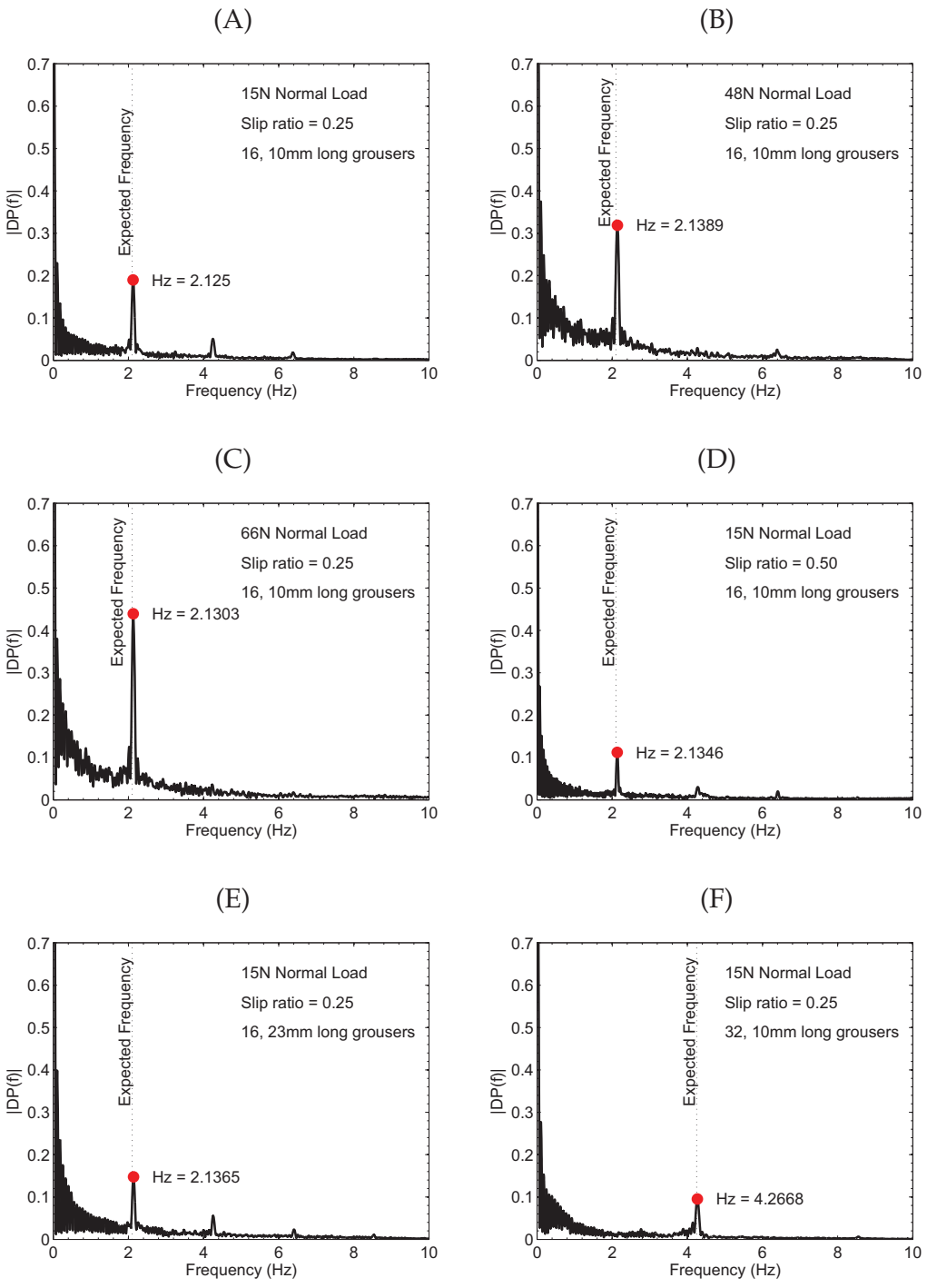

Figure 5.6: Fast Fourier Transforms of a grouser wheel

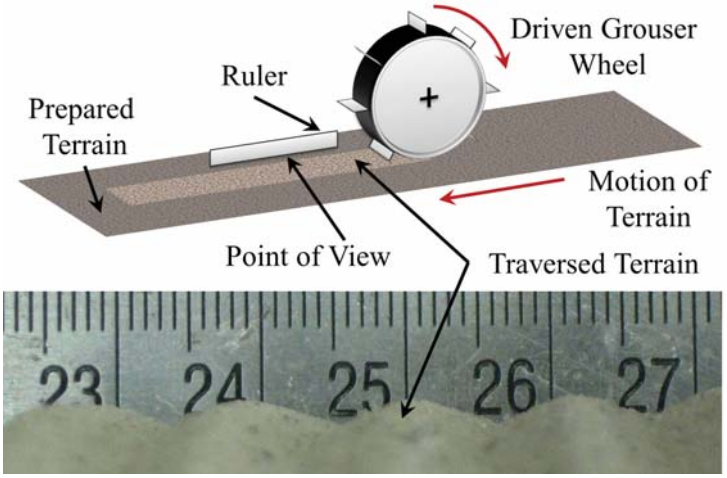

Figure 5.7: Digital image of the disturbed terrain on the SWTB and a schematic of the point of view. The wheel has 16, 10mm long grousers, 15N normal load and a slip ratio of 0.50

which point the contact length begins to rapidly increase. For the 48N and 66N normal loads, tests were not carried out past a slip ratio of 0.75 and 0.5, respectfully, because the rate of excavation was too great and the possibility of damaging the SWTB was deemed an unnecessary risk for the purpose of this work. However, the linear trend before a slip ratio of 0.5 is still present in all cases and the increased excavation occurs after a slip ratio of 0.5. If one performs a three dimensional linear surface fit for contact length as a function of normal load and slip ratio on all data below a slip ratio of 0.5, the result would yield a fit with an R^2 value of 0.98. If one repeats the linear fitting process but includes only the data above 0.5 the fit yields an R^2 value of 0.93. For the test sand used in this study it is found that there is a distinct slip ratio, 0.5, for the three normal loads tested after which the excavation rate increases.

To obtain a reasonable fit that includes all of the data, the order of the polynomial fit must be increased. However, if one uses a higher order fit, the higher order terms should have some physical meaning or theory to justify them. At these high excavation rates other phenomena may be present and influencing the wheel-soil interaction such as fluidization which was suggested by Ishigami et al. [IMNY07]. Fluidization of the sand structure below the wheel caused by the

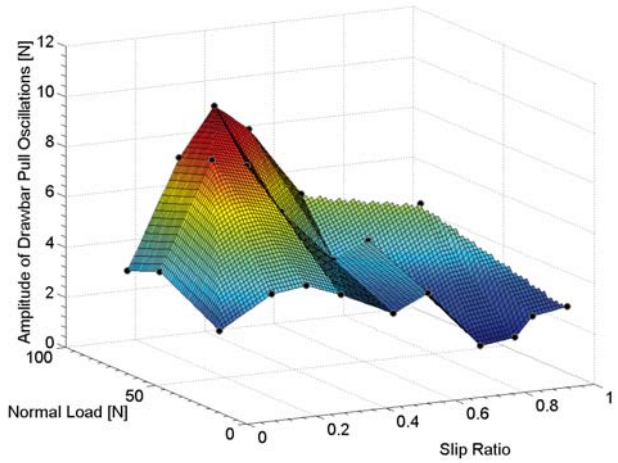

Figure 5.8: Graphical representation of the peak-to-valley amplitude of the drawbar pull as a function of normal load and slip ratio

presence of grousers could explain the rapid increase in the excavation at higher slip ratios. When a granular materials is subject to small displacements, either through vibration or other means, the macroscopic property of the granular system can change from a solid to a fluid [JN92]. Prior to fluidization, the material would be able to resist shear and the wheel would gain traction by resisting the shear applied by a grouser. If the sand becomes fluidized, the terrain will act more as a fluid and is then unable to fully resist the applied shear stress from a grouser. With the material's inability to resist shear stress, the grousers on the wheel will tend to excavate the material and the tractive effort of the wheel may be compromised. Further research needs to be conducted to better predict and account for the excavation increase observed at higher slip ratios. Despite the possibility of unaccounted phenomena and the complex relationship between slip ratio, normal load and the amplitude of the oscillations in the measured data, values for the the new dimensionless factors k'_a and k'_g for the proposed dynamic pressure sinkage relationship described by Equation (5.9) were determined. The model was then manually fit to the data collected from the experimental setup to

develop a semi-empirical model for researchers to advance and mission specialists to use.

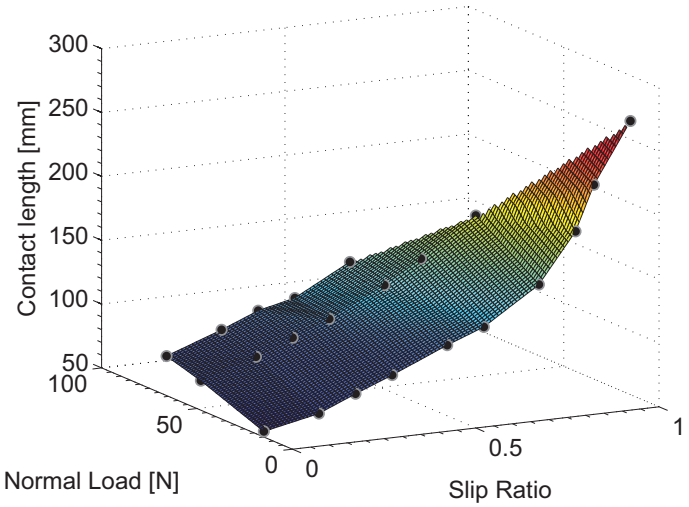

Figure 5.9: Graphical representation of the contact length as a function of normal load and slip ratio

5.4 Results

Figure 5.10 compares experimental and simulation results using the new dynamic model for sinkage, drawbar pull and normal load plotted as a function of time. The simulation is of a wheel with 16 grousers, 10mm long, operating at 0.25 slip and a 66N normal load (which are the same operating conditions as seen in Figure 5.2). In this study k'_g and k'_a were tuned to be 0.06 and 0.03, respectfully. The simulation and experimental results show that the model is within 8.2% of the experimental mean values for the wheel sinkage, drawbar pull and normal load. When compared to experimental data the proposed model is able to capture the peak-to-valley sinkage oscillation to within 0.25mm, the drawbar pull peak-to-valley oscillation to under 5.6N and the normal load peak-to-valley oscillation to under 8N. One can see from Figure 5.10 that the results for the sinkage and normal load results are very good while the drawbar pull oscillations are under

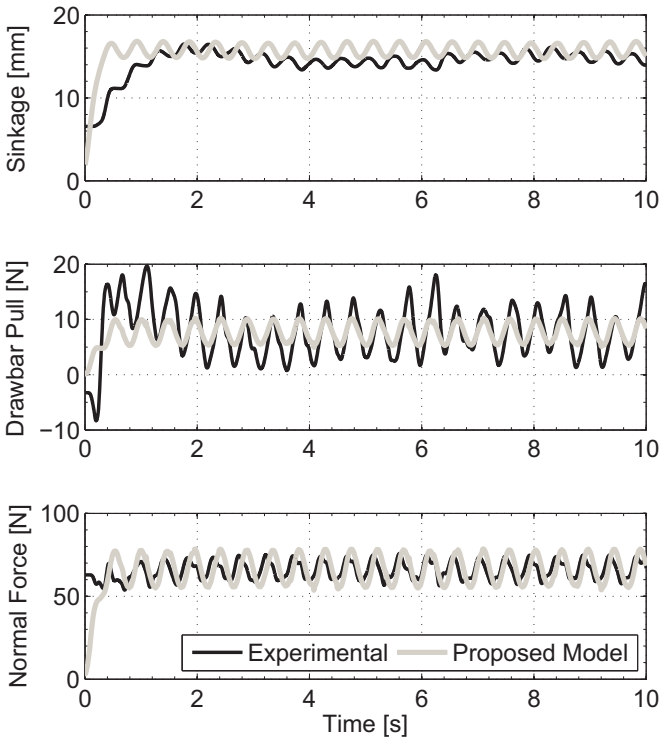

Figure 5.10: Simulation of a rigid wheel with 16, 10mm long grousers, operating at 0.25 slip and a 66N normal load overlayed with experimental data

predicted for this testing condition.

For the remaining test cases the data will be presented as mean-adjusted plots for a limited time span during a period of steady-state operation to focus on the contribution of this work — the oscillations in the sinkage, drawbar pull and normal load. Furthermore, to test the model's predictive capabilities, the model parameters tuned for the 0.25 slip and 66N normal load conditions shown in Figure 5.10 were held constant for the remaining test cases.

Figure 5.11 shows the mean adjusted plots for sinkage, drawbar pull and normal load plotted as a function of time for two different slip ratios (0.35 and 0.5) and a normal load of 66N. For these new test cases, k'_g and k'_a remained at 0.06 and 0.03, respectfully (the same values used for the 0.25 slip ratio and 66N normal load case). One can see that the amplitude of the oscillations for these new

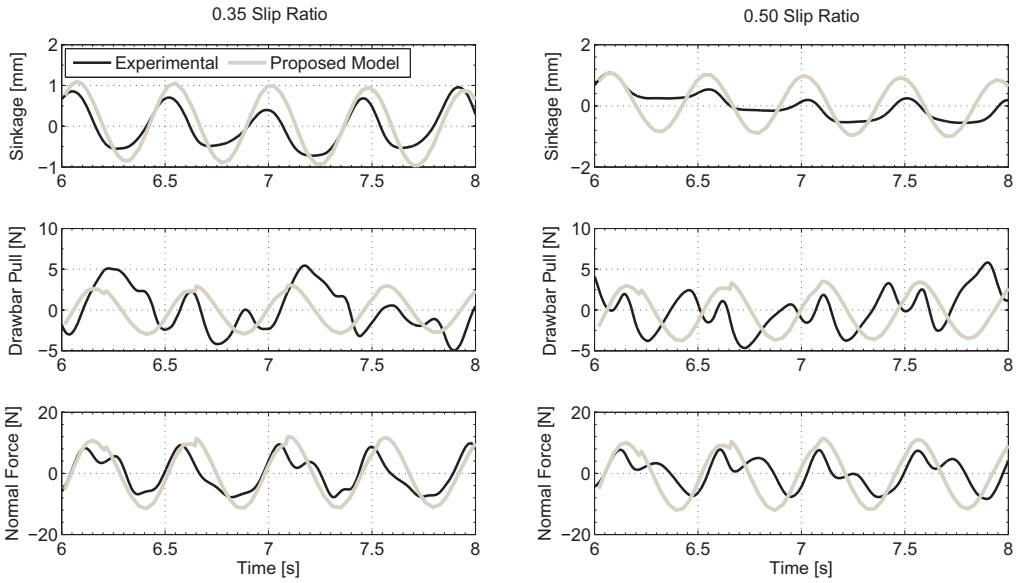

Figure 5.11: Mean adjusted simulation data of a rigid wheel with 16, 10mm long grousers, operating with a 66N normal load overlayed with experimental data. Left) 0.35 slip ratio Right) 0.50 slip ratio

slip ratios are effectively captured by the proposed model.

Figure 5.11 also shows small discontinuities in the simulated force data. These discontinuities are caused because the model does not account for the transition of the grouser coming into contact with the terrain, or the gradual departure of the grouser leaving the terrain. Although the exact shape of the oscillations are not captured, perhaps due to phenomena such as fluidization, the model is able to approximate the dominant dynamic trends in the measured data.

Table 5.2 presents the RMS experimental and simulated data for the three cases mentioned above for the time spans shown in Figure 5.11. The table also presents the difference or delta between these two RMS calculations. The RMS data confirms that the dynamic model is able to reasonably capture the dynamic effects.

Figure 5.12 shows the mean adjusted plots for sinkage, drawbar pull and normal load as a function of time for slip ratios 0.25, 0.35, 0.50 and 0.75 when the normal load was changed to 48N. For all of these cases k'_g and k'_a were again unchanged from the 66N normal load case. Table 5.3 presents the RMS experimental and simulated data for the 48N normal cases. The RMS calculations were taken

Table 5.2: RMS Data for 66N Normal Load

Sinkage in millimeters

Slip Ratio	RMS Experimental	RMS Proposed Model	$\|\Delta\|$ Difference
.25[1]	0.553	0.657	0.104
.35	0.514	0.651	0.137
.50	0.315	0.651	0.336

Drawbar Pull in newtons

Slip Ratio	RMS Experimental	RMS Proposed Model	$\|\Delta\|$ Difference
.25[1]	3.91	1.688	0.104
.35	2.174	2.041	0.133
.50	2.439	2.468	0.029

Normal Force in newtons

Slip Ratio	RMS Experimental	RMS Proposed Model	$\|\Delta\|$ Difference
.25[1]	5.185	8.063	2.898
.35	5.541	7.996	2.455
.50	4.524	7.972	3.447

[1] Denotes the slip ratio which the model was tuned with

for the time spans shown in Figure 5.12. One can see that the RMS difference between the experimental and the proposed model predictions is very good—especially for the sinkage. However, when one examines the time history results (Figure 5.12) one will notice that the model is not capturing the oscillations quite as well as one might imagine when just the RMS data is examined. The RMS calculation is independent of phase and, therefore, any experimental data drift will affect the RMS averaging which can cause misinterpretation of the data. As a result, it is important to note that one should not solely rely on the RMS data as a metric to analyse this dynamic model and the corresponding experimental results.

Figure 5.13 shows the mean adjusted plots for sinkage, drawbar pull and normal load plotted as a function of time for three slip ratios, 0.25, 0.35, 0.5 and 0.75 when the normal load is reduced to 15N. Again, for these cases k'_g and k'_a remained unchanged from the tuning case (66N normal load at 0.25 slip, for this study). One can see that the model is not able to estimate the oscillations as well as before for all of the test cases, particularly in the drawbar pull measurements. This result is expected since the 15N normal load test case is significantly different than the 66N normal load test case for which the model was tuned. Table 5.4 presents the RMS experimental and simulated data for the 15N normal cases. The RMS calculations were taken for the time spans shown in Figure 5.13. The RMS data does a reasonably good job of indicating the model's accuracy for most of the test cases at this normal load when viewed in conjunction with the time history data (Figure 5.13).

It is important to note that, although the dimensionless parameters k'_g and k'_a remained unchanged for all of these test cases, the amplitude term A will vary as a function of time and the operating conditions. In the amplitude term A (Equation 5.3), the first term A_σ is a function of $\bar{\sigma_p}$ which will vary as a function of the normal load since $\bar{\sigma_p}$ is the mean of the maximum passive stresses of the grousers in contact with the terrain. The passive stresses are calculated from the applied normal stresses which will vary as a function of the normal load. The mean of the maximum passive stresses $\bar{\sigma_p}$ will also vary as a function of time since the location of the grousers are changing as a function of time and the

passive stresses are a function of the surcharge q. The time dependency comes from the surcharge which is the normal stress acting just ahead of the grousers as well as from the normal stress which is a function of the angular position. These relationships imply that the passive stresses ($\bar{\sigma_p}$) will vary as a function of time. Moreover, the sinkage is proportional to the applied load and slip ratio which, in turn, will cause l_c to be related to the operating conditions. Thus, the A_γ factor of the amplitude term A (which uses l_c) will vary as a function of the operating conditions. As a result of the formulation of the proposed model, the amplitude term A (Equation 5.3) is a function of time and the operating state during the simulations and it, therefore, needs to be recalculated at each time-step during the simulation.

To help graphically explain the discussion above, Figure 5.14 shows the calculated values of parameter A as a function of time for a wheel with 16, 10mm long grousers for three normal loads, 15, 48 and 66N. For these three cases the dimensionless parameters k'_g and k'_a remained constant at 0.03 and 0.06, respectfully, but one will notice that the mean magnitude of A did increase as a function of the normal load. The increase of the mean value is attributed to the fact that the passive stresses and the contact length will vary as a function of the normal load. One can also see how A varies as a function of time. The parameter dependency, mentioned above, allows for the model to automatically adjust for different operating conditions. Again one will notice discontinuities of the A term in Figure 5.14 which occur because the model does not account for the transition of the grouser entering or departing contact with the terrain.

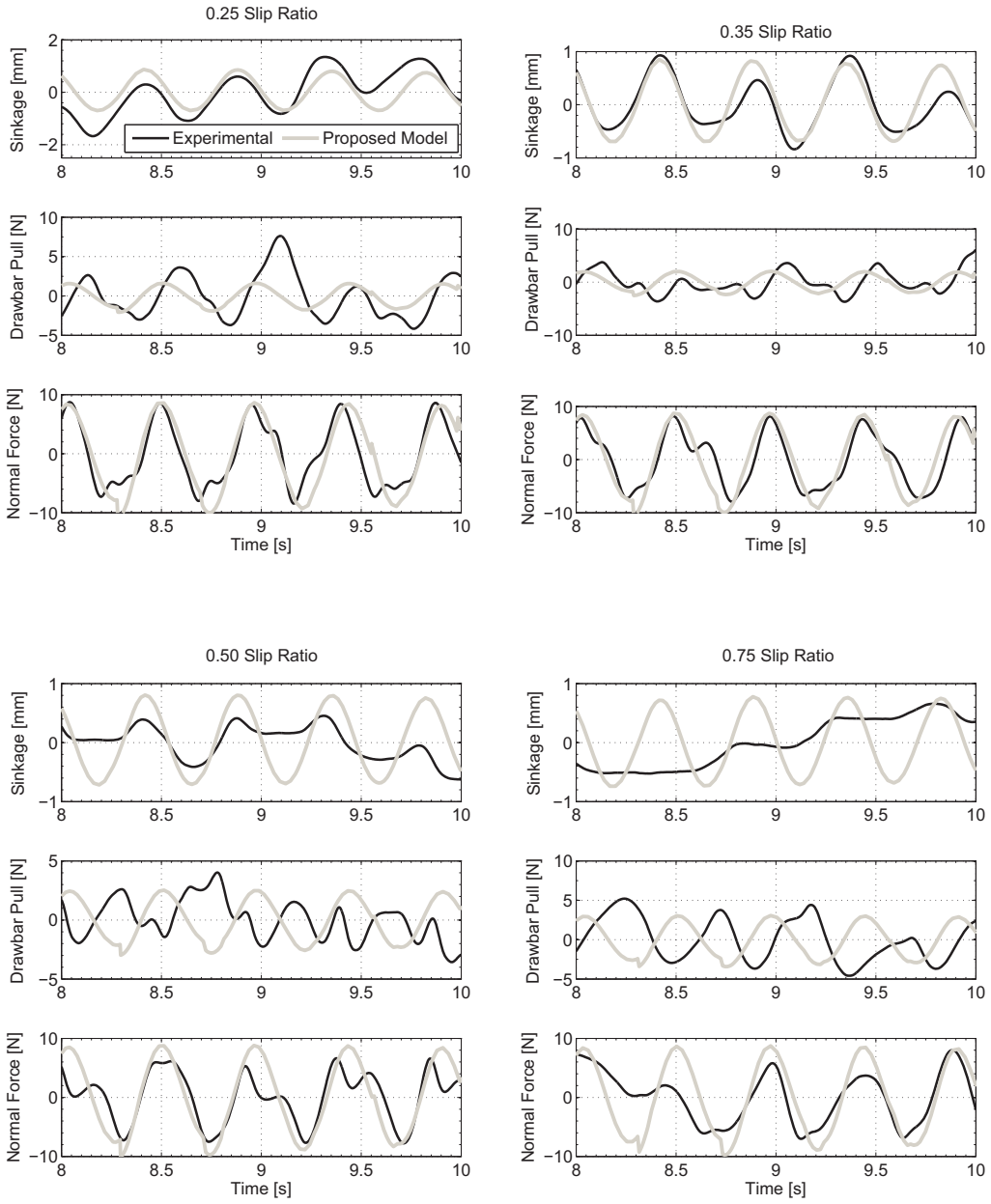

Figure 5.12: Mean adjusted simulation data of a rigid wheel with 16, 10mm long grousers, operating with a 48N normal load overlayed with experimental data. Top Left) 0.25 slip ratio; Top Right) 0.35 slip ratio Bottom Left) 0.50 slip ratio; Bottom Right) 0.75 slip ratio

Table 5.3: RMS Data for 48N Normal Load

Sinkage in millimeters

Slip Ratio	RMS Experimental	RMS Proposed Model	$\|\Delta\|$ Difference
.25	0.632	0.506	0.126
.35	0.428	0.503	0.075
.50	0.220	0.500	0.279
.75	0.203	0.489	0.286

Drawbar Pull in newtons

Slip Ratio	RMS Experimental	RMS Proposed Model	$\|\Delta\|$ Difference
.25	2.344	1.228	1.117
.35	2.130	1.497	0.633
.50	1.578	1.838	0.260
.75	2.583	2.222	0.361

Normal Force in newtons

Slip Ratio	RMS Experimental	RMS Proposed Model	$\|\Delta\|$ Difference
.25	5.353	6.355	1.002
.35	4.746	6.310	1.564
.50	4.326	6.336	2.010
.75	4.645	6.232	1.587

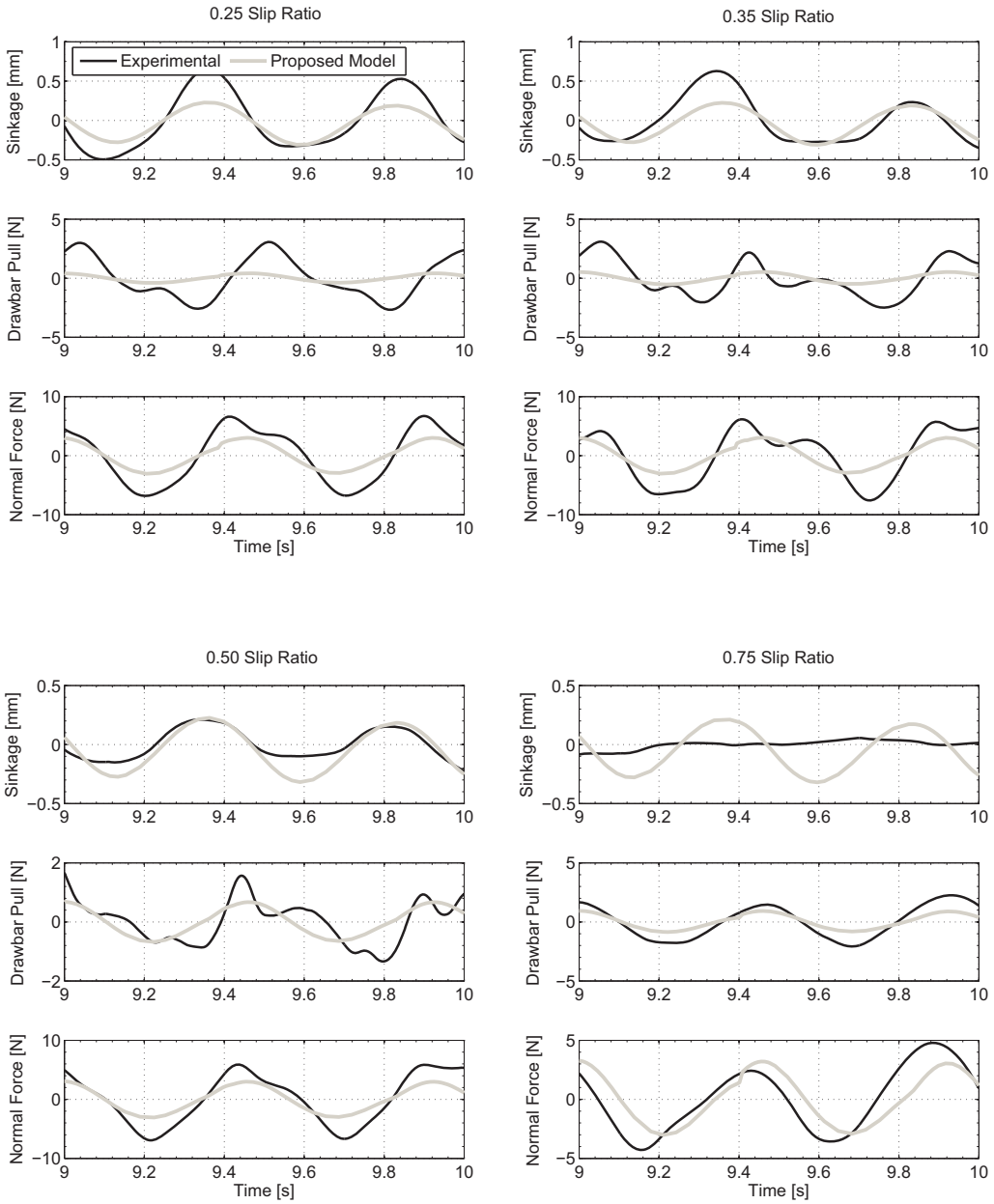

Figure 5.13: Mean adjusted simulation data of a rigid wheel with 16, 10mm long grousers, operating with a 15N normal load overlayed with experimental data. Top Left) 0.25 slip ratio; Top Right) 0.35 slip ratio Bottom Left) 0.50 slip ratio; Bottom Right) 0.75 slip ratio

Table 5.4: RMS Data for 15N Normal Load

Sinkage in millimeters

Slip Ratio	RMS Experimental	RMS Proposed Model	$\|\Delta\|$ Difference
.25	0.410	0.176	0.234
.35	0.341	0.173	0.168
.50	0.165	0.174	0.010
.75	0.065	0.172	0.108

Drawbar Pull in newtons

Slip Ratio	RMS Experimental	RMS Proposed Model	$\|\Delta\|$ Difference
.25	1.858	0.306	1.554
.35	1.126	.391	0.735
.50	1.399	0.492	0.906
.75	1.260	0.637	0.622

Normal Force in newtons

Slip Ratio	RMS Experimental	RMS Proposed Model	$\|\Delta\|$ Difference
.25	4.216	2.277	1.939
.35	4.214	2.269	1.945
.50	4.337	2.224	2.113
.75	2.531	2.220	0.311

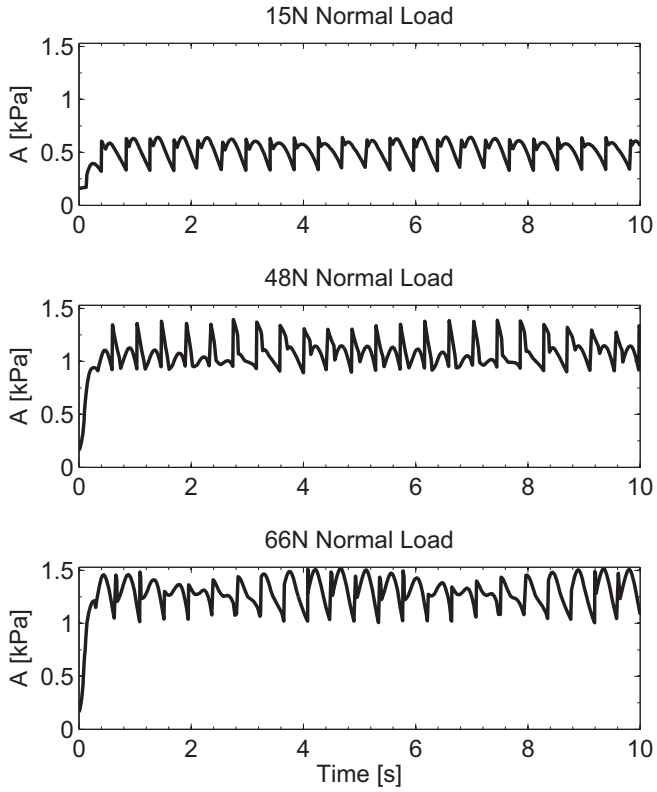

Figure 5.14: A plotted as a function of time for a wheel with 16, 10mm long grousers, operating with three different normal loads

5.5 Summary

This chapter enhances the previous chapter's dynamic pressure sinkage model to explicitly account for grousers on a wheel. The new form of the dynamic pressure-sinkage relationship is:

$$p(z) = \left(ck'_c + \gamma b k'_\phi\right)\left(\frac{z}{b}\right)^n + \left(k'_g \bar{\sigma}_p + k'_a l_c d\gamma\right)\sin\left(\frac{\omega_w}{n_g}t + \Phi\right) \tag{5.10}$$

It is apparent from this study that the model improves traditional terramechanic models when the dynamic effects of grousers are of importance. The additional terms in the model are based on existing soil mechanic theories that vary as a function of soil properties, slip conditions, and vehicle loading. To tune the proposed model only two new dimensionless empirical coefficients k'_g and k'_a need to be adjusted as they do not affect the mean values of the sinkage, drawbar pull or normal load.

CHAPTER 6

CASE STUDIES AND MODEL APPLICATIONS

This chapter further investigates the dynamic pressure-sinkage relationship that was developed in Chapter 4 and 5 to better capture periodic variations observed in the sinkage, drawbar pull and normal force measurements as a rigid wheel interacts with loose sandy soil. Several case studies are presented to help determine the applicability of this dynamic pressure-sinkage relationship. The first case study examines how smooth wheels mounted on a 4-wheeled micro rover testbed interact with sandy soil at different slip ratios as the rover navigates an incline. The second case study investigates the influence of grouser height on the wheel-soil interaction at different slip ratios using measurements from a single wheel testbed. The third and fourth case studies also use a single wheel testbed and focuses on how wheels with different length and number of grousers interact with sandy soil at different slip ratios.

6.1 Case Study #1: Smooth-Wheel Rover Tests

The small four-wheel micro rover previously described in Chapter 2 was used again for this case study. The micro rover has 100mm diameter smooth wheels and was tested in the same sandy soil used throughout this research. The rear wheels were driven through a 505.9:1 geartrain while the front wheels were free

to rotate. Given the dynamic pressure-sinkage relationship presented in Chapter 4, it is hypothesized that the rear wheels, when slipping, should produce repeatable ridges, and that the front wheel would leave a smooth track since their drawbar pull would be negative. These predictions come from the results of the smooth wheel testing performed on the SWTB and discussed in Chapter 2. A tachometer was used to determine the angular velocity of the wheels and a potentiometer was used to record the linear translation of the 1.6kg vehicle. The rear wheels rotated at an average speed of 9.5rpm with a standard deviation of 0.21.

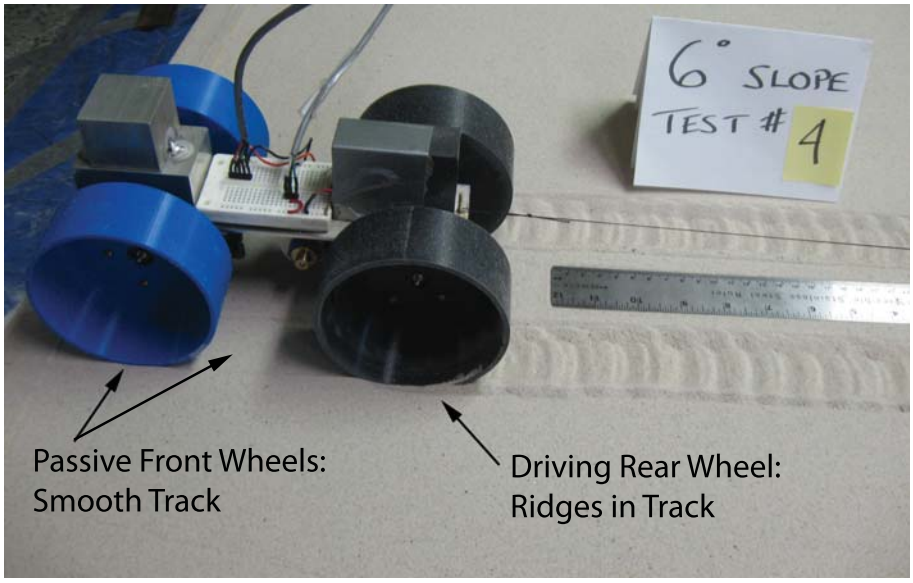

Figure 6.1: Micro rover at the end of a 6° slope climb

To achieve a repeatable and consistent slipping condition, hill climbing tests were carried out at 3.5°, 5° and 6° (maximum inclination which the rover could climb) which corresponded to rear-wheel slip ratios of 0.8, 0.95 and 0.96, respectively. Incline angles between 0° and 3.5° did not produce consistent or repeatable slip conditions. The reason for the irregular results at low inclines is likely from the initial conditions of the test sand where, before each test, the sand was manually mixed and leveled with a scraper tool. It is likely that the local density was not perfectly uniform after this manual preparation process and, therefore,

when the micro rover traversed the terrain, any small variations in the terrain influenced the mobility of the vehicle. Once the slip ratio increased to 0.8, however, the micro rover's rear wheels produced consistent and repeatable ridges in the sand as predicted.

The results of these tests can be seen in Figure 6.1 which shows the micro rover and its tracks with the ridges at a slip ratio of 0.96. Also, as predicted and shown in Figure 6.1, the un-powered front wheel produced a smooth flat track. Figure 6.2 shows a selection of the tracks from the rear wheels for the three inclines (Slip ratios) tested and, in this figure, heavy lines have been digitally superimposed to help the reader identify the ridges. When a linear least squares curve fit was performed on the three slip ratios tested, the data fell on a straight line with a negative slope as shown in Figure 6.3. This linear trend from the micro rover case study confirms earlier results found in Figure 4.9 of Chapter 4 which showed that there is a linear relationship between the frequency of the oscillations and the slip ratio when a smooth wheel was tested on a single-wheel testbed. The results of this case study also confirm that the proposed dynamic pressure-sinkage model should only be used when positive drawbar pull is established at a sustained slipping state.

The micro rover was tested with smooth wheels; however, most wheels have grousers to aid their tractive effort. The next cases studies will examine how well the dynamic model works when grouser designs are altered.

6.2 Case Study #2: Dynamic Effect of Grousers

A series of experiments were carried out on a single-wheel testbed using a wheel with grousers to build upon the previous work of Chapter 5 which presented a dynamic pressure sinkage model specifically for grouser wheels.

A wheel with 16, 23mm long grousers operating at a slip ratio of 0.50 and a normal load of 15N was used as a tuning case for the model. This operating condition is the only tuning case used for the remainder of this chapter. The non-dimensional coefficient k_c' was set to zero as suggested by Wong [Won01, Won10]. The remaining parameters were manually tuned and their values can be found in

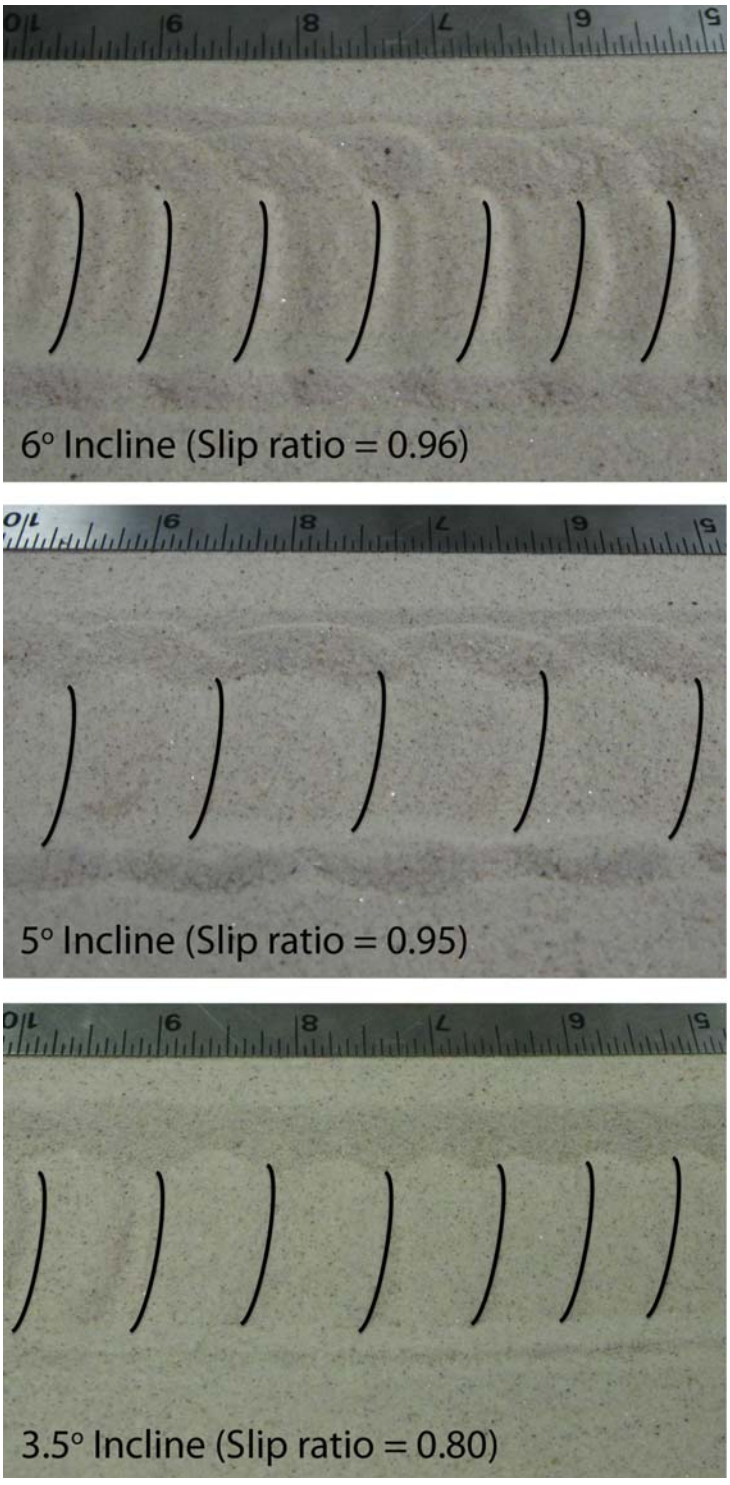

Figure 6.2: Tracks from the rear wheels of the micro rover (Digitally added lines to help identify the ridges)

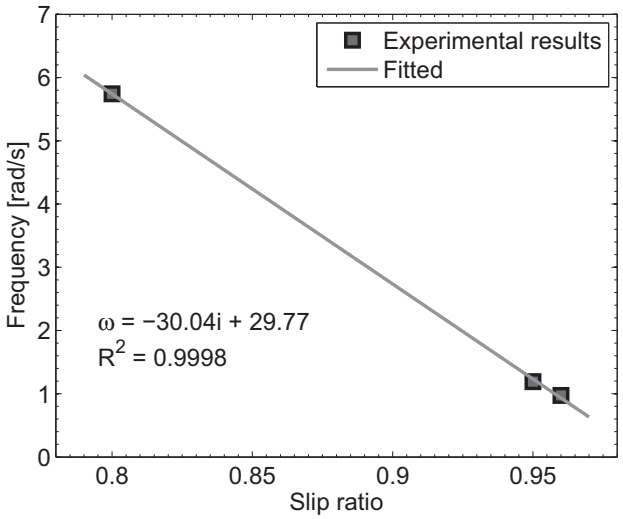

Figure 6.3: Ripple Frequency vs slip ratio

Table 6.1. These parameters were held constant throughout all of the simulations carried out for all work in this chapter. Figure 6.4 plots the sinkage, drawbar pull and normal load as a function time and overlays experimental results with the dynamic pressure-sinkage model described by Equation (5.9) and a traditional terramechanic model which was described in Chapter 3. The traditional terramechanic model was able to reasonably model the mean sinkage and normal force; however, it under predicted the drawbar pull by 5N for this case. This under prediction can be attributed to the fact that Bekker's traditional terramechanics model was originally developed for larger wheels [Bek69, Won01, MGS11]. It has been recently shown by [MGS11] that smaller wheels tend to experience greater sinkage than the predicted values from Bekker's model which, in turn, can lead to larger rolling resistances and reduced tractive performance. As a result, drawbar pull would be underpredicted as confirmed by Figure 6.4. One will notice that the dynamic pressure-sinkage model oscillates about the mean values predicted by Bekker's terramechanic model as expected and accurately predicts the amplitudes and frequencies of the oscillations observed in the measured data. It should be noted that, although any adjustments or improvements to the mean values in Figure 6.4 using correction factors such as those discussed by [MGS11] would

Table 6.1: Summary of Parameters

Parameter	Value	Unit	Comments
k_c'	0	–	Dimensionless cohesive modulus
k_ϕ'	80	–	Dimensionless frictional modulus
K	0.036	m	Shear deformation modulus
n	1	–	Sinkage exponent
γ	13734	N/m^3	Soil weight density
$d\gamma$	$0.1 \times \gamma$	N/m^3	Change in soil weight density
r	0.1	m	Radius of wheel
b	0.075	m	Width of wheel
η	1.35	–	Rear of wheel sinkage relationship
ϕ	28	deg	Internal angle of friction
c	0	kPa	Soil cohesion
C_f	800	Ns/m	Viscous friction coefficient
k_g'	0.1	–	Dimensionless grouser amplitude coefficient
k_a'	0.05	–	Dimensionless density amplitude coefficient

require re-tuning of the dynamic pressure-sinkage relationship, the resulting accuracy of the predicted amplitudes and frequencies of the oscillations would be maintained.

To further validate the predictive capabilities of the model, comparisons for slip ratios of 0.15, 0.25, 0.35 and 0.75 can be seen in Figure 6.5, which presents the data as mean-adjusted plots during steady-state operation so that the oscillations and contribution of the dynamic pressure-sinkage relationship described by Equation (5.9) can be easily compared. Note that the model parameters used for these cases were the same as those used to manually tune the model (Table 6.1). The gradual entrance and exit of a grouser from the terrain is not considered in this work and one will notice small discontinuities in the simulated data from the dynamic pressure-sinkage model in the presented data. The RMS data comparing the simulated and experimental work is presented in Table 6.2 along with the absolute difference or delta between these two calculations. The RMS values were taken from the mean adjusted comparisons for the time periods shown in Figures 6.4 and 6.5. The RMS values indicate reasonable and consistent results when compared to the time history results of Figures 6.4 and 6.5.

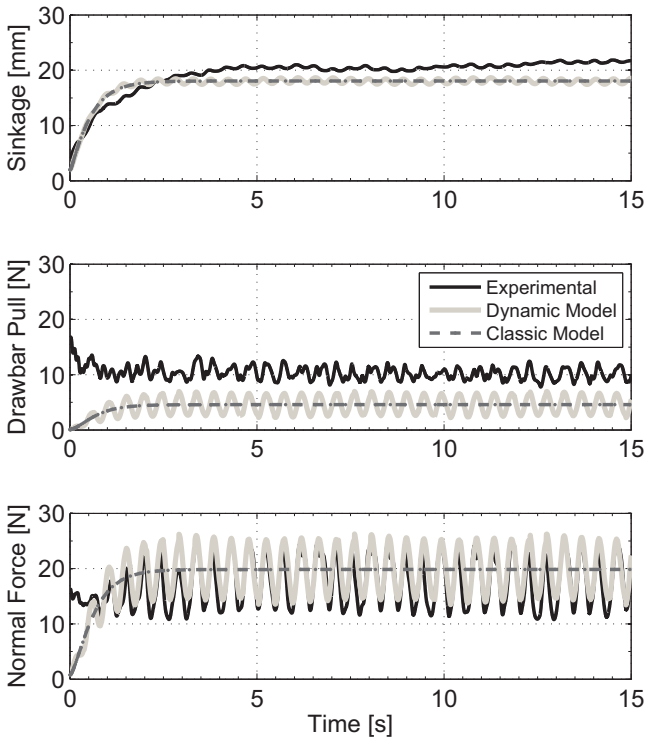

Figure 6.4: Overlay of experimental data with the dynamic and classic models for a rigid wheel with 16, 23mm long grousers, operating at 0.50 slip and a 15N normal load

Figure 6.5 shows that the dynamic model is able to accurately predict the oscillations in the sinkage, drawbar pull and normal force for all cases except for the 0.75 slip ratio case. At this high slip ratio the wheel is excavating the terrain and the sinkage becomes smoother. When the excavation increases one will also notice that the RMS delta (difference) values (Table 6.2) increase for all three measurements. When examining the normal load RMS delta for the 0.75 slip ratio case, the model is over predicted the amplitude and the resulting RMS delta is 1.338. A possible explanation for this reduction in the experimental oscillation amplitude is that, at such high slip ratios, the terrain does not come to rest before the next grouser comes into contact with it resulting in a more continuous flow of sand material. Such a fluidization, which can occur when a granular material

is excited by small displacements through vibration or other means, cause the macroscopic property of the granular system to change from a solid to a fluid [JN92]. This fluidization phenomena is not accounted for in the current terramechanic model. The next case study investigates the ability of the new dynamic model to predict oscillations in the sinkage, drawbar pull and normal force when the grouser length is reduced from 23mm to 10mm.

Table 6.2: RMS Data for Case Study #2

Sinkage

Slip Ratio	RMS Experimental	RMS Proposed Model	$\|\Delta\|$ Difference
.15	0.478	0.339	0.139
.25	0.264	0.336	0.072
.35	0.317	0.337	0.020
.50[1]	0.257	0.333	0.076
.75*	0.171	0.330	0.159

Drawbar Pull

Slip Ratio	RMS Experimental	RMS Proposed Model	$\|\Delta\|$ Difference
.15	1.679	0.896	0.783
.25	1.196	1.129	0.066
.35	0.957	1.330	0.374
.50[1]	1.003	1.539	0.536
.75	1.099	1.807	0.708

Normal Force

Slip Ratio	RMS Experimental	RMS Proposed Model	$\|\Delta\|$ Difference
.15	4.187	4.342	0.155
.25	4.232	4.271	0.039
.35	3.811	4.254	0.443
.50[1]	4.094	4.151	0.57
.75	2.792	4.130	1.338

[1] Denotes the slip ratio which the model was tuned with

* Denotes measurements where the oscillations were diminished due to an un-modeled phenomena

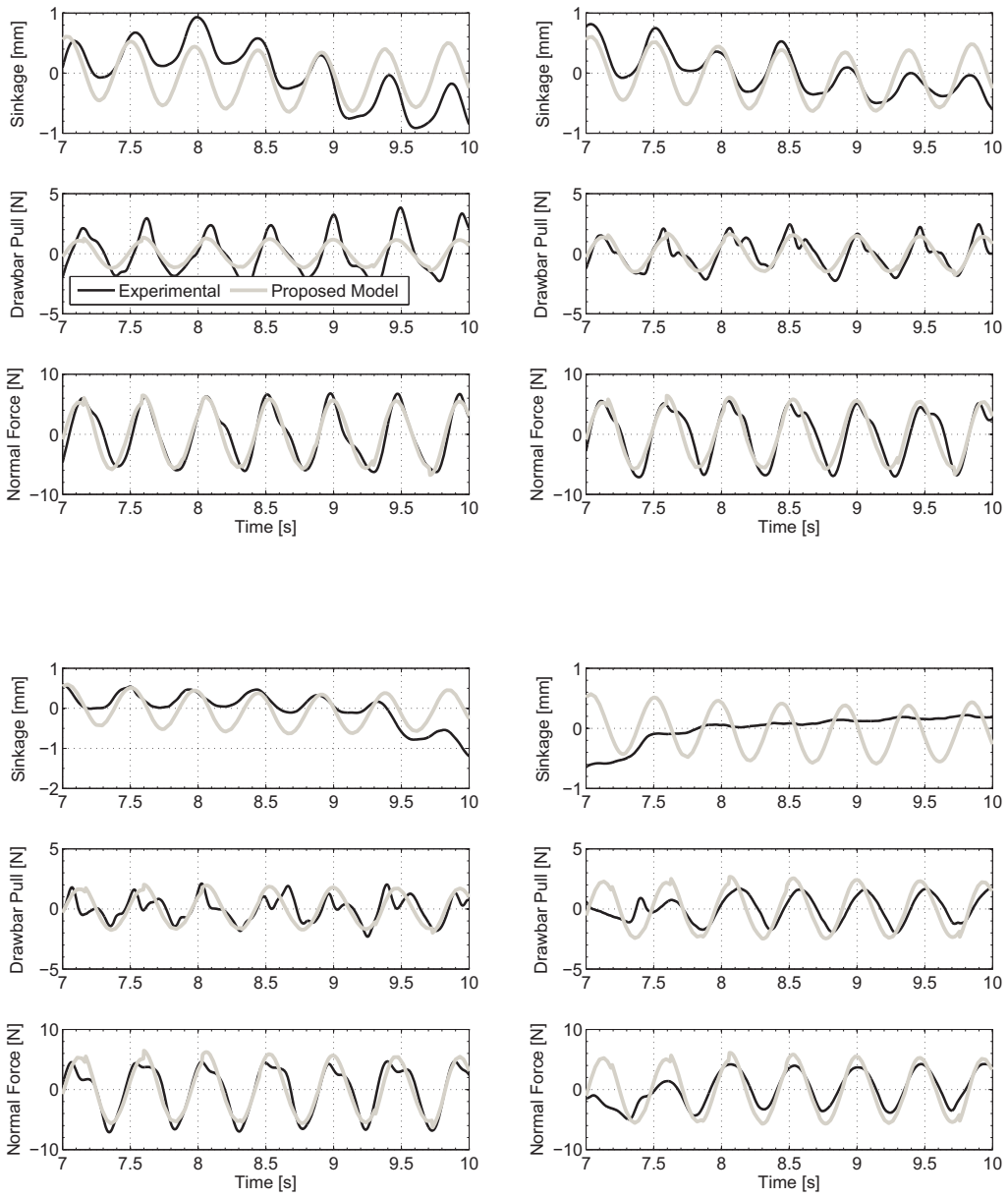

Figure 6.5: Mean adjusted simulation data of a rigid wheel with 16, 23mm long grousers, operating with a 15N normal load overlayed with experimental data. Top Left) 0.15 slip ratio; Top Right) 0.25 slip ratio Bottom Left) 0.35 slip ratio; Bottom Right) 0.75 slip ratio

6.3 Case Study #3: Length of Grousers

Building on the previous case study, SWTB experiments were carried out using a 16 grouser wheel which had the length of each grouser reduced from 23mm to 10mm. Figure 6.6 plots the resulting mean-adjusted experimental and simulated values for sinkage, drawbar pull and normal force as a function of time for slip ratios of 0.25, 0.35, 0.50 and 0.60. The values used for this case study were, again, kept the same as those used to originally tune the model (Table 5.1). For this case study, Table 6.3 presents the RMS data for the experimental and simulated data. The table also presents the difference or delta between these two calculations. The RMS values were taken from the mean adjusted comparisons for the time periods shown in Figure 6.6 and indicate reasonable and consistent results when compared to the time history data of Figure 6.6.

One can see from Figure 6.6 that, for the 0.25 and 0.35 slip ratio cases, the oscillations in all of the measured data is accurately predicted by the model. As observed in the previous section, at the higher slip ratios, particularly 0.60, the model begins to lose its predictive capability for the oscillations in the sinkage. This result is expected based on the previous case study (Section 6.2). As the wheel begins to spin for longer periods of time in the same location, the wheel appears to continuously excavate the surrounding terrain. Since the wheel lacks appreciable forward movement into undisturbed terrain, the grousers cause the sand in the vicinity of the wheel to be in constant motion. As previously mentioned, this fluidization phenomena is not accounted for in the dynamic pressure-sinkage relationship to more accurately model these high-slip conditions.

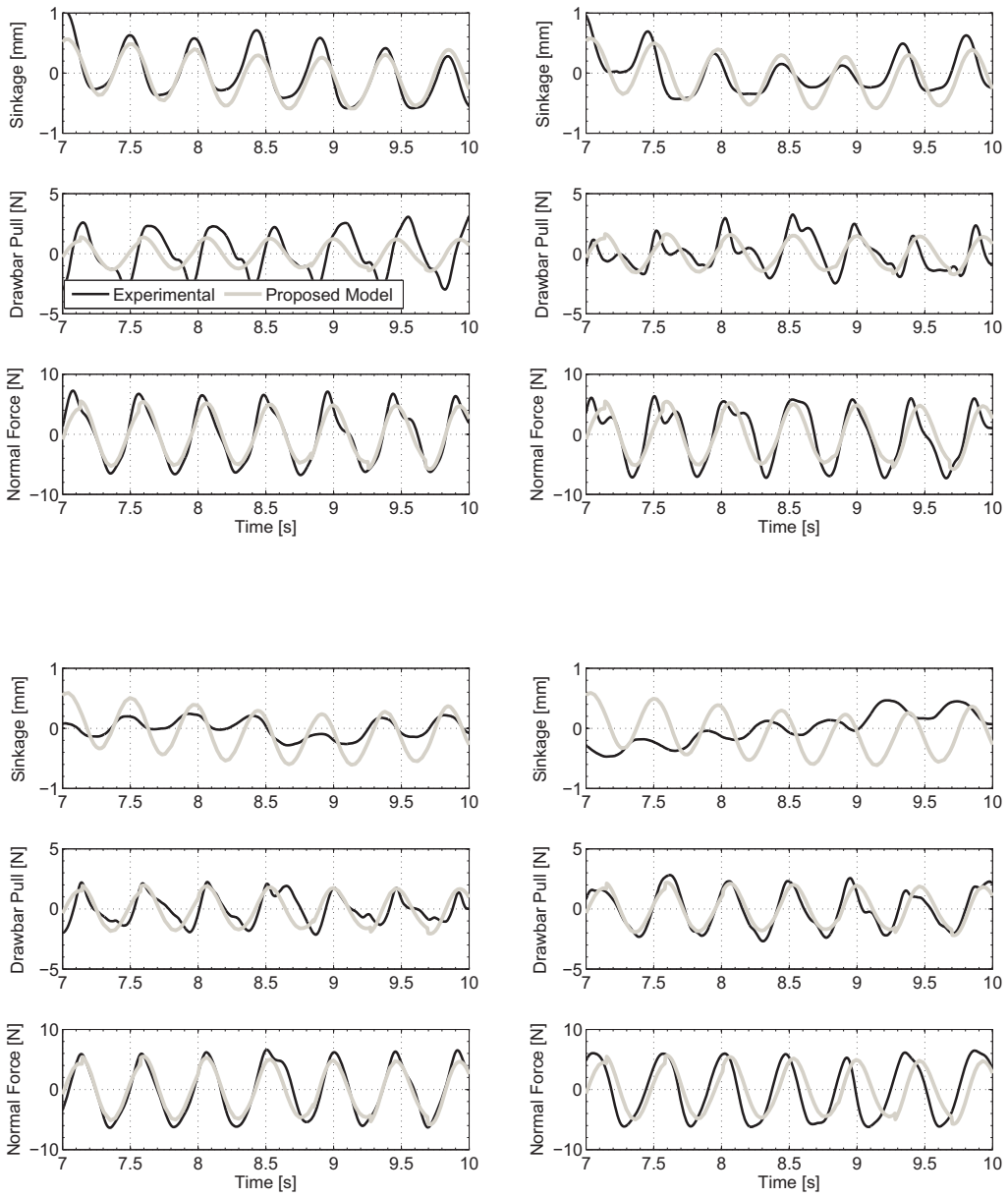

Figure 6.6: Mean adjusted simulation data of a rigid wheel with 16, 10mm long grousers, operating with a 15N normal load overlayed with experimental data. Top Left) 0.25 slip ratio; Top Right) 0.35 slip ratio Bottom Left) 0.50 slip ratio; Bottom Right) 0.60 slip ratio

Table 6.3: RMS Data for Case Study #3

Sinkage

Slip Ratio	RMS Experimental	RMS Proposed Model	$\lvert\Delta\rvert$ Difference
.25	0.419	0.312	0.107
.35	0.282	0.311	0.029
.50	0.150	0.308	0.158
.60	0.259	0.305	0.047

Drawbar Pull

Slip Ratio	RMS Experimental	RMS Proposed Model	$\lvert\Delta\rvert$ Difference
.25	1.691	0.948	0.743
.35	1.301	1.125	0.177
.50	1.145	1.340	0.195
.60	1.573	1.460	0.115

Normal Force

Slip Ratio	RMS Experimental	RMS Proposed Model	$\lvert\Delta\rvert$ Difference
.25	4.381	3.770	0.611
.35	4.240	3.759	0.481
.50	4.188	3.754	0.434
.60	4.461	3.764	0.697

6.4 Case Study #4: Number of Grousers

For this final case study the number of 10mm long grousers were increased from 16 to 32 and SWTB experiments and corresponding model simulations were carried out. Figure 6.7 show the resulting mean-adjusted overlay of experimental and simulated sinkage, drawbar pull and normal force plotted as a function of time for slip ratios of 0.25, 0.50, 0.60 and 0.75. The model parameters used for this case study were again set using the original tuning case for a wheel operating with a 15N normal load at a slip ratio of 0.5 (Table 5.1). One will notice from Figure 6.7 that all of the experimental sinkage results, including those at the lowest slip ratio tested, did not present a noticeable oscillation. This observation, given the resulting increase in flow of sand grains caused by a doubling of the number of grousers, can likely be attributed to the same fluidization phenomena which occurred in the previous test cases. When examining the drawbar pull results in Figure 6.7 one can see that the results are reasonable for slip ratios of 0.25 and 0.50; however, at the higher slip ratios of 0.6 and 0.75, the oscillations become less significant in all three measured signals—again, likely due to fluidization as the sand grains experience a constant flow at these higher slip ratios.

The RMS data comparing the simulated and experimental work is presented in Table 6.3. The RMS values show a large over prediction from the model, especially in the normal force results where the minimum and maximum deltas are 1.778 and 3.187, respectfully. One will notice that the delta RMS values of the sinkage results are very small, suggesting that the model is accurately predicting the amplitude of the oscillations. However, examining the time history data in Figure 6.7 one will see that there are no oscillations in the sinkage measurements. Therefore, examining only the RMS values as a measure of accuracy can be misleading. If one examines Figure 6.7, the experimental data has some natural variation or drift for all slip ratios during the time period shown in the figure. The amplitude of the drift is very close to the amplitude of the model predicted oscillations. Since RMS calculations are independent of phase and frequency, one cannot rely solely on the delta RMS data to conclude if the results are accurate, reasonable or valid. To correctly interpret the RMS results, one must also examine the time history response to conclude if excessive excavation is occurring.

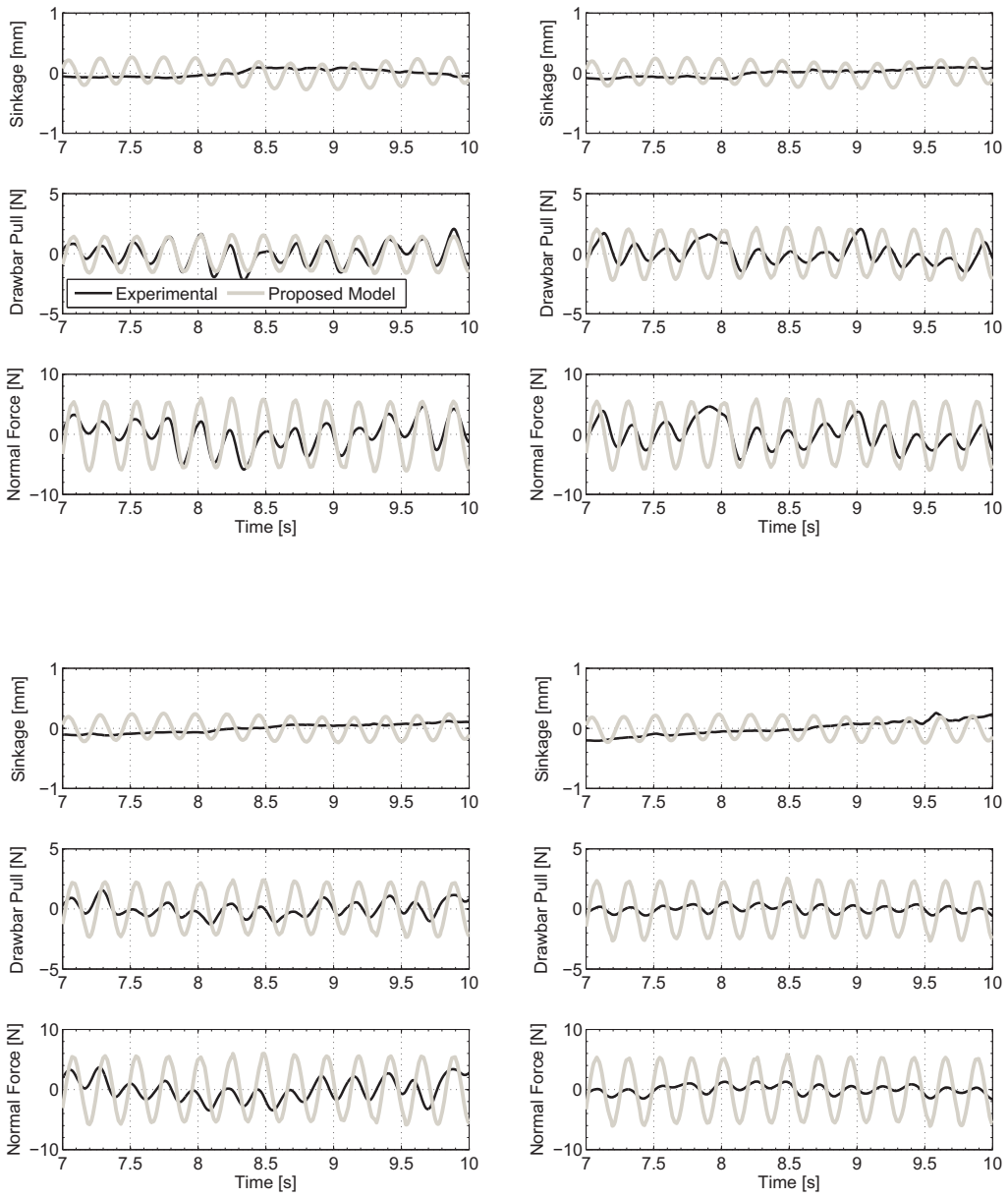

Figure 6.7: Mean adjusted simulation data of a rigid wheel with 32, 10mm long grousers, operating with a 15N normal load overlayed with experimental data. Top Left) 0.25 slip ratio; Top Right) 0.50 slip ratio Bottom Left) 0.60 slip ratio; Bottom Right) 0.75 slip ratio

Table 6.4: RMS Data for Case Study #4

Sinkage

Slip Ratio	RMS Experimental	RMS Proposed Model	$\lvert\Delta\rvert$ Difference
.25*	0.060	0.158	0.099
.35*	0.065	0.152	0.087
.50*	0.072	0.149	0.077
.75*	0.116	0.149	0.032

Drawbar Pull

Slip Ratio	RMS Experimental	RMS Proposed Model	$\lvert\Delta\rvert$ Difference
.25	0.862	1.062	0.200
.35	0.794	1.474	0.680
.50	0.615	1.581	0.966
.75	0.285	1.708	1.423

Normal Force

Slip Ratio	RMS Experimental	RMS Proposed Model	$\lvert\Delta\rvert$ Difference
.25	2.237	4.015	1.778
.35	2.082	3.978	1.896
.50	1.790	3.940	2.150
.75	0.716	3.903	3.187

* Denotes measurements where the oscillations were diminished due to an un-modeled phenomena

6.4.1 Discussion of the Excavation

To further elaborate on the excavation phenomena which occurs during high slip or sustained slip, two figures are presented: Figure 6.8 which shows a rigid wheel with 32, 10mm long grousers operating at slip ratio of 0.60, and Figure 6.9 showing a rigid wheel with 32, 10mm long grousers operating at slip ratio of 1.00. One can see in Figure 6.8 that there is excavation ahead of the wheel and from either side of the wheel. As the wheel traverses forward the terrain is constantly being milled away ahead of the wheel. This material deformation is not accounted for in the terramechanic model and is a likely cause of the diminished oscillations in the measurements. To further highlight the excavation process, Figure 6.9 depicts the same wheel operating at slip ratio of 1.00 and shows the massive excavation ahead of the wheel and from either side of the wheel. The time history data of the sinkage, drawbar pull and normal force of the wheel operating at a slip ratio of 1.00 is shown in Figure 6.10. In this figure one can see the constant and increasing sinkage of the wheel with no appreciative oscillations, suggesting that the terrain is experiencing a continuous motion and excavation. Oscillations are still present in the drawbar pull and normal force measurements and this is to be expected as the grousers will still impact the terrain causing a change in the forces. However, since the terrain is in constant motion, the change in force will not cause an oscillation in the sinkage but rather the grouser's impact will aid in the continual excavation process of the terrain ahead, beneath and adjacent to the wheel.

6.5 Summary

As a result of the case studies presented in this work, it has been shown that the dynamic model previously proposed in Chapters 4 and 5 should only be implemented when there is sustained slippage and positive drawbar pull. Case studies which varied the number and length of the grousers on a wheel demonstrated that the model is able to reasonably capture and predict the dynamic oscillations observed in the drawbar pull and normal force measurements over a wide range of slip ratios while using only one tuning condition. Under high-slip conditions, and when the number of grousers on a wheel is relatively high, there appears

Figure 6.8: Rigid wheel with 32, 10mm grousers operating at a slip ratio of 0.60

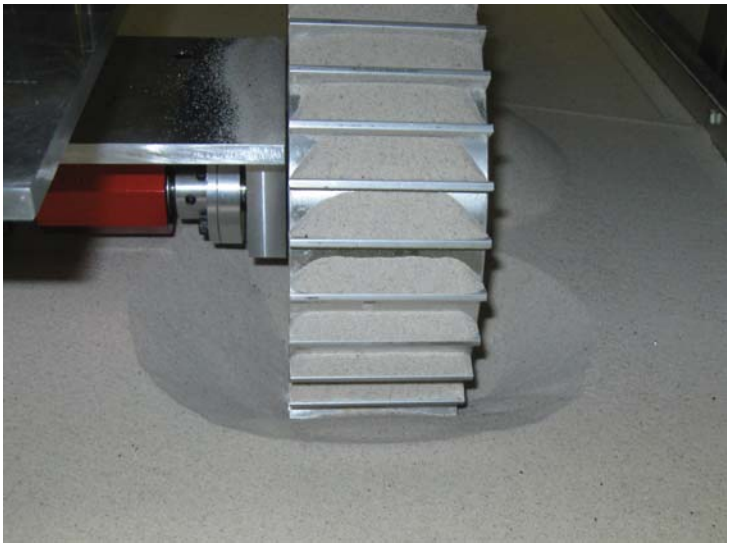

Figure 6.9: Rigid wheel with 32, 10mm grousers operating at a slip ratio of 1

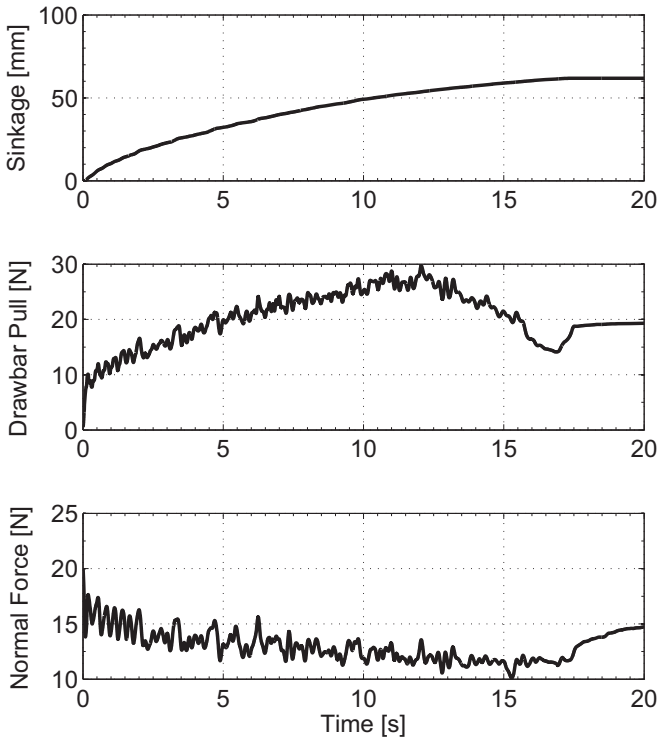

Figure 6.10: Time history data of a rigid wheel with 32, 10mm grousers operating at a slip ratio of 1

to be an unaccounted for fluidization phenomena which reduces the amplitude of the observed oscillations in the sinkage. Also, RMS data should be used in conjunction with time history data to ensure the numeric quantification is appropriate and meaningful.

CHAPTER 7

CONCLUSIONS

The objective of this research was to develop a wheel-soil interaction model that can better predict the oscillations in the sinkage, drawbar pull and normal force for rigid wheels operating in sandy soil.

This chapter summarizes the main results and conclusions of each chapter. A list of contributions that this doctorial work has made to the field of terramechanics is also included as well as some brief suggestions of possible avenues for future research.

7.1 Conclusions

CHAPTER 1 – INTRODUCTION

Chapter 1 presented the observed oscillatory pattern in the measured data corresponding and ripples in the tracks of a smooth wheel and a grouser wheel. The chapter shows how existing analytical terramechanic models do not inherently capture the observed phenomena.

CHAPTER 2 – EXPERIMENTAL EQUIPMENT AND DEVELOPMENT

Chapter 2 investigated several different single-wheel testbeds (SWTBs) and described the new and novel SWTB which was built for the purpose of this research. The new SWTB translated the terrain instead of the wheel support system. This alternative arrangement was shown to be a viable method of conducting terramechanic studies, as the results of the new equipment are in reasonable agreement with the results from other researchers. It was found that the addition of a simple

counter balance added versatility to a SWTB so that a variety of normal loads could be studied. Over 300 individual experiments were performed on the new SWTB, processed and presented in the chapter. The tests were conducted for a variety of wheel configurations, slip ratios and normal loads. The chapter concluded with confirmation that the ripples in the track of a smooth wheel are not a function of the new SWTB, as the ripples were recreated with the testing of a micro rover operating under its own power in the same sandy soil.

Chapter 3 – A Review of Terramechanics

Chapter 3 reviewed various finite element methods (FEM) that could be used to model the observed phenomena; however, it was found that finite element methods and techniques are very computationally expensive and, therefore, not well suited for motion planning, dynamic simulators and terrain estimation. Analytical terramechanic modelling techniques were examined and a numerical solution algorithm was constructed in MATLAB & Simulink which replicates the full dynamics of the SWTB. The chapter then examines the influence of each parameter contained in the analytical terramechanic model to determine which parameters could explain the observed phenomena. It was also shown that the numerical solution runs significantly faster than FEM. The chapter concludes by stating that an analytical approach will be taken to examine the focus of the thesis.

Chapter 4 – Smooth Wheel Model

Chapter 4 presented a new dynamic pressure-sinkage relationship for modelling the observed oscillations in drawbar pull and normal force for a smooth rigid wheel on dry sand. The final form of the new dynamic pressure-sinkage relationship for a smooth wheel is:

$$p(z) = \left(ck'_c + \gamma bk'_\phi\right)\left(\frac{z}{b}\right)^n + d\gamma l_c k'_a \sin(\omega(i)t + \Phi) \tag{7.1}$$

The proposed model was validated over a wide range of slip ratios and normal loads. The model adds one new dimensionless empirical coefficient k'_a to a known terramechanic model. The additional term does not affect the mean values of the

sinkage, drawbar pull or normal load, but rather adds oscillations about the simulated means.

CHAPTER 5 – GROUSER WHEEL MODEL

Chapter 5 built on the smooth-wheel model and presented a new form for the pressure-sinkage relationship to capture the dynamic oscillations observed for a wheel with grousers:

$$p(z) = \left(ck'_c + \gamma b k'_\phi\right)\left(\frac{z}{b}\right)^n + (k'_g \bar{\sigma_p} + k'_a l_c d\gamma)\sin\left(\frac{\omega_w}{n_g}t + \Phi\right) \tag{7.2}$$

The new model improves traditional terramechanic models when the dynamic effects of grousers are of importance. The additional terms in the model are based on existing soil mechanic theories that vary as a function of soil properties, slip conditions, and vehicle loading. The model has two new dimensionless empirical coefficients k'_g and k'_a. As in the smooth wheel model, the additional terms in the new grouser wheel model do not affect the mean values of the sinkage, drawbar pull or normal load.

CHAPTER 6 – CASE STUDIES AND MODEL APPLICATIONS

As a result of the case studies presented in Chapter 6, it was shown that the dynamic model should only be implemented when there is sustained slippage and positive drawbar pull. Case studies which varied the number and length of the grousers on a wheel demonstrated that the model is able to reasonably capture and predict the dynamic oscillations observed in the drawbar pull and normal force measurements using only one tuning condition. Also, RMS data should be used in conjunction with time history data to ensure that the numeric quantification is appropriate and meaningful.

7.2 Contributions to the Field

This doctorial thesis made the follow contributions to the knowledge in the field of terramechanics:

1. design of a new high fidelity single-wheel testbed which translates the terrain and is capable varying the normal loads due to a simple counter balance. In addition, confirmation was presented that this new style of single-wheel testbed produces appropriate results for small wheels operating in sandy soil.

2. correlation of the ripples in the sand in the track of the smooth wheel to the corresponding oscillations in the measured data. In addition, it was confirmed that these ripples in the sand are not a function of the testing equipment because the same ripples were observed on a powered micro rover.

3. development of a dynamic pressure-sinkage model that can be used to model the fluctuations in the drawbar pull and normal force of a smooth wheel operating in sandy soil. In addition, analytical and empirical solutions were presented for the new terms found in the new model.

4. development of a dynamic pressure sinkage model that can be used to model the fluctuations in the sinkage, drawbar pull, and normal force of a wheel with grousers operating in sandy soil. In addition, analytical and empirical solutions were presented for the new terms found in the new model.

5. experimental validation that the new dynamic pressure-sinkage model for a smooth wheel and a wheel with grousers produces reasonable results in a predictive mode of operation.

7.3 Future Work

This thesis presents a viable solution that is built upon traditional terramechanic theory and validated experimentally to capture a phenomena that researchers have observed in testing of smooth and grouser wheels, but have not modelled. Through the course of this work some interesting future avenues of research have emerged:

1. development of a sophisticated method to model the accelerated excavation

that appears at hight slip ratios (> 0.50). A method to model this excavation will aid in the development of lightweight mobile robots and, in particular, planetary rovers. The model would also help mission specialists determine the mobility of their vehicles and aid in their path-planning/motion control. This model would be of particular importance for vehicles that become entrench in loose sandy soil, such as NASA's *Spirt* rover.

2. carry out a parametric study of different wheel configurations and terrains so that further quantification can be made of the oscillations. Moreover, once new experimental data exists for various terrains and wheels an investigation can be performed to determine correlations for the new dimensionless parameters k'_a and k'_ϕ. The ability to predict k'_a and k'_ϕ *a priori* will reduce the complexity of the soil-wheel interaction model and any required tuning.

3. direct measurements of the stresses/pressures acting on the wheel and in the soil, so that the accuracy of the new pressure-sinkage model can be further validated. The modifications that this research made to the Reece pressure-sinkage relationship was borne from force measurements. The resulting pressure-sinkage relationship is an approximation of the true stresses acting on the wheel-soil interface. While the approximation is capable of modelling and predicting the forces and sinkage of a single wheel, in order to model the actual stress field, direct stress measurements are required.

4. It would be very interesting to see how the new model can be integrated into existing algorithms and simulators for the purpose of path-planning, motion control and soil-parameter estimation.

APPENDIX A

SMOOTH WHEEL ALGORITHM

The solution methodology used to simulate the smooth wheel model is as follows:

1. Input all model constants and constraints and prescribe the settled or static sinkage value (i.e. 2 [mm]) for $t = t_o$ and calculate ω, as it is constant for a SWTB simulation.
2. Calculate θ_f, θ_r and θ_m.
3. Calculate the contact length l_c and use this value to calculate $A = k'_a l_c d\gamma$.
4. Compute the normal stress value $\sigma(\theta)$ and shear stress $\tau(\theta)$ and include the $A\sin(\omega t + \phi)$ term.
5. Integrate the stress from θ_r to θ_f to compute the forces F_z and F_x.
6. Frictional damping F_f of the system must be applied to the vertical direction to account for any losses in the system. Sum the forces in the vertical direction to calculate the sinkage acceleration and then integrate the sinkage acceleration twice to obtain a new sinkage value for the next time-step and return to Step 2 with the updated values.

Step 1 of the simulation is carried out within a MATLAB $*$.m file prior to calling the Simulink $*$.mdl file which computes the remaining steps. Simulation steps 2 through 5 are handled by a `Level-2 M file S-Function` within the Simulink model. The important outputs from the S-Function are the wheel sinkage (z),

drawbar pull (F_x) and normal force (F_z). Figure 3.6 shows a simplified schematic representation of the single-wheel testbed pulley system and the corresponding Simulink/Simscape representation of the system that computes step 6 of the simulation methodology. To compute this step one must take the normal force F_z into the Simscape environment with an implementation of the pulley counterbalance system where the masses on either side of the pulley are modeled along with the pulley itself. As shown in Figure 3.6, on one side of the pulley there is only the dead weight of counter balance mass. On the other side of the pulley there is the mass of the SWTB rig and the wheel. A grounded `translational damper` block in Simscape attached on the single-wheel testbed rig side accounts for frictional losses in the vertical direction of the system. The viscous coefficient for the damper was set to 800 [Ns/m]. The losses modelled by this damper can come from the linear bearings, linear potentiometer and unaccounted for effects in the terrain deformation. The normal force F_z from the S-Function becomes the forcing function acting on the mass of the wheel side of the counter balance. Simulink/Simscape computes the displacement of the wheel and this displacement is the new sinkage value that is fed back into the soil model S-Function for the next time-step. One will notice in Figure 3.6 that there is a 1:1 gearbox and a zero input torque source between the two sides of the pulley in the Simulink/Simscape model. These blocks were needed to explicitly state the relationship between the two sides of the pulley. One could expand this Simscape implementation to model a full rover with multiple wheels and degrees of freedom and even alter the acceleration due to gravity to simulate Mars or Moon scenarios.

APPENDIX B

GROUSER WHEEL ALGORITHM

The solution methodology used to simulate the grouser wheel model is as follows:

1. Input all model constants and constraints and prescribe the settled or static sinkage value (i.e. 2 [mm]) for $t = t_o$ and calculate ω, as it is constant for a SWTB simulation.
2. Calculate θ_f, θ_r and θ_m.
3. Calculate the contact length l_c and determine which grousers are in contact with the terrain and calculate $\bar{\sigma}_p$.
4. Calculate $A = k'_a l_c d\gamma + k'_g \bar{\sigma}_p$.
5. Compute the normal stress value $\sigma(\theta)$ and shear stress $\tau(\theta)$ and include the $A\sin(\omega t + \phi)$ term.
6. Integrate the stress from θ_r to θ_f to compute the forces F_z and F_x.
7. Frictional damping F_f of the system must be applied to the vertical direction to account for any losses in the system. Sum the forces in the vertical direction to calculate the sinkage acceleration and then integrate the sinkage acceleration twice to obtain a new sinkage value for the next time-step and return to Step 2 with the updated values.

Step 1 of the simulation is carried out within a MATLAB $*$.m file prior to calling the Simulink $*$.mdl file which computes the remaining steps. Simulation steps

2 through 6 are handled by a `Level-2 M file S-Function` within the Simulink model. The important outputs from the S-Function are the wheel sinkage (z), drawbar pull (F_x) and normal force (F_z). Figure 3.6 shows a simplified schematic representation of the single-wheel testbed pulley system and the corresponding Simulink/Simscape representation of the system that computes step 7 of the simulation methodology. To compute this step one must take the normal force F_z into the Simscape environment with an implementation of the pulley counterbalance system where the masses on either side of the pulley are modeled along with the pulley itself. As shown in Figure 3.6, on one side of the pulley there is only the dead weight of counter balance mass. On the other side of the pulley there is the mass of the SWTB rig and the wheel. A grounded `translational damper` block in Simscape attached on the single-wheel testbed rig side accounts for frictional losses in the vertical direction of the system. The viscous coefficient for the damper was set to 800 [Ns/m]. The losses modelled by this damper can come from the linear bearings, linear potentiometer and unaccounted for effects in the terrain deformation. The normal force F_z from the S-Function becomes the forcing function acting on the mass of the wheel side of the counter balance. Simulink/Simscape computes the displacement of the wheel and this displacement is the new sinkage value that is fed back into the soil model S-Function for the next time-step. One will notice in Figure 3.6 that there is a 1:1 gearbox and a zero input torque source between the two sides of the pulley in the Simulink/Simscape model. These blocks were needed to explicitly state the relationship between the two sides of the pulley. One could expand this Simscape implementation to model a full rover with multiple wheels and degrees of freedom and even alter the acceleration due to gravity to simulate Mars or Moon scenarios.

APPENDIX C

LIST OF PUBLICATIONS

As of June 2011 the following is a list of publications that has come from this doctorial thesis.

Journal

Irani, R. A., Bauer, R. J., Warkentin, A. A Dynamic Terramechanic Model for Small Lightweight Vehicles with Rigid Wheels and Grousers Operating in Sandy Soil. *Journal of Terramechanics*. (IN PRESS - May 2011)

Conference

Irani, R. A., Bauer, R. J.,Warkentin, A. (2011). Dynamic Terramechanic Model for Grouser Wheels on a Planetary Rover in Sandy Soil. *In the proceedings of Canadian Congress of Applied Mechanics, CANCAM 2011*, June 5-9th 2011.

Irani, R. A., Bauer, R. J., Warkentin, A. (2010). Modelling a Single-wheel Testbed for Planetary Rover Applications. *In the proceedings of the ASME Dynamic Systems and Control Conference, DSCC 2010*, September 13-15th 2010.

Irani, R. A., Bauer, R. J., Warkentin, A. (2010) Design of a Single-wheel Testbed and Preliminary Results for Planetary Rover Applications. *In the proceedings of The Canadian Society for Mechanical Engineering Forum CSME 2010*, Victoria, British Columbia, June 7-9, 2010.

REFERENCES

[ABIB+10] R.E. Arvidson, J.F. Bell III, P. Bellutta, N.A. Cabrol, J.G. Catalano, J. Cohen, L.S. Crumpler, D.J. Des Marais, T.A. Estlin, W.H. Farrand, et al. Spirit Mars Rover Mission: Overview and selected results from the northern Home Plate Winter Haven to the side of Scamander crater. *J. Geophys. Res*, 115, 2010.

[AES03] AESCO. *Matlab/Simulink module AESCO soft soil tyre model (AS2TM) user's guide*, 2003.

[AHG+10] A. Azimi, M. Hirschkorn, B. Ghotbi, J. Kovecses, J. Angeles, P. Radziszewski, M. Teichmann, M. Courchesne, and Y. Gonthier. Simulation-based rover performance evaluation and effects of terrain modelling. In *CASI Astronautics Conference ASTRO 2010*, May 4-6 2010.

[ARS06] Z. Asaf, D. Rubinstein, and I. Shmulevich. Evaluation of link-track performances using DEM. *Journal of Terramechanics*, 43(2):141–161, 2006.

[AWHT03] D. Apostolopoulos, M. Wagner, S. Heys, and J. Teza. Results of the inflatable robotic rover testbed. Technical Report CMU-RI-TR-03-18, Carnegie Mellon University, June 2003.

[Bek69] M.G. Bekker. *Introduction to terrain-vehicle systems*. University of Michigan Press, Ann Arbor, 1969.

[BLB05] R. Bauer, W. Leung, and T. Barfoot. Experimental and simulation results of wheel-soil interaction for planetary rovers. In *2005 IEEE/RSJ International Conference on Intelligent Robots and Systems (IROS 2005).*, pages 586–591. IEEE, 2005.

[Blo91] W.A. Block. *Analysis of soil stress under rigid wheel loading*. Ph.d. dissertaion, Auburn University, Auburn AL, 1991.

[CFJ+05] R.C. Chiroux, W.A. Foster, C.E. Johnson, S.A. Shoop, and R.L. Raper. Three-dimensional finite element analysis of soil interaction with a rigid wheel. *Applied Mathematics and Computation*, 162(2):707 – 722, 2005.

[DC79] J. Dundurs and M. Comninou. Some consequences of the inequality conditions in contact and crack problems. *Journal of Elasticity*, 9(1):71–82, 1979.

[DDG+11] L. Ding, Z. Deng, H. Gao, K. Nagatani, and K. Yoshida. Planetary rovers' wheel—soil interaction mechanics: new challenges and applications for wheeled mobile robots. *Intelligent Service Robotics*, 4(1):17–38, 2011.

[DGD+08] L. Ding, H. Gao, Z. Deng, P. Song, and R. Liu. Design of comprehensive high-fidelity/high-speed virtual simulation system for lunar rover. In *IEEE Conference on Robotics, Automation and Mechatronics*, pages 1118–1123. IEEE, 2008.

[DGD+11] L Ding, H. Gao, Z. Deng, K. Nagatani, and K. Yoshida. Experimental study and analysis on driving wheels' performance for planetary exploration rovers moving in deformable soil. *Journal of Terramechanics*, 48(1):27 – 45, 2011.

[DP52] D.C. Drucker and W. Prager. Soil mechanics and plastic analysis or limit design. *Quarterly of Applied Mathematics*, page 157, 1952.

[EPR+05] A. Ellery, N. Patel, L. Richter, R. Bertrand, and J. Dalcomo. Exomars rover chassis analysis and design. In *Proceedings of the 8th international symposium on artificial intelligence, robotics and automation in space (iSAIRAS), ESTEC.*, 2005.

[Fer04] C.W. Fervers. Improved fem simulation model for tire-soil interaction. *Journal of Terramechanics*, 41(2-3):87–100, 2004.

[FHM10] D. Flippo, R. Heller, and D. Miller. Turning efficiency prediction for skid steer robots using single wheel testing. In Andrew Howard, Karl Iagnemma, and Alonzo Kelly, editors, *Field and Service Robotics*, volume 62 of *Springer Tracts in Advanced Robotics*, pages 479–488. Springer Berlin / Heidelberg, 2010.

[FM11] D. Flippo and D. Miller. Suspension and wheel evaluation and experimentation testbed for planetary rovers. *International Journal of Mechatronics and Automation*, 1(1):29–37, 2011.

[Hal07] J.O. Hallquist. *LS-DYNA. Keyword Users Manual. Version 971*. 2007.

[HD08] J.P. Hambleton and A. Drescher. Development of improved test rolling methods for roadway embankment construction. Final Report MN/RC 2008-08, University of Minnesota. Dept. of Civil Engineering, February 2008.

[HK81] R.D. Holtz and W.D. Kovacs. *An introduction to geotechnical engineering*, volume 733. Prentice-Hall, 1981.

[HPC01] D.A. Horner, J.F. Peters, and A. Carrillo. Large scale discrete element modeling of vehicle-soil interaction. *Journal of engineering mechanics*, 127:1027, 2001.

[HU60] E. Hegedus and Land Locomotion Laboratory (US). *A simplified method for the determination of bulldozing resistance*. US Army Ordnance Tank-Automotive Command, 1960.

[HZSA06] S. Hutangkabodee, Y. Zweiri, L. Seneviratne, and K. Althoefer. Soil parameter identification for wheel-terrain interaction dynamics and traversability prediction. *International Journal of Automation and Computing*, 3:244–251, 2006.

[IBD04] K. Iagnemma, C. Brooks, and S. Dubowsky. Visual, tactile, and vibration-based terrain analysis for planetary rovers. In *Proceedings of IEEE Aerospace Conference*, volume 2, pages 841–848. IEEE, 2004.

[ID04] K. Iagnemma and S. Dubowsky. *Mobile robots in rough terrain*. Springer, 2004.

[IGD99] K. Iagnemma, F. Genot, and S. Dubowsky. Rapid physics-based rough-terrain rover planning with sensor and control uncertainty. In *IEEE International Conference on Robotics and Automation*, volume 3, pages 2286–2291. IEEE, 1999.

[IKSD04] K. Iagnemma, S. Kang, H. Shibly, and S. Dubowsky. Online terrain parameter estimation for wheeled mobile robots with application to planetary rovers. *IEEE Transactions on Robotics*, 20(5):921–927, 2004.

[IMNY07] G. Ishigami, A. Miwa, K. Nagatani, and K. Yoshida. Terramechanics-based model for steering maneuver of planetary exploration rovers on loose soil. *Journal of Field Robotics*, 24(3):233–250, 2007.

[INY09] G. Ishigami, K. Nagatani, and K. Yoshida. Slope traversal controls for planetary exploration rover on sandy terrain. *Journal of Field Robotics*, 26(3):264–286, 2009.

[ISD02] K. Iagnemma, H. Shibly, and S. Dubowsky. On-line terrain parameter estimation for planetary rovers. In *IEEE International Conference on Robotics and Automation (ICRA'02)*, volume 3, pages 3142–3147. IEEE, 2002.

[Ish08] G Ishigami. *Terramechanics-based Analysis and Control for Lunar/Planetary Exploration Robots*. Phd, Tohoku University, Department of Aerospace Engineering, March 2008.

[JGL+03] A. Jain, J. Guineau, C. Lim, W. Lincoln, M. Pomerantz, G. Sohl, and R. Steele. Roams: Planetary surface rover simulation environment. In *International Symposium on Artificial Intelligence, Robotics and Automation in Space (i-SAIRAS)*, 2003.

[JH61] Z. Janosi and B. Hanamoto. The analytical determination of drawbar pull as a function of slip for tracked vehicle in deformable soils. In *1st Int. Conf. on Terrain-Vehicle Systems*, 1961. Torino, Italy.

[JN92] H.M. Jaeger and S.R. Nagel. Physics of the granular state. *Science*, 255(5051):1523, 1992.

[Ker04] R.A. Kerr. On Mars, a second chance for life. *Science*, 306(5704):2010, 2004.

[KN78] L.L. Karafiath and E.A. Nowatzki. *Soil Mechanics for Off-Road Vehicle Engineering*. Clausthal Germany: Trans Tech Publications, first edition edition, 1978.

[KSJN07] L.R. Khot, V.M. Salokhe, H.P.W. Jayasuriya, and H. Nakashima. Experimental validation of distinct element simulation for dynamic wheel-soil interaction. *Journal of Terramechanics*, 44(6):429–437, 2007.

[KTMS06] A. Krebs, T. Thueer, S. Michaud, and R. Siegwart. Performance optimization of all-terrain robots: a 2D quasi-static tool. In *IEEE/RSJ International Conference on Intelligent Robots and Systems*, pages 4266–4271. IEEE, 2006.

[KUY+98] H. Kanamori, S. Udagawa, T. Yoshida, S. Matsumoto, and K. Takagi. Properties of lunar soil simulant manufactured in japan. In *Space 98*, volume 1, pages 462–468. ASCE, 1998.

[Lew04] B.A. Lewis. *Manual for LS-DYNA soil material model 147 (FHWA-HRT-04-095)*. 2004.

[LGD08] J. Liu, H. Gao, and Z. Deng. Effect of Straight Grousers Parameters on Motion Performance of Small Rigid Wheel on Loose Sand. *Information Technology Journal*, 7(8):1125–1132, 2008.

[LHC+10] W. Li, Y. Huang, Y. Cui, S. Dong, and J. Wang. Trafficability analysis of lunar mare terrain by means of the discrete element method for wheeled rover locomotion. *Journal of Terramechanics*, 47(3):161–172, 2010.

[Lya10] M. Lyasko. LSA model for sinkage predictions. *Journal of Terramechanics*, 47(1):1–19, 2010.

[MFM+07] C. Mungas, D. Fisher, GS Mungas, D. Apostolopoulos, and M. Wagner. SILVRCLAW III-Advanced Wheel Design and Testing. In *Aerospace Conference, 2007 IEEE*, pages 1–10. IEEE, 2007.

[MGS11] G. Meirion-Griffith and M. Spenko. A modified pressure-sinkage model for small, rigid wheels on deformable terrains. *Journal of Terramechanics*, 48(2):149 – 155, 2011.

[MRTG06] S. Michaud, L. Richter, T. Thuer, and A. Gibesch. Rover Chassis Evaluation and Design Optimisation Using the RCET. In *Proceedings of the 9th ESA Workshop on ASTRA*. Citeseer, 2006.

[NFO+07] H. Nakashima, H. Fujii, A. Oida, M. Momozu, Y. Kawase, H. Kanamori, S. Aoki, and T. Yokoyama. Parametric analysis of lugged wheel performance for a lunar microrover by means of DEM. *Journal of Terramechanics*, 44(2):153–162, 2007.

[NO04] H. Nakashima and A. Oida. Algorithm and implementation of soil-tire contact analysis code based on dynamic FE-DE method. *Journal of Terramechanics*, 41(2-3):127–137, 2004.

[PEA+06] N. Patel, A. Ellery, E. Allouis, M. Sweeting, and L. Richter. Rover mobility performance evaluation tool (rmpet): A systematic tool for rover chassis evaluation via application of bekker theory. In *Proceedings of the 8th ESA Workshop on ASTRA*, Noordwijk, The Netherlands, Nov. 2-4, 2004 2006.

[PNG06] H.A. Perko, J.D. Nelson, and J.R. Green. Mars soil mechanical properties and suitability of mars soil simulants. *Journal of Aerospace Engineering*, 19:169, 2006.

[Ree65] A.R. Reece. Principles of soil–vehicle mechanics. *Proceedings of the Institution of Mechanical Engineers, Automobile Division*, 180(1965):45–66, 1965.

[RH99] L. Richter and H. Hamacher. Investigating the locomotion performance of planetary microrovers with small wheel diameters and small wheel loads. In *Proceedings of the 13th international conference, ISTVS*, pages 719–26, 1999.

[SARW98] B. Shamah, D. Apostolopoulos, E. Rollins, and W.L. Whittaker. Field validation of nomad's robotic locomotion. In *Proceedings of SPIE - The International Society of Photo-Optical Engineering*, volume 3525, pages 214–222, November 1998.

[SBHS09] G.B. Sinclair, J.R. Beisheim, J.E. Helms, and S. Sezer. How to avoid futile finite element analysis of singular stresses. In *Proceedings of the 22nd Canadian Congress of Applied Mechanics*, May 31 2009.

[SGKR10] B. Schäfer, A. Gibbesch, R. Krenn, and B. Rebele. Planetary rover mobility simulation on soft and uneven terrain. *Vehicle System Dynamics*, 48(1):149–169, 2010.

[SID05] H. Shibly, K. Iagnemma, and S. Dubowsky. An equivalent soil mechanics formulation for rigid wheels in deformable terrain, with application to planetary exploration rovers. *Journal of Terramechanics*, 42(1):1–13, 2005.

[SOH99] R.W. Sumner, J.F. O'Brien, and J.K. Hodgins. Animating sand, mud, and snow. In *Computer Graphics Forum*, volume 18, pages 17–26. Wiley Online Library, 1999.

[WD07] A. Wilkinson and A. DeGennaro. Digging and pushing lunar regolith: Classical soil mechanics and the forces needed for excavation and traction. *Journal of Terramechanics*, 44(2):133 – 152, 2007.

[Won80] J.Y. Wong. Data processing methodology in the characterization of the mechanical properties of terrain. *Journal of Terramechanics*, 17(1):13–41, 1980.

[Won89] J.Y. Wong. *Terramechanics and off-road vehicles.* Elsevier, 1989.

[Won01] J.Y. Wong. *Theory of ground vehicles*. John Wiley, New York, 2001.

[Won10] J.Y. Wong. *Terramechanics and Off-Road Vehicles*. Butterworth-Heinemann, 2nd edition, October 2010.

[WR67] J.Y. Wong and A.R. Reece. Prediction of rigid wheel performance based on the analysis of soil-wheel stresses part I. Performance of driven rigid wheels. *Journal of Terramechanics*, 4(1):81–98, 1967.

[ZL06] R. Zhang and J. Li. Simulation on mechanical behavior of cohesive soil by Distinct Element Method. *Journal of Terramechanics*, 43(3):303–316, 2006.